2014

# Applications of the Variational Approach to Fracture Mechanics

Ataollah Mesgarnejad
*Louisiana State University and Agricultural and Mechanical College*, a.mesgarnejad@gmail.com

# APPLICATIONS OF THE VARIATIONAL APPROACH TO FRACTURE MECHANICS

A Dissertation

Submitted to the Graduate Faculty of the
Louisiana State University and
Agricultural and Mechanical College
in partial fulfillment of the
requirements for the degree of
Doctor of Philosophy

in

The Department of Mechanical Engineering

by
Ataollah Mesgarnejad
M.Sc., Amirkabir University of Technology, 2007
B.Sc., Islamic Azad University, Central Tehran Branch, 2005
December 2014

پیشکش به بهترین آموزگاران زندگیم، پدر و مادرم

# ACKNOWLEDGMENTS

First and foremost, I would like to acknowledge the endless support of my family (Maman, Baba, Hamed, and Kristen). I can never repay the immense debt I owe to my late father and my mother for their unending love and nurture. To my little brother, Hamed, whom I will always remember as a 4 year old boy in his pilot overalls. And to the most important human being, my beautiful fiancée, Kristen (who is sitting by my side at this moment complaining about how I am writing this).

I also would like to acknowledge my many devoted teachers that have helped me every step of the way. I thank my advisors Prof. M. M. Khonsari and Prof. B. Bourdin. I thank Prof. M. M. Khonsari for his support and patience over the years. I feel a deep debt of gratitude towards Prof. B. Bourdin for his endless guidance and the many hours I spent learning from him. I also would like to thank my committee members Dr. Devireddy and Dr. de Quieroz, and Dr. Tyagi, the dean representative in my committee.

I also want to thank my dear friends, Bamdad and Amirreza. I am privileged to know them both and cherish their friendship beyond anything. I thank Hessam, Kasra, Raysan, Navid, Ali, and Andrés for many good memories at LSU and for their constant support and friendship.

This work was supported in part by the National Science Foundation grant DMS-1312739. Some numerical experiments were performed using resources of the Extreme Science and Engineering Discovery Environment (XSEDE), which is supported by National Science Foundation grant number OCI-1053575 under the Resource Allocation TG-DMS060014.

# Table of Contents

# Abstract

In this study we present the variational approach to fracture mechanics as a versatile tool for the modeling of the fracture phenomenon in solids. Variational fracture mechanics restates the problem of initiation and propagation of cracks in solids as an energy minimization problem. The edifice of this energy minimization problem is such that unlike other methods (*e.g.,* extended finite element method XFEM, cohesive-zone methods) the variational approach to fracture mechanics, diminishes the need for an *a priori* knowledge of the crack path or *ad hoc* assumptions in the form of path selection laws. We will show applications of the variational approach to fracture mechanics to the thin-film and the classical two and three dimensional elasticity settings and to simulation of double-torsion experiments.

# CHAPTER 1
# INTRODUCTION

## 1.1 Historical background and motivation

Fracture mechanics has always been one of the important areas of focus for engineers. The proper advent of fracture mechanics in its modern form can be attributed to original work of Griffith [54] who framed the fracture problem as an energy minimization problem and concluded his paper with:

> The "theorem of minimum potential energy" may be extended so as to be capable of predicting the breaking loads of elastic solids, if account is taken of the increase of surface energy which occurs during the formation of cracks.

Despite this assertion subsequent progress in the field has been more focused on the local (*i.e.,* near field) properties of cracks. This was mainly due to the lack of the mathematical tools necessary to formulate and treat the problems arising from the elastic energy minimization in the presence of the cracks. In his celebrated work Irwin [61] connected the energy release rate from the tip of a crack (denoted by $G$) and the singularity of the elastic displacement field at the crack front (classically denoted by $K_I, K_{II}, K_{III}$ with the subscripts indicating the three classical crack propagation modes). Rice [97, 98] later connected the energy release rate rate from the tip of the crack to his famous path independent J-Integral. Consequently a host of analytical and numerical tools have been created to perform analysis and predict crack propagation paths based on methods dealing with the magnitude of these singularities; however, all these methods are limited either since an *a priori* knowledge of the crack path is needed or that an *ad hoc* assumption has to be made to work as a propagation criterion which both often results in inconsistencies (see for example [39, 37]).

The variational approach to fracture mechanics can be thought of as going back to Griffith's premise. Using the mathematical concepts and tools created in the past century,

the variational approach to fracture mechanics casts the original Griffith brittle fracture in terms of a *free discontinuity problem*. This approach was first proposed by Francfort and Marigo [49], while the first numerical treatment was later reported in [24]. A thorough review of the approach can be found in [25].

In the variational framework, the fracture problem is treated as an potential energy minimization of a two-fold total energy consisting of: (i) Internal energy stored in the solid, (ii) Fracture (surface[†]) energy, necessary to create a crack. The variational approach to fracture mechanics then posits that the pair of displacement and cracks will minimize this potential energy. Since the fracture problem is cast in the variational framework, a whole class of tools from calculus of variation and functional analysis become available. Over the next three sections we introduce the general concepts behind the variational approach to fracture mechanics.

### 1.2 Structure of variational approach to fracture mechanics

For a body of matter modeled as the $n$-dimensional domain $\Omega \subset \mathbb{R}^n$ containing the $(n-1)$-dimensional finite crack set $\Gamma \subset \Omega$, we define the total energy as the sum of the stored energy in the bulk $\mathscr{P}(u,\Gamma)$[‡] and the surface energy $\mathcal{S}(\Gamma;u)$ and write:

$$\mathscr{E}(u,\Gamma) := \mathscr{P}(u,\Gamma) + \mathcal{S}(u,\Gamma) \tag{1.1}$$

Although variational framework to fracture mechanics can be extended to non-elastic and nonlinear elastic cases we restrict ourselves here and write the bulk energy in terms of its local potential and external body ($f_b$) and surface ($f_s$) forces as:

$$\mathscr{P}(u,\Gamma) = \frac{1}{2}\int_{\Omega\setminus\Gamma} \mathcal{W}(u,\nabla u)\,dx - \int_{\Omega} f_b \cdot u\,dx - \int_{\partial_N\Omega} f_s \cdot u\,ds \tag{1.2}$$

[†]This is called the interchangeably surface energy, since in the sense of Griffith's theorem the fracture energy is associated with the creation of new surfaces.

[‡]We use the semicolon notation to show implicit dependence of the functionals.

where $\partial_N\Omega \subseteq \partial\Omega$ is the part of boundary of the domain with prescribed traction. Later in chapters 2-3 we will replace this local potential by its appropriate form to define the corresponding fracture problems in thin films and in isotropic elastic bodies.

Similarly, we define the surface energy required to create a crack set $\Gamma$ in its general form as:

$$\mathscr{S}(u,\Gamma) := \int_\Gamma G_c(x;[\![u]\!](x))\, d\mathcal{H}^{n-1} \tag{1.3}$$

where $\mathcal{H}^m$ is the m-dimensional Hausdorff measure (*i.e.,* $\mathcal{H}^2$ is a measure of the aggregate area and $\mathcal{H}^1$ is a measure of the aggregate length in three and two dimensions respectively) and $[\![u]\!]$ is the crack opening displacement (*i.e.,* jump of displacement $[\![u]\!] := |u^+ - u^-|$).

*Remark* 1.1. As highlighted by Barenblatt [13], Griffith's criterion imparts a dimension dependency characteristic by implicitly requiring that the bulk and the surface energy are comparable. In other words, since the bulk energy is proportional to the measure of volume and the surface energy is proportional to the measure of surfaces created, the fracture becomes configuration dependent as well as geometry dependent.

If for now we assume the crack path $\Gamma = \hat{\Gamma}$ is known and sufficiently smooth (it is rectifiable), the evolution of the fracture problem can be parameterized by a single parameter namely the crack length $l(t)$. It has been shown [49] the resulting minimization problem for the total energy (1.1) is equivalent to the following evolution problem:

**Definition 1.2.** The mapping pair $t \mapsto (u(t), l(t))$ is a quasi-static evolution for the displacement field and the crack tip along a prescribed curve $\hat{\Gamma}$. Given the initial crack length $l_0$ and the loading history $t \mapsto (\hat{u}(x,t), f_s(t), f_b(t))$ where $\hat{u}(x,t)$ is the prescribed displacement on part of boundary of domain $\partial_D\Omega(\cap\partial_N\Omega = \emptyset)$, it satisfies the initial condition $l(0) = l_0$ and evolves according to the following conditions for $t \in (0,T]$:

- Ireversibility condition: $\dot{l}(t) \geq 0$
- Stationarity: $(u(t), l(t))$ is a stationary point of (1.1).

- Energy balance: Total energy (1.1) is absolutely continuous on $[0,T]$ and satisfies energy balance:

$$\frac{d\mathscr{E}}{dt} = \int_{\partial_D\Omega\setminus\Gamma(l(t))} \nabla\mathcal{W}(u(t))\cdot\dot{\hat{u}}(x,t)\,dx - \int_\Omega f_b\cdot\dot{u}\,ds - \int_{\Omega_N} f_s\cdot\dot{u}\,ds \tag{1.4}$$

The evolution law 1.2 is equivalent to Griffith's classical formulation for sufficiently smooth cracks when the elastic energy of the body at equilibrium $\mathscr{P} : l \mapsto \inf_v(\mathscr{E}(u,\Gamma(l)))$ is strictly convex. Convexity of $\mathscr{P}$ is, in turn, related to the convexity of the local bulk energy potential $\mathscr{W}$ and the regularity of the loads and geometry. In case of strictly convex $\mathscr{P}$, the stationarity condition can be replaced by a minimality condition. Variational fracture mechanics takes a leap of faith and exploits this even in the case of non-convex $\mathscr{P}$, writing the evolution law as:

**Definition 1.3.** The mapping pair $t \mapsto (u(t),\Gamma(t))$ is a quasi-static evolution for the displacement field and the crack set. Given the initial crack set $\Gamma^0$ and the loading history $t \mapsto (\hat{u}(x,t), f_s(t), f_b(t))$ where $\hat{u}(x,t)$ is the prescribed displacement on part of boundary of domain $\partial_D\Omega(\cap\partial_N\Omega = \emptyset)$, it satisfies the initial condition $l(0) = l_0$ and evolves according to the following conditions for $t \in (0,T]$:

- Ireversibility condition: $\Gamma(t) \nearrow t$ (*i.e.,* $\mathcal{H}^{n-1}(\Gamma(t_1)) \geq \mathcal{H}^{n-1}(\Gamma(t_2))\,\forall t_1 \geq t_2$)
- Minimality: $(u(t),\Gamma(t))$ is a global minimum of (1.1) $\mathscr{E}(v,\Gamma)$ among all $\Gamma \supset \Gamma_t$ and $v = \hat{u}(x,t)\,\forall x \in \partial_D\Omega$
- Energy balance: Total energy (1.1) is absolutely continuous on $[0,T]$ and satisfies energy balance:

$$\frac{d\mathscr{E}}{dt} = \int_{\partial_D\Omega\setminus\Gamma} \nabla\mathcal{W}(u(t))\cdot\dot{\hat{u}}(x,t)\,dx - \int_\Omega f_b\cdot\dot{u}\,ds - \int_{\Omega_N} f_s\cdot\dot{u}\,ds \tag{1.5}$$

One can show the existence of a solution for the above problem in the setting of

anti-plane loading in [45] and under restrictive assumptions on crack geometry for two-dimensional elasticity in [34].

### 1.3 Initiation in brittle fracture

The fact that in definition 1.3 the stationarity is replaced by a global minimum pertains to one of the main issues with Griffith's brittle fracture model. As illustrated in [25] initiation can be achieved by the above evolution law in a finite time; however, this means a jump to a fracture state regardless of how far the cracked state is in the configuration space. A more in-depth study of the initiation problem suggests that, indeed, the initiation is a three parameter problem (namely: geometry length scale, Griffith's length scale, and a critical flaw length scale) that cannot be modeled accurately using the two dimensions available in Griffith's model. This problem can be palliated introducing a third length scale.

As seen in (1.3) the critical energy release rate $G_c$ in its most general form can depend on the crack opening $[\![u]\!]$. Griffith's theory in its original form assumes that there are no cohesive forces across the crack and, therefore, $G_c(x; [\![u]\!](x)) = G_c(x)$ only depends on the local material properties. However, more general behavior can be also modeled in the variational framework with little additional effort. Figure 1.1 shows a comparison of different models for energy release rate from the tip of a crack. Where Griffith's model predicts that as soon as the fracture opening is greater than a few atomic sizes the energy release rate is constant and equal to $G_c$, in other models – see for example Barenblatt's [13] or Dugdale's model [47] – the $G_c$ limit is based on an intrinsic length assumed .

The same effect as above can be achieved by non-local gradient damage models [94, 93], in which the damage is a continuous variable and there exist a length scale associated with the localization of these effects. Since these non-local damage models introduce softening as the damage progresses, stresses fall at the sight of damage but since the broad uniform

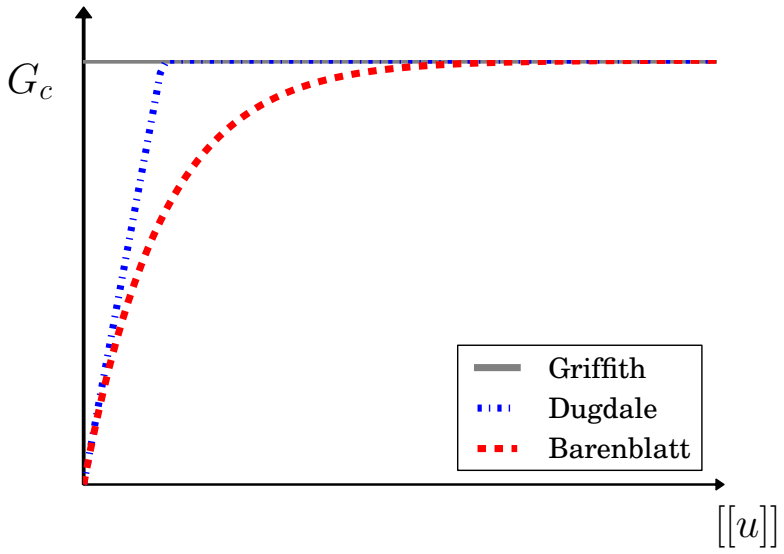


Figure 1.1: Comparison of energy release rate from the crack tip vs. crack opening displacement for Griffith (gray solid line), Dugdale (blue dash-dotted line), Branblatt (red dashed line)

damage is not energetically favorable it loses its stability and then localizes with a final optimum damage profile [91, 92].

### 1.4 Approximation and approximation of variational approach fracture

Implementation of the problem defined in definition 1.3 is prohibitively hard since we need suitable way to represent any crack set $\Gamma$ admissible. In this study we focus on two sets of polynomial approximations for the crack set $\Gamma$ and the measure of this crack set $\mathcal{H}^{n-1}(\Gamma)$ as first proposed by Ambrosio and Tortorelli in [6]. In this setting the crack set is replaced with a smeared fracture field $\alpha$ where $\alpha = 1\, a.e.\, \text{in}\, \Omega$ and goes to zero at the crack set. This essentially thickens the fracture set and introduces another length scale $\eta$ associated with the width of the fracture set profile. In this setting one can write an approximation for the total energy (1.1) as:

$$\mathscr{E}_\eta(u,\alpha) := \int_\Omega (1-\alpha)^2 \mathcal{W}(u)\, dx + \frac{1}{4C_\eta} \int_\Omega G_c(x,\alpha) \left( \frac{\alpha^m}{\eta} + \eta |\nabla \alpha|^2 \right) dx \tag{1.6}$$

where $m = 1, 2$ corresponds to two class of this approximation that we would call **AT1** and **AT2**, respectively. The constant $C_\eta$ is given by:

$$C_\eta = \int_0^1 \sqrt{\alpha^m}\, d\alpha \tag{1.7}$$

*Remark* 1.4. If we compare to the (1.6) with the gradient damage models of form:

$$\mathscr{E}_\eta(u, \alpha) := \int_\Omega E(\alpha)\mathcal{W}(u)\, dx + \int_\Omega (w(\alpha) + \eta E_0 |\nabla \alpha|^2)\, dx \tag{1.8}$$

we can easily see that **AT1** and **AT2** are easily reproducible with replacing $E(\alpha) = \alpha^2$ and $w(\alpha) = \frac{G_c}{4C_\eta \eta}$ and $E_0 = \frac{G_c}{4C_\eta}$. This gives tremendous insight and shows that indeed by using Amborosio and Tortorelli's approximation we are introducing another length scale to the problem that can be calibrated much like the length scale of the gradient damage models (see for example [92]).

*Remark* 1.5. One can note that the approximate energy (1.6) is convex with respect to the variable $\alpha$ and depending on convexity of $\mathcal{W}$ (as in case of linearized elasticity) is convex in displacement field $u$.

## 1.5 Structure of the dissertation

We introduced the basic ideas of variational fracture mechanics in this chapter. In Chapter 2 we will see an application of variational framework to fracture of thin films. As a result of the multi-dimensional nature of the geometry in the fracture of thin films, we will perform an asymptotic analysis and obtain a rescaled two-dimensional model that represents the original three-dimensional problem of thin-film fracture by decoupling the thin film from its underlying substrate. In Chapter 3 we will present a validation study on the variational framework. We will focus on a number of well-documented problems in two-dimensional and three-dimensional elasticity and validate the results of our numerical experiments by comparing them to the experimental results. We will also introduce a new

minimization scheme that will remedy some of the challenges of using variational fracture when dealing with abrupt crack propagations. In Chapter 4 we investigate fracture in double-torsion experimental technique and provide analysis of range of issues that can affect these experiments. Finally in Chapter 5 we will present a conclusion and a road-map to the future work.

# CHAPTER 2
# A VARIATIONAL APPROACH TO THE FRACTURE OF BRITTLE THIN FILMS SUBJECT TO OUT-OF-PLANE LOADING †

## 2.1 Abstract

We address the problem of fracture in homogenous linear elastic thin films using a variational model. We restrict our attention to quasi-static problems assuming that kinetic effects are minimal. We focus on out-of-plane displacement of the film and investigate the effect of bending on fracture. Our analysis is based on a two-dimensional model where the thickness of the film does not need to be resolved. We derive this model through a formal asymptotic analysis. We present numerical simulations in a highly idealized setting for the purpose of verification, as well as more realistic micro-indentation experiments.

## 2.2 Introduction

Thermal barrier coatings, thin-lubricant films, and electronic display devices are examples of applications in which the integrity of mechanical components depends largely on the integrity of a thin film of material applied on the surface of a substrate. The need to gain insight into the nature of thin films under various thermal and mechanical loadings has led to a large body of theoretical, experimental and numerical publications reviewed in detail in [83, 69]. Classical fracture mechanics has been widely used in the past few decades, and the majority of published works deal with the determination of critical load-

†This chapter has previously appeared as, Mesgarnejad, A., Bourdin, B., Khonsari, M., A Variational Approach To The Fracture Of Brittle Thin Films Subject To Out-of-plane Loading, Journal of Mechanics and Physics of Solids, 61(11):2360-2379, 2013. It is reprinted by permission of Elsevier for details see Appendix B.

ing for a pre-existing crack, usually growing on a pre-defined path. Such an assumption may be too restrictive when dealing with real life applications in which the nucleation point may be unknown and multiple cracks may be interacting or growing along unknown paths. Figure 2.1, for instance, shows fracture patterns obtained during micro-indentation experiments and illustrates how qualitatively and quantitatively different crack patterns arise for different scales or material properties.

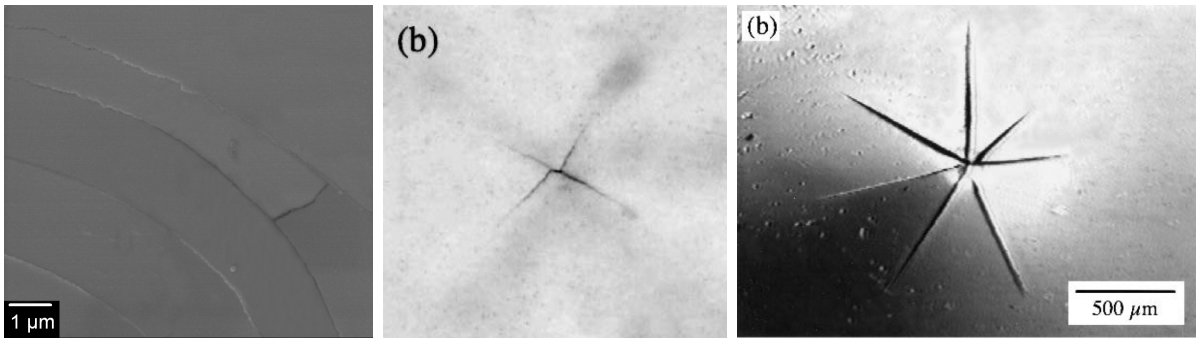


Figure 2.1: Micro-indentation experiments reproduced from [102, Figure 3] (left) and [69, Figure 7-8] (center, right); reproduced with permission.

To treat the problem of pre-tensioned films subject to in-plane displacements, Hutchinson and Suo [59] introduced a non-dimensional fracture driving force $Z = G/E_e$, where $G$ is the elastic energy release rate and $E_e$ is the stored elastic energy per unit volume of the material. Using this parameter, they were able to categorize different fracture patterns in thin films and, more specifically, showed cases where surface cracks occur or a network of channel fractures develops. More recently, Xia and Hutchinson in [110] developed a two-dimensional membrane model and derived solutions for a single crack and a network of parallel cracks, as well as spiral cracks based on linear fracture mechanics. Some of these solutions were recovered through a variational approach in [70]

Our aim in this paper is to examine the fracture of thin films with negligible thickness compared to the dimensions of the domain being analyzed, and in which transverse cracks span the entire cross-section of the film. We introduce a bulk energy consisting of two terms: the energy stored in the thin film and a Winkler foundation–type [103] energy due

to deformation in the bond between the thin film and the substrate. We justify these under specific scaling properties of the thickness and elastic properties of the film and bonding layers by an asymptotic analysis argument. This reduces the settings of our problem from three to two dimensions.

We propose to adopt the point of view of the variational approach to fracture mechanics [49, 23, 21, 25], which we adapt to our specific situation, in order to eliminate the reliance on *a priori* knowledge of the crack path or morphology. We build upon the work of [70], but focus on the out-of-plane deformation of a film perfectly bonded to an elastic substrate. The postulated evolution law is based on sequences of *unilateral global minimization* of a total energy consisting of the sum of a bulk energy associated with the elastic deformation of the thin film away from cracks and the surface energy due to creation of transverse cracks. The assumption of cracks propagating in a quasi-static setting is consistent with our focus on the asymptotic limit of a film of vanishing thickness and on cracks that are long compared to the thickness of the film.

We propose a numerical approach based on a regularized energy similar to the one presented in [23]. To verify our approach we focus on highly idealized situations, in particular in one-dimensional cases where exact solutions can be built. Using this relatively simple model, we are able to highlight several observed behaviors of cracks in thin films, including the nucleation of arrays of parallel cracks (see Sections 2.4 and 2.5.1), fracture branching, cell formation, and formation of networks of channel cracks (see Section 2.5.2).

The paper is organized as follows. In Section 2.3.1, we give the elastic and fracture energies for a static problem, and derive a model for quasi-static evolutions in Section 2.3.2. In Section 2.3.3, we propose a non-dimensional formulation. In Section 2.3.4, we present our numerical approach. Section 2.4 is devoted the verification of the numerical implementation in an idealized setting. In Section 2.5, we offer two more realistic numerical experiments highlighting the versatility of our formulation. Additionally, a numerical approach leading

to an exact solution of the one dimensional problem is presented in 2.7, and 2.8 is devoted to the formal derivation of our reduced model.

## 2.3 Variational model for fracture of a thin film

### 2.3.1 Formulation of the problem

A host of problems arises in applications that are based on a reduced dimensional formulation. Plate and shell models, in theory of elasticity, are examples of such a dimension reduction. Here we are interested in one such problem with an elastic homogenous thin layer bonded to a substrate. For the engineering minded reader, this model is similar to a plate with an elastic foundation [103].

We consider an elastic thin film bonded to the upper surface $\Omega \subset \mathbb{R}^2$ of the substrate $\mathscr{W} \subset \mathbb{R}^3$ by a Winkler type foundation. We denote the thin film's domain $\Omega_f = \Omega \times (0, h) \subset \mathbb{R}^3$ (see Figure 2.2). We focus on channel cracks $\Gamma_f = \Gamma \times (0, h) \subset \mathbb{R}^2$ in the thin film. We consider loading through an imposed displacement at upper surface of the substrate namely $w_t = w|_{\Omega \times \{0\}}$. Intuitively, it is reasonable to assume that the thin film does not carry any vertical load and that its deformation is driven by the movement of substrate [59]. In all that follows, the displacement of the substrate-film interface is supposed known *a priori*.

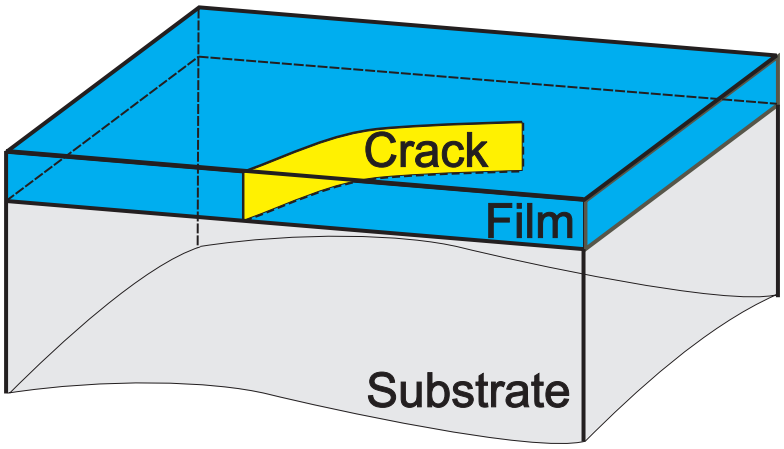


Figure 2.2: Problem's schematics

To use the variational approach to fracture mechanics, the potential energy of the system must be calculated. Our model applies to situations where where the dominant term in the elastic energy comes from bending effects. We account for a simplified configuration where the cohesive bond between the film and the substrate acts as an elastic highly anisotropic (essentially one-dimensional) medium (*i.e.,* a Winkler foundation). Rigorous validation of such a formulation requires examination of the three-dimensional elastic energies of the film and that of the cohesive bond when thicknesses of both layers approach zero. In fact, it is possible to rigorously derive the two-dimensional problem as a limit of a three-dimensional energy when thickness of the film approaches zero ($h \to 0$) using suitable scaling hypotheses. The derivation using asymptotic analysis can be found in 2.8.

*Remark* 2.1. The assumptions made while deriving the two-dimensional form of the energy translates to assumptions on the magnitude of the in and out-of-plane loadings. In terms of applications this implies:

- That thermal and residual stresses, as well as surface traction, are minimal. For cases like indentation of thin films this assumption seems valid since the in-plane normal stresses are largely due to the bending effects on the thin film.

- That the elastic modulus of the substrate in the vertical direction is small compared to its modulus in horizontal direction and also to that of the film. This applies to a film bonded on a compliant substrate such as the ones presented in [102, 96].

Using 2.8, the expression for the bulk energy can be written as the sum of the bending energy of thin film plus that of the Winkler foundation. We can write the bulk energy of the film and cohesive bond for vertical displacement $u \in H^2(\Omega \backslash \Gamma)$ of square integrable displacement fields with square integrable first and second derivatives as:

$$\begin{aligned} \mathscr{P}_t(u, \Gamma) &:= \int_{\Omega \backslash \Gamma} \mathcal{W}_b(u) dx + \int_{\Omega} \mathcal{W}_c(u, w_t)\, dx; \\ \mathcal{W}_b(u) &:= \frac{D}{2} W(\mathrm{D}^2 u)\, dx; \\ \mathcal{W}_c(u, w_t) &:= \frac{K}{2}(u - w_t)^2, \end{aligned} \tag{2.1}$$

where $\mathrm{D}^2$ represents the second derivative matrix defined as:

$$\mathrm{D}^2(v(x_1, x_2)) := \begin{bmatrix} v_{,11} & v_{,12} \\ v_{,12} & v_{,22} \end{bmatrix} \tag{2.2}$$

in two-dimensions, and where $W$ is the elastic potential associated with any 2 by 2 matrix $\Phi$ by

$$W(\Phi) := (\Phi_{11} + \Phi_{22})^2 - 2(1 - \nu)(\Phi_{11}\Phi_{22} - \Phi_{12}^2), \tag{2.3}$$

and $D$ and $K$ are the flexural stiffness of the film and the modulus of the Winkler foundation is defined as:

$$D := \frac{Eh^3}{12(1 - \nu^2)} \tag{2.4}$$

where $E, \nu$ are elastic modulus and Poisson's ratio for the thin film.

Following the variational approach to fracture mechanics, we model fracture as an energy-releasing mechanism, in which the energy released varies linearly with respect to the new surfaces formed. This is, in essence, the premise of Griffith's criterion. Since

we use a reduced two-dimensional formulation, where we lump the changes in thickness, cracks are simply reduced to one-dimensional entities that go through the film thickness, *i.e.* form channel cracks. Hence, the energy release is assumed to be proportional to the crack surface area:

$$\mathscr{S}(\Gamma) := hG_c\mathcal{H}^1(\Gamma) \tag{2.5}$$

where $\mathcal{H}^1$ is the one-dimensional Hausdorff measure (*i.e.*, $\mathcal{H}^1(\Gamma_t)$ is the aggregate length of the cracks) and $G_c$ is the critical elastic energy release rate associated with an infinitesimal increment of crack length.

Combining (2.1) with (2.5) yields the total potential energy:

$$\mathscr{E}_t(u,\Gamma) := \mathscr{P}_t(u,\Gamma) + \mathscr{S}(\Gamma) \tag{2.6}$$

### 2.3.2 Quasi-static evolution

Throughout this paper, we focus on a quasi-static evolution. For a crack set $\Gamma$, the admissible displacement set consists of functions $\mathscr{C}(\Gamma) := H^2(\Omega \setminus \Gamma)$. The evolution of the displacement field and associated crack set for a given loading history $w_t$ is given by the continuous evolution law (see [25] for instance):

**Definition 2.2. (Quasi-static evolution)** Given a loading sequence $w_t$ for $t \in [0, t_{max}]$, a function $t \to (u_t \in \mathscr{C}(\Gamma_t), \Gamma_t \subset \Omega)$ is the solution of quasi-static evolution if it satisfies:

1. Irreversibility of the crack evolution:

$$\Gamma_t \supseteq \Gamma_s, \ \forall\, 0 \leq s \leq t \tag{2.7}$$

2. Unilateral global stability. At any time $t$, the state $(u_t \in \mathscr{C}(\Gamma_t), \Gamma_t)$ is the global

minimizer of total energy among all admissible states:

$$\mathscr{E}_t(u_t, \Gamma_t) \leq \mathscr{E}_t(u, \Gamma),\ \forall u \in \mathscr{C}_t(\Gamma_t), \quad \forall\, \Gamma \supseteq \Gamma_t \tag{2.8}$$

3. Energy balance. The function $E(t) := \mathcal{E}_t(u_t, \Gamma_t)$ is absolutely continuous in $t$ and satisfies the condition

$$E(t) - E(0) = -\int_0^t \int_\Omega \sigma_t \frac{\partial w_t}{\partial t}\, dx\, dt \tag{2.9}$$

where $\sigma_t := K(u - w_t)$.

Since the process is assumed to be rate-independent, evolution in time is only accounted through the irreversibility condition. Thus, it is easy to see that up to rescaling of time, any monotonically increasing load can be replaced with a linear scaling of a reference load

$$w_t = t w_0. \tag{2.10}$$

where the parameter $t$ is merely a scaling factor; although this designation is admittedly imprecise, we occasionally refer to $t$ as "time".

### 2.3.3 Non-dimensionalization

We begin our analysis by providing a rescaled version of the total energy in equation (2.6). We consider the normalized space variable $\tilde{x} := x/x_0$, the normalized displacement $\tilde{u} := u/u_0$, and the normalized loading parameter $\tilde{w}_t := w_t/u_0$. In a similar fashion, we define $\tilde{\Omega} = \Omega/x_0 := \{x/x_0;\ x \in \Omega\}$, and $\tilde{\Gamma} = \Gamma/x_0 := \{x/x_0;\ x \in \Gamma\}$. Upon substituting the rescaled qualities in the expression of the total energy, we obtain

$$\frac{x_0^2}{u_0^2 D}\mathscr{E}_t(\tilde{u}, \tilde{\Gamma}) = \frac{1}{2}\int_{\tilde{\Omega}\setminus\tilde{\Gamma}} W(D^2\tilde{u})\, d\tilde{x} + \frac{1}{2}\frac{K x_0^4}{D}\int_{\tilde{\Omega}} (\tilde{u} - \tilde{w}_t)^2\, d\tilde{x} + \frac{G_c h x_0^3}{u_0^2 D}\mathcal{H}^1(\tilde{\Gamma}) \tag{2.11}$$

In what follows, we set $x_0 = u_0 = L$, where $L$ is some characteristic length of the domain $\Omega$. With this choice of parameters, we can rewrite (2.6) as:

$$\tilde{\mathscr{E}}_t(\tilde{u}, \tilde{\Gamma}) := \frac{1}{2} \int_{\tilde{\Omega} \setminus \tilde{\Gamma}} W(D^2 \tilde{u}) \, d\tilde{x} + \frac{\tilde{K}}{2\tilde{a}^4} \int_{\tilde{\Omega}} (\tilde{u} - \tilde{w})^2 \, d\tilde{x} + \frac{\tilde{G}}{\tilde{a}} \mathcal{H}^1(\tilde{\Gamma}) \tag{2.12}$$

where $\tilde{K}$, and $\tilde{G}$, and $\tilde{a}$ are dimensionless parameters defined as

$$\begin{cases} \tilde{K} := \dfrac{12Kh(1-\nu^2)}{E}, \\ \tilde{G} := \dfrac{12G_c(1-\nu^2)}{Eh}, \\ \tilde{a} := \dfrac{h}{L}. \end{cases} \tag{2.13}$$

*Remark* 2.3. The actual choice of the normalization parameters $x_0$ and $u_0$ is arbitrary. Another possible choice, similar to the one adopted in [70], is $x_0 = (D/K)^{1/4}$ and $u_0 = \sqrt{G_c h x_0^3 / D}$ so that all coefficients in (2.11) become equal to 1. Our choice leads to the domain size and displacement magnitude of the order of 1 and is motivated by our focus on the numerical implementation, at the expense of slightly more complicated expressions.

For the sake of conciseness and in order to simplify the notation, from this point on we omit the tilde on all fields, *i.e.* we write $u$ for $\tilde{u}$ and so on.

### 2.3.4 Numerical implementation

The variational approach to fracture frees itself from the need of an *a priori* knowledge of the crack path or specification of an additional *branching criterion*. Nevertheless, an implementation requires sophisticated numerical methods capable of dealing with free discontinuity problems. Specifically, the method requires performing the minimization of the total energy with respect to *any* kinematically admissible displacement field $u$ and *any* cracks defined by a curve or set of curves $\Gamma$. The method is derived from the one presented in-depth in [25] and references therein. In what follows, we give a brief overview of the method focusing on the necessary changes required to deal with the biharmonic problem and refer the interested reader to the aforementioned references for more details.

Following the approach pioneered in [4] for an image segmentation problem and studied in-depth in [28], we introduce a regularization parameter $\eta > 0$ homogeneous to a length and a secondary variable $\alpha$ taking its values in $(0, 1)$ to represent the presence of cracks (in a sense to be clarified further below). We define the regularized energy

$$\mathscr{E}_{t,\eta}(u, \alpha) := \mathscr{P}_t(u, \alpha) + \mathscr{S}_\eta(\alpha), \tag{2.14}$$

where

$$\mathscr{P}_t(u, \alpha) := \frac{1}{2} \int_\Omega (1 - \alpha)^2 W(D^2 u)\, dx + \frac{K}{2a^4} \int_\Omega (u - w_t)^2\, dx, \tag{2.15}$$

and

$$\mathscr{S}_\eta(\alpha) := \frac{3G}{8a} \int_\Omega \frac{\alpha}{\eta} + \eta |\nabla \alpha|^2\, dx. \tag{2.16}$$

In the setting of the Mumford-Shah functional or of anti-plane shear, the behavior of the regularized problem can be rigorously established. More specifically, it can be shown that as $\eta \to 0$, $\mathscr{E}_{t,\eta}$ converges to $\mathscr{E}_t$ in the sense of $\Gamma$–convergence. From there, it is easily seen that the global minimizer of $\mathscr{E}_{t,\eta}$ converges to that of $\mathscr{E}_t$ as $\eta \to 0$. Roughly speaking, as $\eta \to 0$, the displacement field minimizing (2.14) becomes arbitrarily close to that of minimizing (2.12), and that the $\alpha$ field converges to 1 "near the jumps of $u$" (*i.e.*, the cracks) and to 0 almost everywhere else. This $\Gamma$–convergence result can be extended further to encompass the entire discrete and then continuous time evolution (see [53]). These results are mathematically complex and we do not attempt to extend them to our setting. Instead, we assume that they hold in the case of a bi-harmonic bulk term and proceeded by induction. We believe that the numerical results presented further along in Section 2.4 and 2.5 give credit to this assumption, even though, admittedly, they are no substitute for a formal proof.

The numerical implementation and, in particular, the minimization strategy of (2.14) is now regarded classical. Following [25], by considering a discrete set of loading parameters $t_i$ and for a given choice of the regularization parameter $\eta$, we seek sequences of minimizers

of the regularized energy. At each time step, the crack growth condition (2.7) is accounted for through the addition of constraints on the field $\alpha$. Namely, for each $t_i$, we solve the following minimization problem:

$$(u_i, \alpha_i) = \underset{\substack{u_i \in \mathcal{K}_A \\ \alpha_i \in \mathcal{A}_\epsilon(\alpha_{i-1})}}{\arg\min} \; \mathscr{E}_{t,\eta}(u, \alpha), \tag{2.17}$$

where $\mathcal{K}_A(t_i)$ denotes the set of kinematically admissible displacements and $\mathcal{A}$ is defined by

$$\mathcal{A}_\epsilon(\alpha) = \{x \in \Omega \,;\, \alpha(x) < 1 - \epsilon\}\,, \tag{2.18}$$

and $\epsilon$ is some arbitrarily small parameter.

The actual minimization of (2.14) is achieved using a combination of alternate minimizations and a backtracking algorithm. At each time step, we iterate minimization with respect to $u$ and $\alpha$ until the results converge. In this algorithm, the first step to obtain $u$ is a simple convex problem which is implemented by solving the associated Euler-Lagrange equation (*i.e.*, the elasticity problem) using the method of finite differences. The second step to solve for $\alpha$ is to apply a bounded Trust Region Newton minimization scheme for the discrete energy. Upon convergence of the alternate minimizations algorithm, we compare the results to all the previous loading steps in order to avoid settling on *some* local minimizers (see [21] for more details on the backtracking idea). Of course, we cannot claim that this approach *always* leads to a global minimizer. In some situations, we were able to compute the actual global minimizer of the regularized energy using dynamic programming and compare the results with the outcome of our minimization strategy (see Section 2.4.2 ).

Our implementation relies on the distributed data structures and linear algebra provided by PETSc [12, 10, 11], whereas the constrained optimization problems are solved using TAO [86].

The astute reader will also have noticed the similarity between the regularized functional (2.14) and non-local gradient damage [94] or phase field [56, 57, 64] models. In these models, the regularization parameter is given a physical interpretation (*e.g.*, internal length, interaction distance). However, our approach is somewhat different. The parameter $\eta$ is treated purely as a numerical artifact of the energy functional (2.14), which itself is treated as an intermediate expression in a two-step numerical method based on regularization followed by discretization. In short, our model is based on the minimization of a free discontinuity energy (2.12) and the specific form of its regularization (2.15) bears no special physical significance.

## 2.4 A one-dimensional verification problem

Under restrictive enough hypothesis on the loading, the geometry of the domain, and the structure of the solution, it is possible to build a closed-form (but non-trivial) solution of our model. This highly idealized situation provides valuable insight into the properties of the proposed model, and will allow us to provide some element of *verification* of our numerical implementation. We consider an elongated rectangular domain $\Omega = \omega \times (-l_y/2, l_y/2)$ where $\omega$ is some interval and $l_y \ll 1$, and assume that the loading function $w_t$ depends only on $x$ (Figure 2.3).

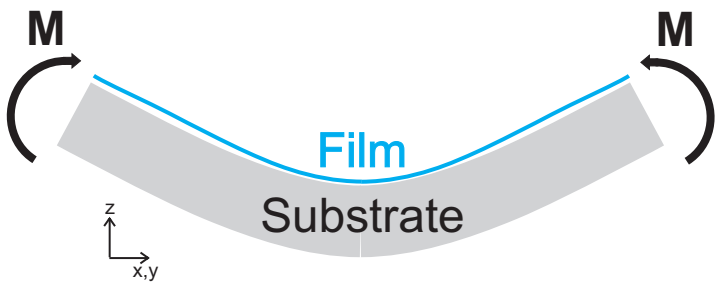


Figure 2.3: Pure-bending problem schematic.

In this situation, it is natural to consider only displacement fields that depend on $x$

and transverse cracks in the form $\Gamma = \gamma \times (-l_y/2, l_y/2)$ when $\gamma$ consists of a discrete set of points in $\omega$. Introducing the function $v_t := u - w_t$, we define rescaled elastic, surface and total energies as:

$$E_t(v_t, \gamma) := P_t(v_t, \gamma) + S(\gamma), \tag{2.19}$$

where one-dimensional bulk energy $P_t$, and one-dimensional surface energy $S$ are defined as:

$$P_t(v_t, \gamma) := \frac{1}{l_y}\mathscr{P}_t(u, \Gamma) = \frac{1}{2}\int_{\omega\setminus\gamma} (v_t'' + w_t'')^2\, dx + \frac{K}{2a^4}\int_\omega v_t^2\, dx, \tag{2.20}$$

$$S(\gamma) := \frac{1}{l_y}\mathscr{S}(\Gamma) = \frac{G}{a}\#(\gamma), \tag{2.21}$$

and $\#(\gamma)$ denotes the counting measure of $\gamma$ (*i.e.*, the number of points in $\gamma$.)

In the 1-D case, we adopt a slightly different viewpoint by focusing on the film's fragments instead of its crack points. Given any interval $\omega$, we note that the choice of a countable family of $n$ points $\gamma = \{x_1, \cdots, x_n\}$ is exactly equivalent to partitioning $\omega$ into $n+1$ disjoint open intervals $\{\omega_0, \omega_1, \ldots, \omega_n\}$ such that $\omega_i \cap \omega_j = \emptyset$ if $i \neq j$ and $\bigcup_{0\leq i\leq n} \bar{\omega_i} = \bar{\omega}$. With a slight abuse of notation, for any such partition $\mathscr{X} = \{\omega_0, \ldots, \omega_n\}$ and any displacement field $v_t$ twice differentiable in each $\omega_i$ we define

$$E_t(v_t, \mathscr{X}) := P_t(v_t, \mathscr{X}) + S(\mathscr{X}), \tag{2.22}$$

where

$$P_t(v_t, \mathscr{X}) := \frac{1}{2}\sum_{i=0}^{n} \left[\int_{\omega_i} (v_t'' + w_t'')^2\, dx + \frac{K}{2a^4}\int_{\omega_i} v_t^2\, dx\right] \tag{2.23}$$

$$S(\mathscr{X}) := \frac{G}{a}\left[\#(\mathscr{X}) - 1\right], \tag{2.24}$$

Hereafter, we focus on a specific choice of the loading function $w_t(x) = \frac{-tx^2}{2}$ for which the elastic energy becomes

$$P_t(v_t, \mathscr{X}) = \frac{1}{2}\sum_{i=1}^{n+1}\left[\int_{\omega_i}(v_t'' - t)^2\,dx + \frac{K}{2a^4}\int_{\omega_i} v_t^2\,dx\right]. \tag{2.25}$$

Despite its similarity with the problem of a homogeneous elastic membrane under constant in-plane strain studied in [110, 70], the minimization of $E_t$ is much more challenging as we will see below.

### 2.4.1 An explicit formula for the total energy of a film broken into $n+1$ fragments.

We start our analysis by providing an explicit formula for the total energy of a film in elastic equilibrium. First, we write the elastic energy of a single fragment of length $l$ free at both ends, noting that the modified elastic energy (2.25) is invariant by translation, so that the actual position of the fragment (*i.e.*, choice of $\mathscr{X}$) plays no role.

Consider an unfractured film occupying an interval $\omega_k = (x_k, x_{k+1})$ of length $l = x_{k+1} - x_k$. Up to a translation, the modified displacement $v_t$ is given by the minimizer of

$$P_t(v_t, \{(-l/2, l/2)\}) = \int_{-l/2}^{l/2}(v_t'' - t)^2\,dx + \frac{K}{2a^4}\int_{-l/2}^{l/2} v_t^2\,dx, \tag{2.26}$$

leading to the Euler-Lagrange equations

$$v_t^{(4)} + \frac{K}{a^4}v_t = 0, \tag{2.27}$$

subject to the traction-free boundary conditions

$$v_t''(\pm l/2) = t,\ v_t^{(3)}(\pm l/2) = 0. \tag{2.28}$$

After some tedious algebra, one obtains an explicit expression for the minimizing modified

displacement:

$$
\begin{aligned}
v_t^*(x) = \frac{2}{\lambda^2\left(\sin(\lambda l)+\sinh(\lambda l)\right)}\Big[ & -\cos\left(\tfrac{\lambda l}{2}\right)\sinh\left(\tfrac{\lambda l}{2}\right)\sin\left(\lambda x\right)\sinh\left(\lambda x\right) \\
& +\sin\left(\tfrac{\lambda l}{2}\right)\cosh\left(\tfrac{\lambda l}{2}\right)\cos\left(\lambda x\right)\cosh\left(\lambda x\right) \\
& -\cos\left(\tfrac{\lambda l}{2}\right)\sinh\left(\tfrac{\lambda l}{2}\right)\cos\left(\lambda x\right)\cosh\left(\lambda x\right) \\
& -\sin\left(\tfrac{\lambda l}{2}\right)\cosh\left(\tfrac{\lambda l}{2}\right)\sin\left(\lambda x\right)\sinh\left(\lambda x\right)\Big],
\end{aligned}
\tag{2.29}
$$

and for the associated elastic energy:

$$
E_t^*(l) := \frac{t^2}{2}\left(l + F_\lambda(l)\right), \tag{2.30}
$$

where $\lambda := \frac{K^{1/4}}{a\sqrt{2}}$ is an internal scaling factor that represents the ratio between cohesive energy and bending energy, and the function $F_\lambda$ is defined by

$$
F_\lambda(l) := \frac{2\left(\cos(\lambda l)-\cosh(\lambda l)\right)}{\lambda\left(\sin(\lambda l)+\sinh(\lambda l)\right)}. \tag{2.31}
$$

Figure 2.4 shows the elastic energy $E_t^*(l)$ and function $F_\lambda(l)$ as a function of the fragment length $l$ for several values of the internal scaling factor $\lambda$. It is worth noting that the linear part of the energy is simply due to the work of imposed moments (*i.e.*, $v_t'' = t$) and the non-linear scaling function is due to the work of the modified displacement (*i.e.*, $v_t^*$).

Using (2.30), it is easy to obtain a general formula for the total energy of a film broken into $n+1$ fragments, summarized as follows.

**Proposition 1.** *Consider a partition $\mathscr{Y} = \{I_0, \cdots, I_m\}$ of an interval $I$. Let $v_t^*$ be the equilibrium modified displacement associated with the loading $w_t(x) = -tx^2/2$,* i.e., *$v_t^*|_{I_j} = \arg\min_v E_t(v, \{I_j\})$. Then, the total energy associated to $\mathscr{Y}$ is*

$$
E_t^*(\mathscr{Y}) := E_t(v_t^*, \mathscr{Y}) = \frac{t^2}{2}\left(|I| + \sum_{j=0}^{m} F_\lambda(|I_j|)\right) + \frac{mG}{a}, \tag{2.32}
$$

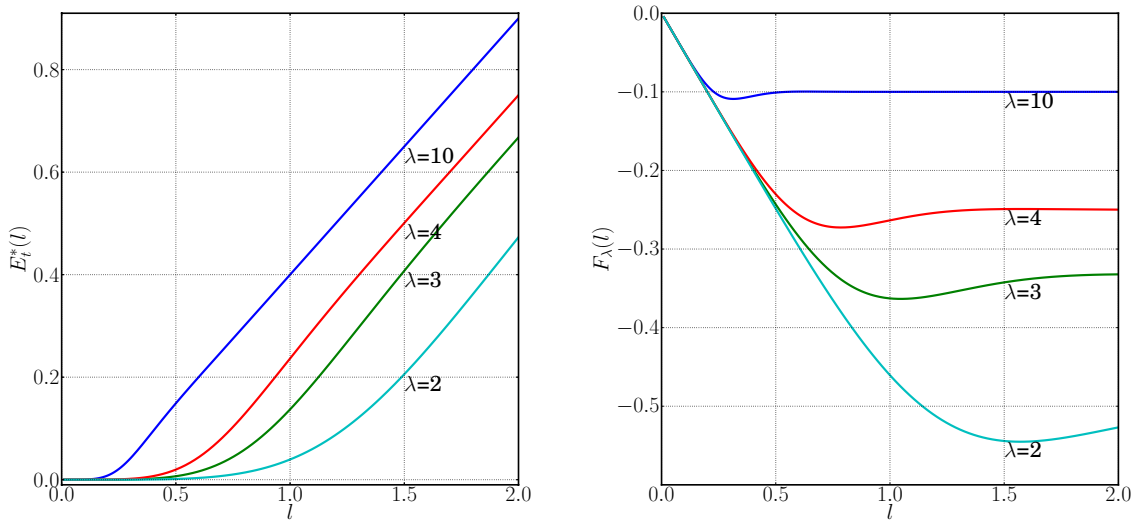


Figure 2.4: Elastic energy (2.30) of fragment of length $l$ with traction-free boundary conditions on both ends at unit load $t = 1$ (left) and scaling function $F_\lambda(l)$ (2.31)(right) as a function of $l$ for various values of $\lambda$.

*if* $m > 0$, *and*

$$E_t^*(\mathscr{Y}) := E_t(v_t^*, I) = \frac{t^2}{2}\left(|I_0| + F_\lambda(|I_0|)\right) \tag{2.33}$$

*otherwise.*

In the case of the homogenous elastic membrane under constant in-plane strain in [70], a simple argument of convexity for the equivalent of $F_\lambda$ leads to the conclusion that for a given value of $n$, the partition $\mathscr{X}$ minimizing $E_t^*(\mathscr{X})$ consists of $n$ equal length fragments in $\omega$. Here, $F_\lambda$ is non-convex and such a result does not hold true *a priori*, which renders obtaining a closed-form minimizer for $E^*(t)$ much more challenging. Instead, we use a dynamic programming technique inspired by [33] to compute the true global minimizer of the total energy, and illustrate via examples that the optimal crack configuration may not result in fragments of equal length. n the next two sections, we use exact solutions obtained by a dynamic programming algorithm to verify the numerical implementation of the regularized functional (2.14). The details of this algorithm are presented in 2.7.

### 2.4.2 Comparison with the elliptic regularization approach

A major hurdle is the stiffness of the elastic term in the regularized energy. Substituting $\lambda$ in (2.15), it is clear that for small values of $\lambda$, the minimization of the total energy with respect to the displacement field becomes numerically ill-conditioned. Since realistic situations correspond to large values of the parameter $\lambda$, we chose to partially ignore this issue: we implemented a one dimensional version of the regularized energy by means of finite differences on a regular grid, which we used to replicate the experiments in Figure 2.15-2.16. We then focused on the more realistic situations using two-dimensional finite differences.

In this section, we used the one-dimensional implementation of the regularized energy (2.14) for the problem in Figure 2.15. Figure 2.5 (left) compares each component of the fracture energy obtained with both methods, while the displacement $v_t$ and fracture $\alpha$ fields are plotted on the right, respectively, after the first and second crack nucleation ($t = 1, 2$). The space discretization consists of 800 grid points ($\delta_x = 6.25 \times 10^{-4}$), while the loading interval $0 \leq t \leq 3.0$ is discretized in 100 time steps and the regularization parameter is $\eta = 10\delta_x$. The backtracking algorithm from [21] was used in order to ensure energy balance at the crack nucleation loads. The agreement between both models, in terms of value of the energies, critical loads at nucleation and crack location is excellent.

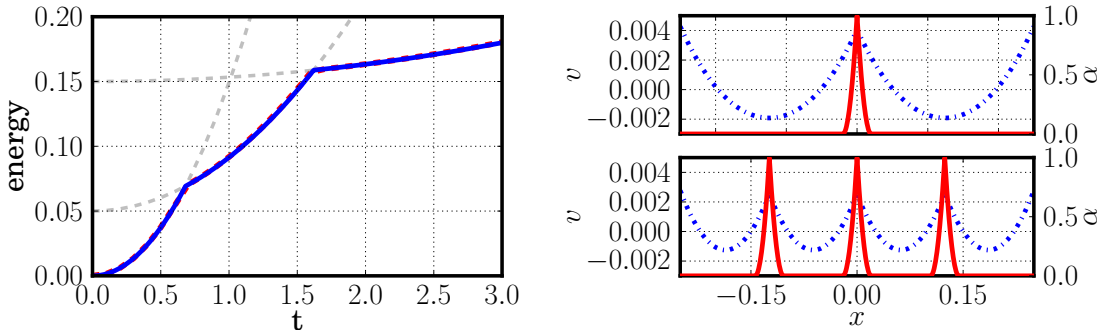


Figure 2.5: Fracture of a one-dimensional sample uniformly loaded. Comparison between the dynamic programing solution from Figure 2.15 and the minimization of the regularized energy (2.14) with $\lambda = 10$, $l_0 = 0.5$, $Ga^{-1} = 0.05$, $\eta = 10\delta x$. Left: total energy as a function of the loading (blue solid line) compared to the dynamic programming solution (dashed lines). Right: displacement $u$ (blue dotted line) and $\alpha$ field (red solid line) at $t = 1.0$ (top) and $t = 2.0$ (bottom)

In Figure 2.6, the same process is repeated for the computation leading to an asymmetric crack pattern shown in 2.16. Here, the agreement is not as good. Whereas dynamic programming computations predict that single cracks should be nucleated respectively at $x = -0.06$, $x = 0.22$, and $x = -.28$ at $t = 0.67, 0.73$, and $0.91$, alternate minimizations of (2.14) lead to the nucleation of two symmetric cracks at $x \simeq \pm 0.09$ at $t \simeq 0.75$, followed by the nucleation of two more cracks at $x \simeq \pm 0.24$ at $t \simeq 1.09$. Figure 2.6 (left) compares the total energy obtained with our dynamic programing algorithm (solid blue line) to that obtained through numerical minimization of (2.14), and highlights the difficulty of this problem. Note in particular how the solution with two symmetric cracks obtained with the alternate minimizations algorithm enhanced with the backtracking scheme is close to the global minimizer. Yet it appears to be a stable critical point of the regularized energy. Notice also how the optimal 3-crack configuration is not achievable from the two-crack configuration by virtue of irreversibility. This explains how the second bifurcation takes place at a higher loading value in the numerical simulation based on minimization of (2.14).

That the alternate minimizations algorithm fails to properly identify the proper solution is not a surprise, since it can only be shown to converge to a critical point of the energy. Thus, by virtue of its non-convexity, it may admit many local minimizers. In fact, whereas the variational approach to fracture postulates that crack nucleation is given by global minimizers of a non-convex energy, in the numerics what often triggers such events is the stability of the elastic solutions (see [94]). A continuation method, similar to the one implemented in [74] may be useful here, but was not tested, as we focused our attention towards more realistic situations.

We conclude this section by focusing on an example with more realistic parameters, which we can use for the verification of our two-dimensional finite difference implementation. We consider a two dimensional domain $\Omega = (-0.5, 0.5) \times (-0.1, 0.1)$ discretized by a $300 \times 60$ grid ($\delta x = 3.3 \times 10^{-3}$). The internal scaling factor is $\lambda = 31.6$, and the regularization parameter is $\eta = 5\delta x$. Figure 2.7 shows the comparison between the global

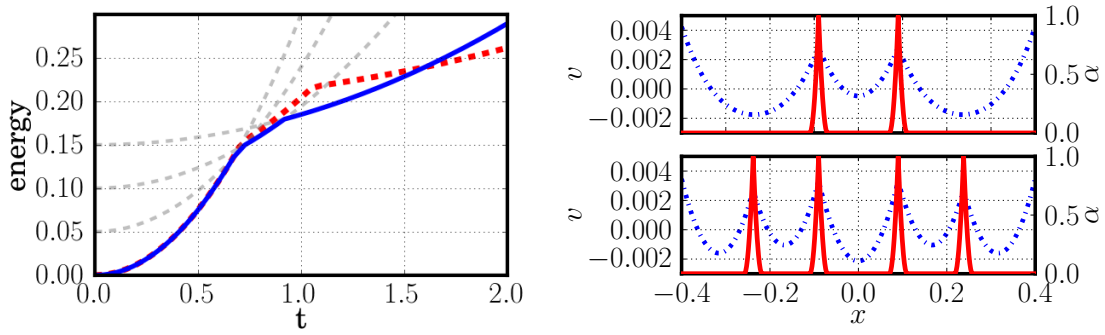


Figure 2.6: Fracture of a one-dimensional sample uniformly loaded. Comparison between the dynamic programing solution from Figure 2.16 and the minimization of the regularized energy (2.14) with $\lambda = 10$, $l_0 = 0.8$, $Ga^{-1} = 0.05$, $\eta = 10\delta x$. Left: total energy as a function of the loading (blue solid line) compared to the dynamic programming solution (red dashed line). Right: displacement $u$ (blue dotted line) and $\alpha$ field (red solid line) at $t = 0.8$ (top) and $t = 1.5$ (bottom)

minimizer of the energy $\mathscr{E}_t$ obtained by dynamic programming and the energy of discrete regularized energy $\mathscr{E}_{t,\eta}$. The backtracking algorithm described in [25] was used to avoid some classes of local minimizers and ensure energy balance.

As can be seen in Figure 2.7, even with a relatively large regularization parameter $\eta$, the total energy of the numerical solution is very close to that of the global minimizer for the one-dimensional problem. Also note that the total energy obtained from two-dimensional numerical solution is smaller compared to that of the true one-dimensional global minimizer which can be attributed to the two-dimensional features near the boundary $x_2 = \pm ly/2$ (see Figure 2.7). Note also that while the surface and elastic energies of the numerical solutions are overall close to that of the global minimizer, one observes some discrepancy when the loading parameter $t$ is such that $4.5 \leq t \leq 6$. This can be explained by two properties of our numerical solutions. Firstly, when $4.5 \leq t \leq 6$, our numerical solution is not the translation of a one-dimensional crack pattern (see in Figure 2.7 how at the onset of nucleation, the cracks only span parts of the cross section of our domain). Also, before crack nucleation, we observe that the $\alpha$ field does not remain near 0. This leads to a softening effect similar to that of distributed damage. As the regularization parameter $\eta$ becomes smaller, this effect should progressively vanish. For larger loads the fracture field $\alpha$ remains overall

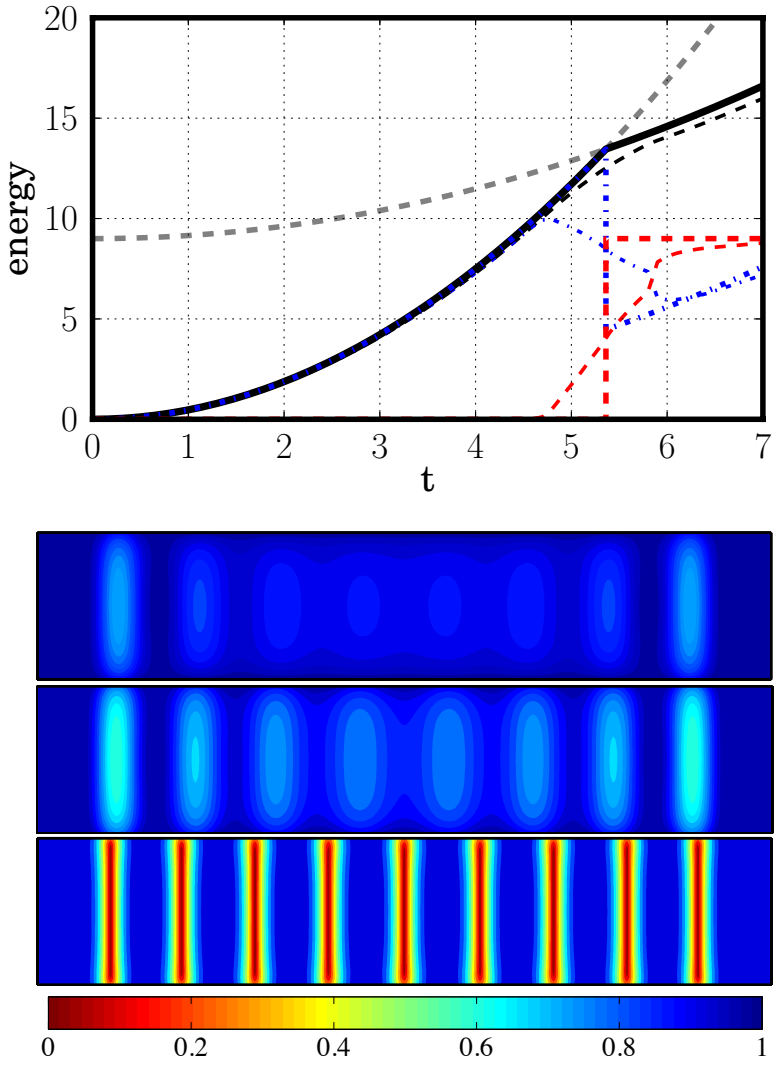


Figure 2.7: Fracture of a two-dimensional sample under pure bending. Comparison between the dynamic programing solution from Figure 2.18 and the minimization of the regularized energy (2.14) with $\lambda = 31.6$, $l_0 = 1$, $Ga^{-1} = 1$, $\eta = 5\delta x$. Evolution of the energy (black: total, blue: energy, red: surface energy) and comparison with the 1d global minimizer (thick lines) (top), fracture field $\alpha$ at $t = 5, 5.4, 5.8$ (from top to bottom).

near 0, with smooth but well-focused transitions to 1 at $x = \pm 0.4, \pm 0.3, \pm 0.2, \pm 0.1, 0.0$, corresponding to the 9 cracks observed in the global minimizer (see Figure 2.18).

## 2.5 Numerical simulations

While previous section is mostly concerned with verification of our implementation based on a highly idealized problems with little regard for the physical relevance of the

rescaled material properties, we also focused on two more realistic problems. We first describe the fracture of a film coating on a cantilever beam then the a spherical indentation of a film on compliant substrate.

### 2.5.1 Coated cantilever beam

In order to simulate the transverse crack on a thin film coating a cantilever beam, we considered a rectangular domain $\Omega = (0, l_x) \times (-ly/2, ly/2)$ subject to a substrate displacement $w_t = tx^2(3l_x - x)$ corresponding to clamping the edge $x = 0$ and applying a point force of magnitude $F = -t/6$ at $x = l_x$ (Figure 2.8). We chose for unit of length $L = l_x$ in (2.12) so that our computational domain corresponds to a rectangle of unit length and height $l_y/l_x$, which we discretized with a uniform grid of $400 \times 40$ cells. We focused instead on the minimization of the regularized energy (2.14) over adapting the dynamic programing algorithm.

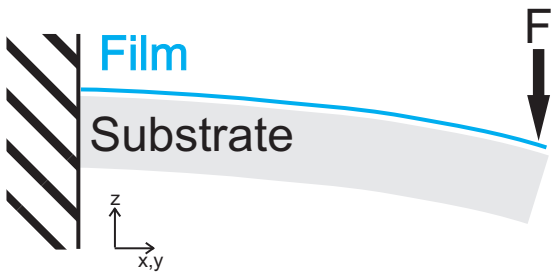


Figure 2.8: Coated cantilever beam problem schematic

Figure 2.9 shows snapshots of the fracture field a multiple increments of the loading parameter $t$. Again, we observe the progressive nucleation of an array of equidistant transverse cracks, growing from the clamped end towards the loaded end of the domain. The characteristic crack spacing appears to depend most strongly on the non-dimensional cohesive stiffness $Ka^{-4}$. Qualitatively, this behavior is similar to the one observed in [25, sec. 6] for the in-plane loading of a layered material. Figure 2.10 shows the evolution of the elastic, surface and total energy for these two cases. Interestingly, it appears that after a

loading phase during which the elastic energy grows as a quadratic function of the loading parameter, its growth become linear. This suggests that asymptotically, when the length of the domain becomes large compared to the crack spacing, the effective mechanical behavior associated with the growing network of parallel cracks is that of a damaged region growing from the left edge of the domain at the same rate.

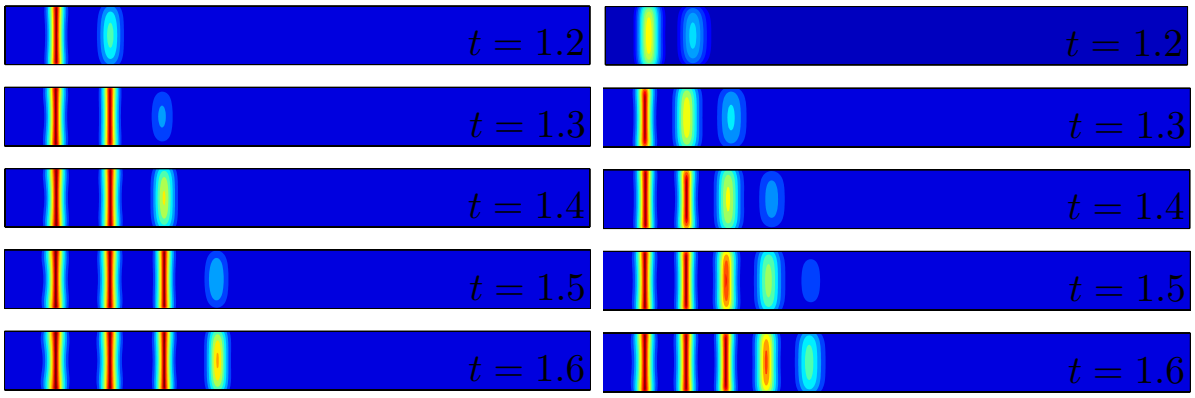


Figure 2.9: Fracture of a two-dimensional coated cantilever beam with $L = 1.0$, $Ga^{-1} = 1.$, $\eta = 5\delta x$: (left) $Ka^{-4} = 6 \times 10^6$, (right) $Ka^{-4} = 1.2 \times 10^7$.

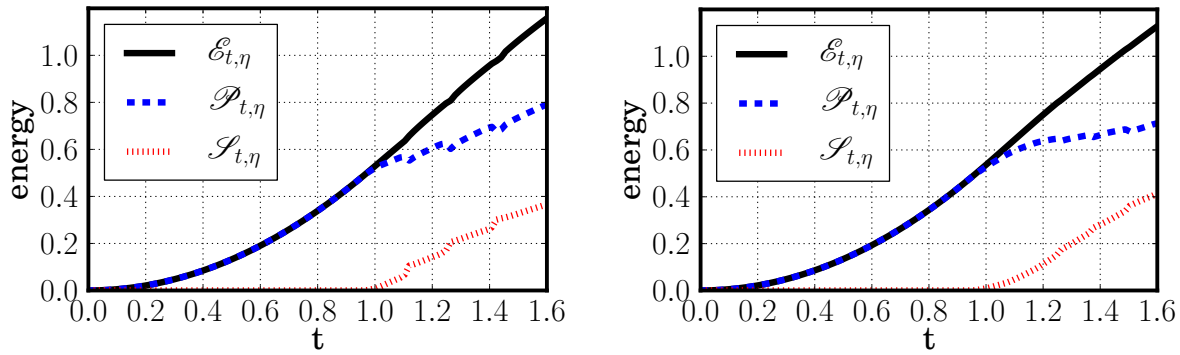


Figure 2.10: Evolution of the elastic, surface end total energies for a two-dimensional coated cantilever beam with $l_0 = 1.0$, $Ga^{-1} = 1.$, $\eta = 5\delta x$: (left) $Ka^{-4} = 6 \times 10^6$, (right) $Ka^{-4} = 1.2 \times 10^7$.

### 2.5.2 Indentation of thin films

We finally present numerical simulations indentation experiments of thin films, a truly two-dimensional problem of significant importance commonly used as testing methodology to measure different physical properties of thin films [68, 76, 85]. We considered a two-dimensional domain $\Omega = (-0.5, 0.5)^2$ discretized by a structured mesh consisting of $1500 \times$

1500 nodes ($\delta x = 0.0025$) with regularization parameter $\eta = 5\delta x = 0.005$. We consider the action of a spherical indenter centered at $(0, 0, R(1-t))$ from the film surface, $t$ being as usual the loading parameter. Figure 2.11 shows the settings of the problem. The displacement of the substrate is given by

$$W_t(x,y) = \begin{cases} 0 & \text{if } x^2 + y^2 \geq R^2 t(2-t), \\ R(1-t) + \sqrt{R^2 - x^2 - y^2} & \text{otherwise,} \end{cases}$$

*i.e.,* we neglect the deflection of the substrate unless it is in contact with the indenter. This is essentially similar to assuming a fully plastic substrate, and consistent with the experimental literature for very flexible substrate [32, 102]. Also since this loading is not monotonically increasing, we did not use the backtracking algorithm.

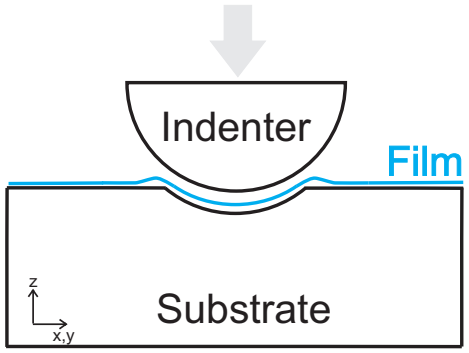


Figure 2.11: Schematics of the micro-indentation problem.

Figure 2.12 shows snapshots of the evolution of the fracture field $\alpha$ for increasing values of the loading parameter. The values for non-dimensional fracture toughness $G = 5 \times 10^{-3}$ was calculated based on fracture toughness of Indium Tin Oxide (ITO) films as shown in Table 2.1 for a film of thickness $h = 0.1\,\mu$m. The value of $K$ was then calibrated based on the experimental observation. We did not attempt at performing a full quantitative comparison with experiments. However, features of our numerical simulations compare

favorably with experiments and common observations. In particular, the combination of circular cracks linked by smaller radial cracks was observed in [102, Figure 3] reproduced here in Figure 2.1.

Figures 2.13 and 2.14 show sets of radial cracks obtained for two set of parameters corresponding to a thiner film or a larger indenter radius compared to that of the numerical experiments in Figure 2.12. This cracks geometry is reminiscent of experiments presented in [69, Figure 7-8], which were reproduced in Figure 2.1. In an actual experiment, one observes that ring cracks evolve from the contact edge downward whereas radial cracks evolve from the interface upward. This behavior can not be accounted for in our model as we assume that cracks always tunnel through the entire thickness of the film. Instead, we observe that cracks nucleate with a strictly positive length, which is consistent with the analysis of [38]. These cracks propagate with increasing load until the high values of $t$ where ring cracks initiate at their outer radii. We can, however replicate some common observations of thin-film fracture; in particular, perpendicular crossing of fracture path in Figure 2.13 and 120° branching of cracks in Figure 2.14. Furthermore, in Figure 2.14 one can see that as the non-dimensional fracture toughness of the film is reduced, there is transition from one branch (Figure 2.14 (left)) to two very close branches (Figure 2.14 (center)) and finally the distancing of the branching points (Figure 2.14 (right)). This is similar to the observations made by Maurini, et al. [74] for drying driven fractures.

Table 2.1: Physical properties of Indium Tin Oxide

| Young Modulus [113] | Critical Stress Intensity Factor $K_{IC}$ [40] |
|---|---|
| $99.8 \pm 13.6\,\mathrm{GPa}$ | $2.2 \pm 0.3\,\mathrm{MPa}\sqrt{\mathrm{m}}$ |

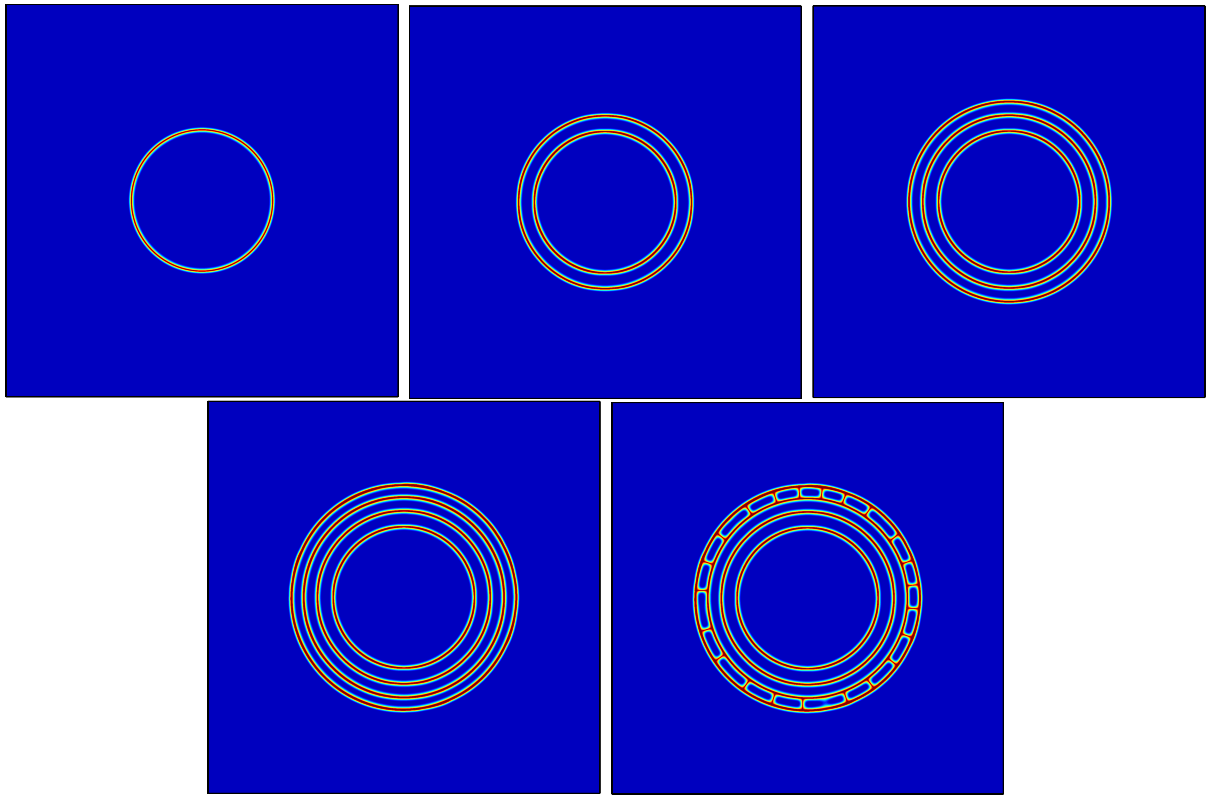

Figure 2.12: Fracture of a two-dimensional thin-film with compliant substrate under spherical indenter of radius $R = 0.3$ with $Ka^{-4} = 4 \times 10^6$, $Ga^{-1} = 1$, and $\eta = 5\delta x$ at (from top left) $t = 0.3, 0.5, 0.7, 0.9, 1.0$.

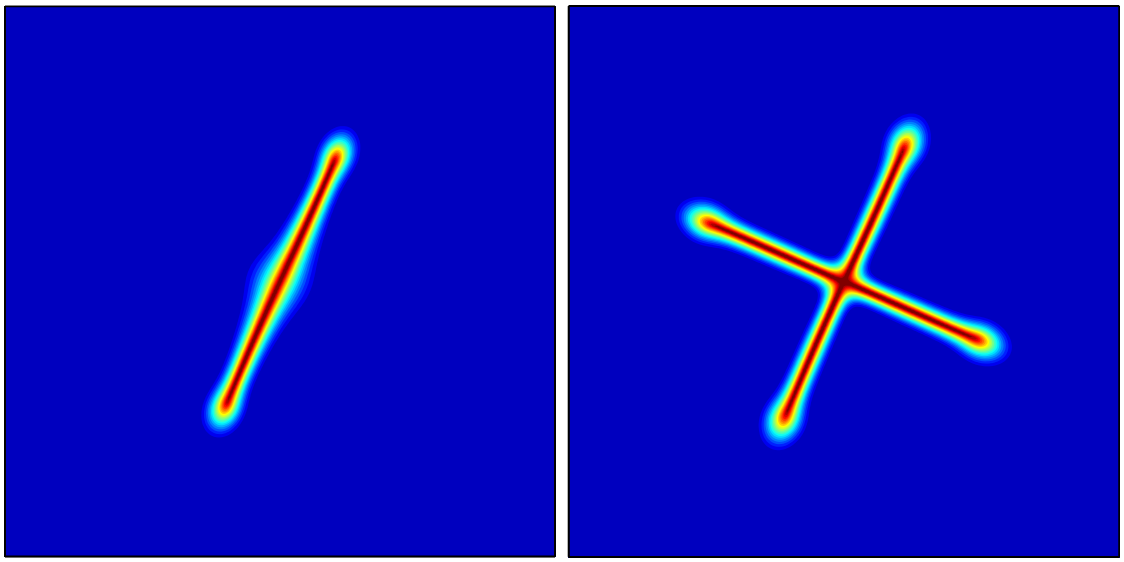

Figure 2.13: Crossing of cracks in fracture of a two-dimensional thin-film with compliant substrate under spherical indenter of radius $R = 0.1$ zoomed to $(-0.1, 0.1)^2$ with $\eta = 5\delta x$ (from left) $Ka^4 = 4 \times 10^6$, $Ga^{-1} = 1$ at $t = 0.23$ (left), $t = 0.24$ (right)

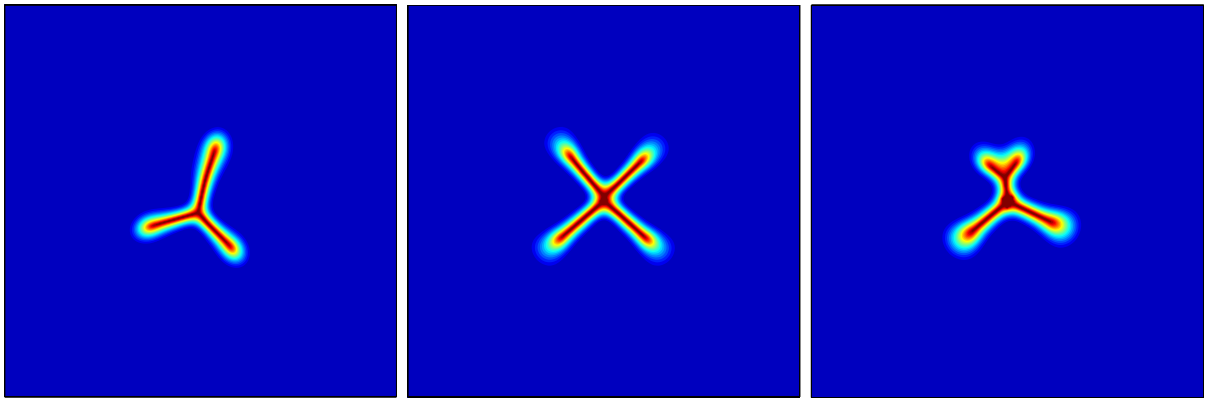

Figure 2.14: Branching of cracks in fracture of a two-dimensional thin-film with compliant substrate under spherical indenter of radius $R = 0.1$ zoomed to $(-0.1, 0.1)^2$ with $\eta = 5\delta x$ (left) $Ka^4 = 6.4 \times 10^7$, $Ga^{-1} = 2.0$ at $t = 0.17$, (center) $Ka^4 = 6.4 \times 10^7$, $Ga^{-1} = 1.5$ at $t = 0.1$, (right) $Ka^4 = 6.4 \times 10^7$, $Ga^{-1} = .7$ at $t = 0.075$.

## 2.6 Conclusions

In this article, we extend the variational approach to fracture mechanics [49, 23, 21, 25] to fracture of elastic thin films with elastic bonds to the substrate. The analysis is based on the bending effects in thin films in contrast to the available literature in this area where the focus is on in-plane effects [110, 70].

The form of the total energy is obtained from three-dimensional linearized elasticity using asymptotic analysis under suitable assumptions in 2.8. We also present an in-depth analysis of a highly idealized problem and verify our approach via numerical experiments. This is not easy since the analytical solution is only available in a few cases. In Section 2.4 we offer a case where it is possible to retrieve the *global minimizer* for quasi-static evolution. The results are compared to both one- and two-dimensional numerical experiments. Comparisons between the numerical results and predictions based on global minimality show that the regularization as offered in Section 2.3.4 converges to those predicted analytically.

We extend the numerical experiments in Section 2.5 to coated cantilever beams and spherical indentation of thin films to show different cases where the formulation can be applied. Two-dimensional loads, such as the ones offered here, lead to an intriguing array of phenomena (e.g. fracture networks, parallel fractures, spiral fracture patterns, fracture-made-cells, etc.). Specifically in Section 2.5.1 the numerical experiments offer an insight on

existence of a second length scale (cracks spacing) different from the Griffith length scale that strongly depends on the non-dimensional cohesive stiffness $Ka^4$.

Although at this point we make no effort in quantitative validation of our model, in Section 2.5.2 we capture a wide range of observed phenomena in fracture of thin films on compliant substrates as well as thin-film fracture in general. These include transition of fracture patterns from circular to radial as well as branching and crossing of cracks.

The main objective of this work is to lay a solid background for the analysis of fracture in thin films. Variational approach to thin-film fracture mechanics shows its potential for prediction of crack nucleation and propagation path. Unlike other methodologies in fracture mechanics by using variational approach to fracture mechanics, no *ad-hoc* treatment is necessary for crack nucleation or crack propagation and bifurcation. Instead, they are naturally predicted through minimization over all crack paths.

## 2.7 A global minimization algorithm based on dynamic programming

Although the closed-form minimization of the total energy functional (2.32) is not feasible, it is possible to produce an algorithm that can be proven to converge to its *global* minimizer. This algorithm is derived from a dynamic programming approach devised in [33] for Mumford-Shah problem. It relies on the following key observation:

Consider a film occupying an interval $\omega = (a, b)$ subject to a load of magnitude $t$, and let $\mathscr{X}_\omega = \{\omega_0, \omega_1, \ldots, \omega_m\}$ be the partition minimizing $E_t^*(\bullet)$ amongst all partitions of $\omega$. Then $\mathscr{X}^- := \{\omega_0, \omega_1, \ldots, \omega_{m-1}\}$ minimizes $E_t^*(\bullet)$ amongst all partitions $\omega \setminus \omega_m$, and

$$E_t^*(\mathscr{X}_\omega) = E_t^*(\mathscr{X}^-) + E_t^*(\{\omega_m\}) + \frac{G}{a}. \tag{2.34}$$

From there, it is easy to deduce that given any interval $\omega = (a, b)$,

$$\min_{\mathscr{X} \text{ partition of } (a,b)} E_t^*(\mathscr{X}) = \min_{x_0 \in \omega} \left( \min_{\mathscr{X}^- \text{ partition of } (a,x_0)} E_t^*(\mathscr{X}^-) + E_t^* \left( \{(x_0, b)\} \right) + \frac{G}{a} \right), \tag{2.35}$$

and that the minimum on the right-hand-side of (2.35) is achieved by $x_0$ and $\mathscr{X}^-$, then the minimum on the left hand side is achieved by $\mathscr{X} := \mathscr{X}^- \cup (x_0, b)$.

Noting finally that the energy is invariant by translation of the domain, *i.e.*, only the length of $\omega$ matters, we arrive at the following algorithm:

**Algorithm 2.1** Dynamic programing approach to the global minimization of (2.22) for a given loading parameter $t$.

assume $\omega = (0, l)$ and let $|\omega| = l$
for a given $n_x$ define $l_i = \frac{i}{n_x - 1} l$
**for** $i = n_x - 1$ to $1$ **do**
    $\mathscr{X}^1_{l-l_i} \longleftarrow \{(0, l - l_i)\}$
    $U^1_{l-l_i} \longleftarrow E^*_t(\mathscr{X}^1_{l-l_i})$
$n_{max} \longleftarrow \frac{a}{G} E^*_t(\{(0, l)\}) + 1$
**for** $n = 2$ to $n_{max}$ **do**
    **for** $i = 1$ to $n_x - 1$ **do**
        Compute $\mathscr{X}^n_{l_i} = \underset{0<j<i}{\arg\min} \left(U^{n-1}_{l_i - l_j} + E^*_t(\mathscr{X}^1_{l_j})\right)$
        $U^n_{l_i} \longleftarrow E^*_t(\mathscr{X}^n_{l_i})$
Compute $\mathscr{X}^* := \underset{1 \le n \le n_{max}}{\arg\min} U^n_l$
$U^* \longleftarrow E^*_t(\mathscr{X}^*)$

Considering quasi-static loading, and for a loading discretization $\{t_i\}$, $0 \le i \le N$, $t_0 = 0$, $t_N = T$, if we assume $\mathscr{X}^{(i)} := \{\omega^{(i)}_0, \ldots, \omega^{(i)}_{m_i}\}$ is the optimal partition for film $\omega = (a, b)$ at loading $t_i$ then admissible partition at loading $t_{i+1}$ consists of the union of optimal partitions of each $\omega^{(i)}_j$, $0 \le j \le m_i$. This, in turn, enforces the irreversibility condition *(IR)* for each loading step.

Using the above observation we adapt this algorithm to account for the quasi-static evolution and the irreversibility constraint. Algorithm 2.2 finds the global minimizer partition $\mathscr{X}^*_{(i)}$ of equation (2.22) for a monotonically increasing load at each step :

### 2.7.1 Numerical results using dynamic programming

Here we present two sets of results obtained using the dynamic programming algorithm 2.2. The first set of results are from a set of parameters where the global minimizer

**Algorithm 2.2** Dynamic programing approach to the global minimization of (2.22) under monotonically increasing load.

1: Initiate $\mathscr{X}^*_{(1)} = \{(0, l)\}$
2: Define $\mathscr{P}(\omega)$ :=set of all partitions of $\omega$
3: **for** $i = 1$ to $N$ **do**
4: assume $\mathscr{X}^*_{(i-1)} = \{\omega_1^{(i-1)}, \ldots, \omega_n^{(i-1)}\}$ and let $n \longleftarrow \#(\mathscr{X}^{(i-1)})$
5: **for** $j = 1$ to $n$ **do**
6: $\mathscr{Y}_j = \underset{\mathscr{Y}_j \in \mathscr{P}(\omega_j^{(i-1)})}{\arg\min} E^*_t(\mathscr{Y}_j)$ (using algorithm 2.1)
7: $\mathscr{X}^*_{(i)} \longleftarrow \bigcup\{\omega \in \mathscr{Y}_j; 1 \leq j \leq n\}$
8: $U^*_{(i)} \longleftarrow E^*_t(\mathscr{X}^*_{(i)})$

of (2.22) similar to that of [70] is attained by fracture by bisection. The second set of results on the other hand highlights the effect of non-convexity of (2.22) resulting in an asymmetrical fracture pattern.

Figure 2.15 shows the evolution of the total energy $E^*_t$ (left) and a schematic representation of the cracks' locations (right) for the 1-D problem as a function of the loading parameter $t$ for a domain of length $l_0 = 0.5$ with $\lambda = 10$, and $Ga^{-1} = 0.05$.

At $t = 0.68$, the configuration corresponding to a single crack at the center of the domain ($x = 0$) becomes energetically favored over the untracked one. This is illustrated by the crossing of the energy curves corresponding, respectively, to the un-cracked configuration and the one with a single centered crack in Figure 2.15 (left). A similar process takes place at $t = 1.62$ when the configuration associated with 3 equi-distributed ($x = -.25, 0, .25$) cracks becomes energetically less costly than the one with a single centered crack. This evolution by successive bisections is similar to the one observed in [70] in the case of constant in-plane strain.

On a longer domain, the non-convexity of the function $F$ leads to a loss of symmetry. Figure 2.16 represents the outcome of a numerical simulation similar to that of 2.15 with $l_0 = 0.8$. In this situation, the first crack nucleation at $t = 0.67$ is off-center at $x = -0.06$. Successive crack nucleations take place at the center of each ligament, but are staggered in time at $t = 0.73, x = 0.22$ and $t = 0.91, x = -0.28$. Note that Figure 2.16 depicts one of

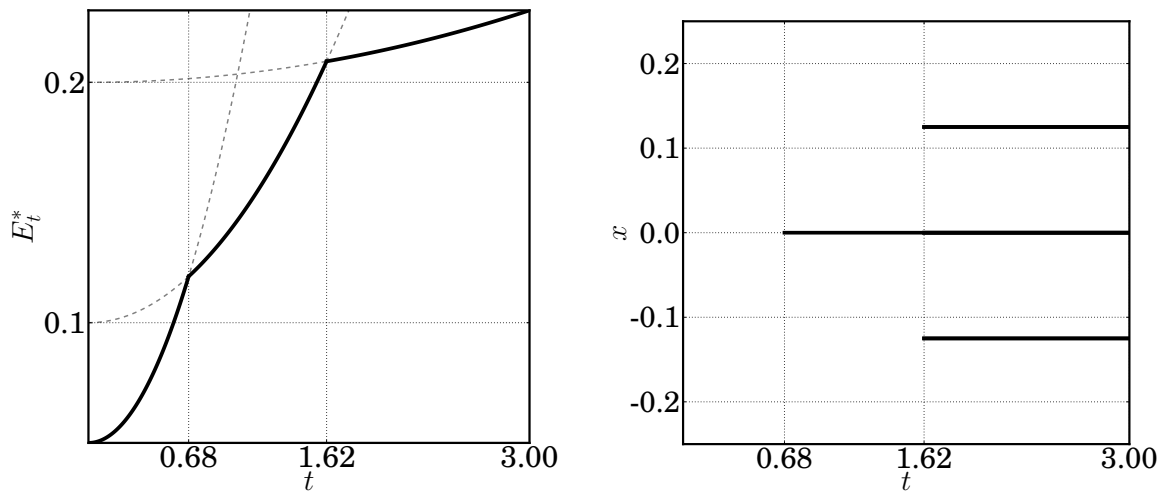


Figure 2.15: Optimal energy (left) and crack location (right) of a sample of length $l_0 = 0.5$ under pure bending obtained using dynamic programming algorithm with $Ga^{-1} = 0.05$, $\lambda = 10$.

the two solutions of this problem, the other being obtained by symmetry with respect to the domain center.

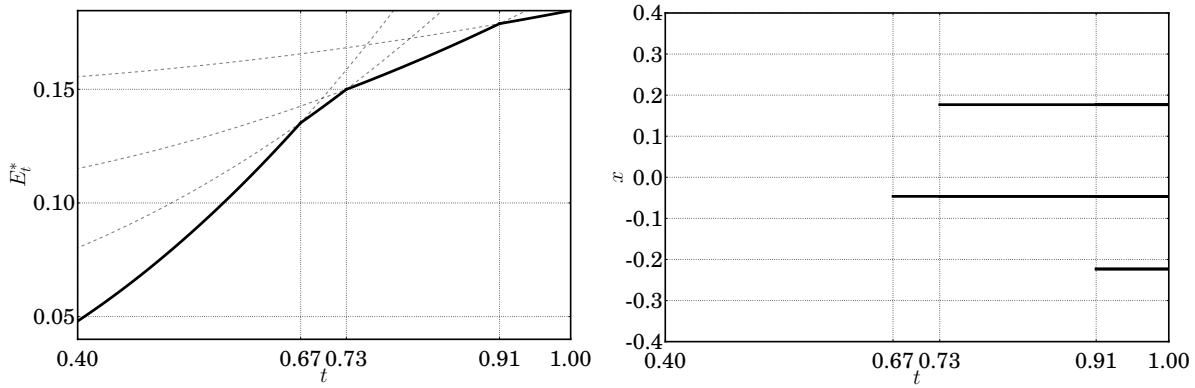


Figure 2.16: Optimal energy (left) and crack location (right) of a sample of length $l_0 = 0.8$ under pure bending obtained using dynamic programming algorithm with $Ga^{-1} = 0.05$, $\lambda = 10$.

The link between non-convexity of the elastic energy functional and loss of symmetry can be easily seen from the graph of $F_\lambda$ (2.31). From (2.32), it is easy to see that finding the optimal configuration consisting of a single crack is equivalent to solving the one-

dimensional minimization problem

$$\min_{0 \le l \le l_0} F_\lambda(l) + F_\lambda(l_0 - l).$$

From the shape of the graph of $F$ in Figure 2.4, one would indeed expect that for small values of $l_0$, $F_\lambda(l) + F_\lambda(l_0 - l)$ admits a unique global minimizer at $l_0/2$ whereas when $l_0$ becomes larger, it becomes a "two-well" function and admits two global minimizers. This is illustrated in Figure 2.17 where $F_\lambda(l) + F_\lambda(l_0 - l)$ is plotted for $\lambda = 10$ and $l_0 = 0.5, 0.8$. The non-convexity for $l_0 = 0.8$ is made more obvious in the rightmost graph by zooming in around the origin.

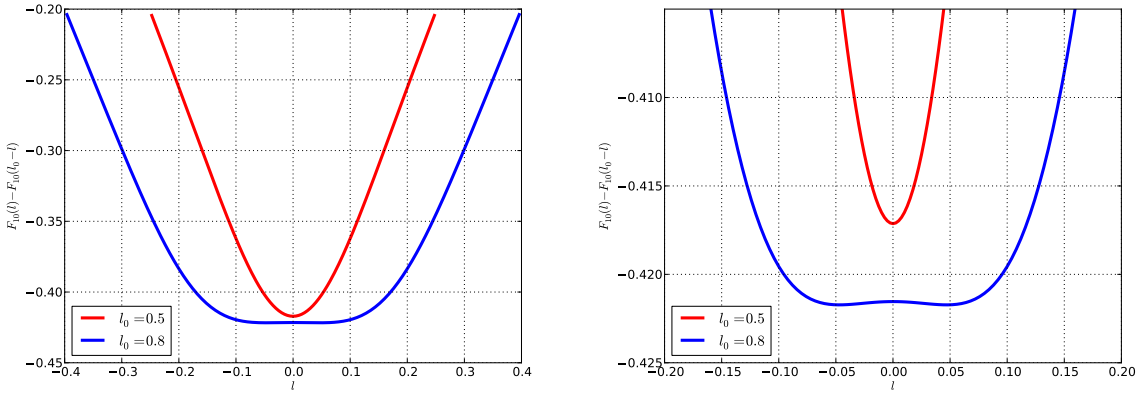


Figure 2.17: Elastic energy of a configuration with a single crack as a position of its location, for a domain length $l_0 = .5$ and $l_0 = .8$. In order to make comparisons easier, the graphs are shifted towards the left by $l_0/2$.

In practical applications, the parameter $\lambda$ is expected to be very large. Figure 2.18 represents a summary of the crack evolution for a more realistic set of parameters: $l_0 = 1$, $\lambda = 31.62$, and $Ga^{-1} = 1$. We chose the scaling factor so that upon a critical load, 9 equi-distributed cracks nucleate together $\gamma = \{\pm 0.4, \pm 0.3, \pm 0.2, \pm 0.1, 0\}$. Again, the qualitative difference between this evolution and the recursive subdivision observed in [70] comes from the non-convexity of the elastic energy with respect to the fragment length.

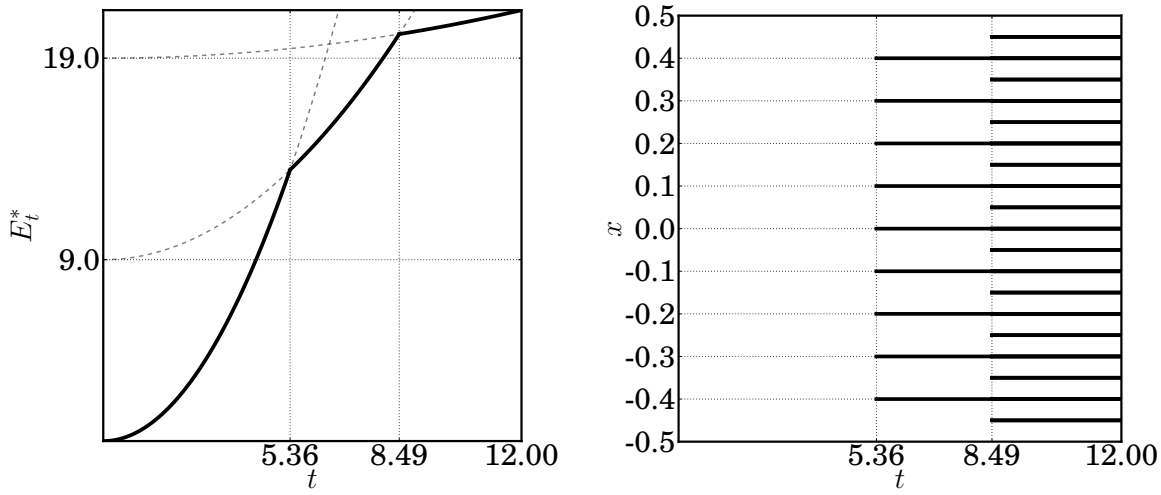


Figure 2.18: Optimal energy (left) and crack location (right) of a sample of length $l_0 = 1$ under pure bending obtained using dynamic programming algorithm with $Ga^{-1} = 1$, $\lambda = 31.62$.

## 2.8 Derivation of the lower dimensional model

We show how the reduced-dimension expression of the elastic energy can be formally derived from the full three dimensional model using a proper rescaling of the layers' thicknesses and elastic properties. We focus on the case of non-homogenous boundary condition *i.e.,* $u^\epsilon = (0, 0, \bar{g}^\epsilon(x_1^\epsilon, x_2^\epsilon))$ at lower boundary of cohesive bond layer. We use the convention that greek letter subscripts stand for indices 1,2 and latin letters for 1,2,3.

We consider a film of thickness $\epsilon$ occupying a region $\Omega_\epsilon := \omega \times (0, \epsilon)$ where $\omega \subset \mathbb{R}^2$ and a transversely anisotropic bonding layer occupying $\Omega_\epsilon^{'} := \omega \times (-\epsilon, 0]$.

The Hooke's law of the film and the bonding layers are given respectively for any kinematically admissible displacement field $u^\epsilon$ by

$$\sigma_{ij}^\epsilon(u^\epsilon) := \lambda_\epsilon e_{kk}^\epsilon(u^\epsilon)\delta_{ij} + 2\mu e_{ij}^\epsilon(u^\epsilon), \tag{2.36}$$

and

$$\begin{cases} \sigma^\epsilon_{\alpha\beta}(u^\epsilon) & := \left[\lambda'_\epsilon e^\epsilon_{\tau\tau}(u^\epsilon) + \lambda^{''}_\epsilon e^\epsilon_{33}(u^\epsilon)\right]\delta_{\alpha\beta} + 2\mu'_\epsilon e^\epsilon_{\alpha\beta}(u^\epsilon) \\ \sigma^\epsilon_{\alpha 3}(u^\epsilon) & := 2\mu^{''}_\epsilon e^\epsilon_{\alpha\beta}(u^\epsilon) \\ \sigma^\epsilon_{33}(u^\epsilon) & := \lambda^{''}_\epsilon e^\epsilon_{kk}(u^\epsilon) + 2\mu^{''} e^\epsilon_{33}(u^\epsilon). \end{cases} \tag{2.37}$$

The total energy associated with $u^\epsilon(x^\epsilon)$ in the film and bonding layer is then given by

$$E_\epsilon(u_\epsilon) = \frac{1}{2}\int_{\Omega_\epsilon \cup \Omega'_\epsilon} \sigma_\epsilon(u^\epsilon) : e_\epsilon(u^\epsilon)\, dx^\epsilon \tag{2.38}$$

Using a change of variables $v^\epsilon = u^\epsilon - (0,0,g^\epsilon)$ where

$$g^\epsilon(x^\epsilon_1, x^\epsilon_2, x^\epsilon_3) = \begin{cases} 0 & \text{if } x^\epsilon \in \Omega_\epsilon \\ -x^\epsilon_3 \bar{g}^\epsilon(x^\epsilon_1, x^\epsilon_2) & \text{if } x^\epsilon \in \Omega'_\epsilon \end{cases} \tag{2.39}$$

is the extension of $\bar{g}^\epsilon$ to $\Omega_\epsilon \cup \Omega'_\epsilon$, we can write (2.38) as:

$$E_\epsilon(v^\epsilon) = \frac{1}{2}\int_{\Omega_\epsilon \cup \Omega'_\epsilon} \sigma_\epsilon(v^\epsilon + g^\epsilon) : e_\epsilon(v^\epsilon + g^\epsilon)\, dx^\epsilon := J_\epsilon(v^\epsilon) + J'_\epsilon(v^\epsilon, \bar{g}^\epsilon), \tag{2.40}$$

Using the expression of the Hooke's laws, (2.40) can be rewritten as

$$\begin{aligned} J_\epsilon(v^\epsilon) :=& \frac{1}{2}\int_{\Omega_\epsilon} \lambda e^\epsilon_{\alpha\alpha}(v^\epsilon) e^\epsilon_{\beta\beta}(v^\epsilon) + 2\mu e^\epsilon_{\alpha\beta}(v^\epsilon) e^\epsilon_{\alpha\beta}(u^\epsilon)\, dx^\epsilon \\ &+ \frac{1}{2}\int_{\Omega_\epsilon} \lambda e^\epsilon_{\alpha\alpha}(v^\epsilon) e^\epsilon_{33}(v^\epsilon) + 4\mu e^\epsilon_{\alpha 3}(v^\epsilon) e^\epsilon_{\alpha 3}(v^\epsilon)\, dx^\epsilon \\ &+ \frac{1}{2}\int_{\Omega_\epsilon} (\lambda + 2\mu) e^\epsilon_{33}(v^\epsilon) e^\epsilon_{33}(u^\epsilon)\, dx^\epsilon, \end{aligned} \tag{2.41}$$

and

$$
\begin{aligned}
J'_\epsilon(v^\epsilon, \bar{g}^\epsilon) :=& \frac{1}{2}\int_{\Omega'_\epsilon} \lambda' e^\epsilon_{\alpha\alpha}(v^\epsilon) e^\epsilon_{\beta\beta}(v^\epsilon) + 2\mu' e^\epsilon_{\alpha\beta}(v^\epsilon) e^\epsilon_{\alpha\beta}(v^\epsilon)\, dx^\epsilon \\
&+ \frac{1}{2}\int_{\Omega'_\epsilon} \lambda'' e^\epsilon_{\alpha\alpha}(v^\epsilon)\left(e^\epsilon_{33}(v^\epsilon) - \bar{g}^\epsilon\right)\, dx^\epsilon \\
&+ \frac{1}{2}\int_{\Omega'_\epsilon} 4\mu''\left(e^\epsilon_{\alpha 3}(v^\epsilon) - \frac{x^\epsilon_3}{2}\bar{g}^\epsilon_{,\alpha}\right)\left(e^\epsilon_{\alpha 3}(v^\epsilon) - \frac{x^\epsilon_3}{2}\bar{g}^\epsilon_{,\alpha}\right)\, dx^\epsilon \\
&+ \frac{1}{2}\int_{\Omega'_\epsilon} (\lambda'' + 2\mu'')\left(e^\epsilon_{33}(v^\epsilon) - \bar{g}^\epsilon\right)\left(e^\epsilon_{33}(v^\epsilon) - \bar{g}^\epsilon\right)\, dx^\epsilon. \qquad (2.42)
\end{aligned}
$$

We then introduce the classical (see [41] for instance) scaling of the coordinate system and deformations

$$
(x_\alpha, x_3) := (x^\epsilon_\alpha, \frac{1}{\epsilon}x^\epsilon_3),\ (v_\alpha, v_3) := (v^\epsilon_\alpha, \epsilon v^\epsilon_3) \qquad (2.43)
$$

leading to the classical transformation of strains

$$
\begin{cases}
e_{\alpha\beta}(v) := e^\epsilon_{\alpha\beta}(v^\epsilon) \\
e_{\alpha 3}(v) := \epsilon e^\epsilon_{\alpha 3}(v^\epsilon) \\
e_{33}(v) := \epsilon^2 e^\epsilon_{33}(v^\epsilon).
\end{cases} \qquad (2.44)
$$

Also to satisfy consistency of the order of magnitudes of $\epsilon$ for displacement field components, we suppose that $\bar{g} = \epsilon^2 \bar{g}^\epsilon$.

The specific form of the linear elastic energy considered in this paper can be derived under the assumption that the in-plane elastic modulii of the bonding layer are small compared to that of the film, and that the out of plane modulii are small compared to the in plane ones. Namely, we assume that

$$
\begin{aligned}
(\lambda_\epsilon, \mu_\epsilon) &:= (\lambda, \mu) \\
(\lambda'_\epsilon, \mu'_\epsilon) &:= \epsilon^2(\lambda', \mu') \\
(\lambda''_\epsilon, \mu''_\epsilon) &:= \epsilon^4(\lambda', \mu'). \qquad (2.45)
\end{aligned}
$$

Furthermore, we assume that the loading is such that $\bar{g} = \epsilon^2 \bar{g}^\epsilon$ so that the total energy is of order $\epsilon$, and define

$$F_\epsilon(v) := \frac{E_\epsilon(v)}{\epsilon} = G_\epsilon(v) + G'_\epsilon(v, \bar{g}), \tag{2.46}$$

with

$$\begin{aligned} G_\epsilon(v) :=& \frac{1}{2} \int_{\Omega_1} \lambda e_{\alpha\alpha}(v) e_{\beta\beta}(v) + 2\mu e_{\alpha\beta}(v) e_{\alpha\beta}(v)\, dx \\ &+ \frac{1}{2\epsilon^2} \int_{\Omega_1} 2\lambda e_{\alpha\alpha}(v) e_{33}(v) + 4\mu e_{\alpha 3}(v) e_{\alpha 3}(v)\, dx + \frac{1}{2\epsilon^4} \int_{\Omega_1} (\lambda + 2\mu) e_{33}(v) e_{33}(v)\, dx, \end{aligned} \tag{2.47}$$

and

$$\begin{aligned} G'_\epsilon(v, \bar{g}) :=& \frac{\epsilon^2}{2} \int_{\Omega'_1} \lambda' e_{\alpha\alpha}(v) e_{\beta\beta}(v) + 2\mu' e_{\alpha\beta}(v) e_{\alpha\beta}(v)\, dx + \frac{\epsilon^2}{2} \int_{\Omega'_1} 2\lambda' e_{\alpha\alpha}(v)(e_{33}(v) - \bar{g})\, dx \\ &+ \frac{\epsilon^2}{2} \int_{\Omega'_1} 4\mu' \left( e_{\alpha 3}(v) - \frac{x_3}{2} \bar{g}_{,\alpha} \right) \left( e_{\alpha 3}(v) - \frac{x_3}{2} \bar{g}_{,\alpha} \right) dx + \\ &\frac{1}{2} \int_{\Omega'_1} (\lambda' + 2\mu') \left( e_{33}(v) - \bar{g} \right) \left( e_{33}(v) - \bar{g} \right) dx. \end{aligned} \tag{2.48}$$

where, for the sake of conciseness, for $\epsilon = 1$ we write $\Omega_1 = \Omega_{\epsilon=1}$, $\Omega'_1 = \Omega'_{\epsilon=1}$ are the rescaled domains.

Consider now a minimizer $v$ of $F_\epsilon$, and the set $\mathbb{V}$ of admissible test functions $\mathbb{V} := \{\phi \in H^1(\Omega_1 \cup \Omega'_1); \phi(x_\alpha, -1) = 0\}$. The first order optimality conditions for $F_\epsilon$ become

$$A_\epsilon(v, \phi; \epsilon) + A'_\epsilon(v, \phi; \epsilon) = 0 \ \forall \phi \in \mathbb{V} \tag{2.49}$$

with

$$\begin{aligned} A_\epsilon(v,\phi) := &\int_{\Omega_1} \lambda e_{\alpha\alpha}(v(\epsilon))e_{\beta\beta}(\phi) + 2\mu e_{\alpha\beta}(v(\epsilon))e_{\alpha\beta}(\phi)\,dx \\ &+ \frac{1}{\epsilon^2}\int_{\Omega_1} \lambda e_{\alpha\alpha}(v(\epsilon))e_{33}(\phi) + \lambda e_{33}(v(\epsilon))e_{\alpha\alpha}(\phi)\,dx \\ &+ \frac{1}{\epsilon^2}\int_{\Omega_1} 4\mu e_{\alpha 3}(v(\epsilon))e_{\alpha 3}(\phi)\,dx \\ &+ \frac{1}{\epsilon^4}\int_{\Omega_1} (\lambda+2\mu) e_{33}(v(\epsilon))e_{33}(\phi)\,dx, \end{aligned} \tag{2.50}$$

and

$$\begin{aligned} A'_\epsilon(v,\phi) :=& \epsilon^2\int_{\Omega'_1} \lambda' e_{\alpha\alpha}(v(\epsilon))e_{\beta\beta}(v) + 2\mu' e_{\alpha\beta}(v(\epsilon))e_{\alpha\beta}(v)\,dx \\ &+ \epsilon^2\int_{\Omega'_1} \lambda' e_{\alpha\alpha}(v(\epsilon))e_{33}(v) + \lambda'(e_{33}(v(\epsilon)) - 2\bar{g})e_{\alpha\alpha}(v)\,dx \\ &+ \epsilon^2\int_{\Omega'_1} 4\mu'(e_{\alpha 3}(v(\epsilon)) - x_3\bar{g}_{,\alpha})e_{\alpha 3}(v)\,dx \\ &+ \int_{\Omega'_1} (\lambda'+2\mu')(e_{33}(v(\epsilon)) - \bar{g})e_{33}(v)\,dx. \end{aligned} \tag{2.51}$$

We now consider and expansion of $v$ in even powers of $\epsilon$ (odd powers of $\epsilon$ would trivially cancel in the sequel)

$$v(\epsilon) = v_0 + \epsilon^2 v_2 + \epsilon^4 v_4 + \mathcal{O}(\epsilon^6), \tag{2.52}$$

where $v_0,\ v_2,\ v_4 \in \mathbb{V}$. Substituting this expression in the first order optimality conditions, we get that

$$\epsilon^{-4}a_{-4}(v,\phi) + \epsilon^{-2}a_{-2}(v,\phi) + a_0(v,\phi) + O(\epsilon^2) = 0\ \forall \phi \in \mathbb{V} \tag{2.53}$$

where

$$a_{-4}(v,\phi) := \int_{\Omega_1} (\lambda + 2\mu) e_{33}(v_0) e_{33}(v)\, dx \tag{2.54}$$

$$\begin{aligned} a_{-2}(v,\phi) := & \int_{\Omega_1} \lambda (e_{\alpha\alpha}(v_0) e_{33}(v) + e_{33}(v_0) e_{\alpha\alpha}(v))\, dx \\ & + \int_{\Omega_1} 4\mu e_{\alpha 3}(v_0) e_{\alpha 3}(v) dx + \int_{\Omega_1} (\lambda + 2\mu) e_{33}(v_2) e_{33}(v)\, dx \end{aligned} \tag{2.55}$$

$$\begin{aligned} a_0(v,\phi) := & \int_{\Omega_1} \lambda e_{\alpha\alpha}(v_0) e_{\beta\beta}(v) + 2\mu e_{\alpha\beta}(v_0) e_{\alpha\beta}(v)\, dx \\ & + \int_{\Omega_1} \lambda (e_{\alpha\alpha}(v_2) e_{33}(v) + e_{33}(v_2) e_{\alpha\alpha}(v))\, dx \\ & + \int_{\Omega_1} 4\mu e_{\alpha 3}(v_2) e_{\alpha 3}(v)\, dx + \int_{\Omega_1} (\lambda + 2\mu) e_{33}(v_4) e_{33}(v)\, dx \\ & + \int_{\Omega_1'} (\lambda' + 2\mu')(e_{33}(v_0) - \bar{g}) e_{33}(v)\, dx \end{aligned} \tag{2.56}$$

Assuming then that convergence takes place at each scale and from the expression of $a_{-4}$, it is easy to obtain that

$$e_{33}(v_0) = 0 \text{ in } \Omega_1, \tag{2.57}$$

so that

$$a_{-4}(v,\phi) = 0 \ \forall v \in \mathbb{V}. \tag{2.58}$$

At order $\epsilon^{-2}$, we first consider a test function $v$ in the form $v(x_\alpha, x_3) = f(x_3) e_3$ with $f$ continuously differentiable on $(0,1)$. From (2.53) and (2.55), we obtain that

$$\int_{\Omega_1} (\lambda e_{\alpha\alpha}(v_0) + (\lambda + 2\mu) e_{33}(v_2)) f'\, dx = 0,$$

and from the arbitrariness of $f$, that

$$e_{33}(v_2) = -\frac{\lambda}{\lambda + 2\mu} e_{\alpha\alpha}(v_0) \text{ in } \Omega_1. \tag{2.59}$$

Combining (2.57), (2.59), and (2.55), we get that $\int_{\Omega_1} 4\mu e_{\alpha 3}(v_0)e_{\alpha 3}(v)\,dx = 0$ for all $v \in V$, so that

$$e_{\alpha 3}(v_0) = 0 \text{ in } \Omega_1, \tag{2.60}$$

so that

$$a_{-2}(v, \phi) = 0 \ \forall v \in \mathbb{V}. \tag{2.61}$$

*Remark* 2.4. Combining (2.57) and (2.60), it is easy to see that $v_0$ is a *Kirchhoff-Love* field in $\Omega_1$, *i.e.,* that there exists a function $U_0$ of $x_\alpha$ such that

$$(v_0)_\alpha = -(x_3 - \frac{1}{2})(v_0)_{3,\alpha}(x_\alpha) + (U_0)_\alpha(x_\alpha),\ \alpha = 1, 2. \tag{2.62}$$

From (2.57), we deduce that $(v_0)_3$ depends only on $x_\alpha$, so that

$$(v_0)_3 = f(x_\alpha)$$

for some function $f$. Accounting then for (2.60), we get that

$$(v_0)_{\alpha,3} = -(v_0)_{3,\alpha} = -\frac{\partial f}{\partial x_\alpha} \text{ in } \Omega_1,\ \alpha = 1, 2,$$

and integrating along the $x_3$ direction we can obtain (2.62)

$$(v_0)_\alpha = -(x_3 - \frac{1}{2})\frac{\partial f}{\partial x_\alpha} + (U_0)_\alpha(x_\alpha) \text{ in } \Omega_1,\ \alpha = 1, 2,$$

where $(U_0)_\alpha$ is the in-plane displacement in $\Omega_1$ on $x_3 = \frac{1}{2}$ plane.

We finally turn our attention to the terms of order 1. Consider first a test function in

the form $\phi = f(x_3)e_3$, with $f \in C_c^\infty(0,1)$. Substituting in (2.56), we get that

$$\int_{\Omega_1} (\lambda e_{\alpha\alpha}(v_2) + (\lambda + 2\mu)e_{33}(v_4))f'(x_3)\,dx = 0,$$

so that

$$e_{33}(v_4) = -\frac{\lambda}{\lambda + 2\mu} e_{\alpha\alpha}(v_2) \text{ in } \Omega_1. \tag{2.63}$$

We then consider a test function in the form $\phi = f(x_\alpha)e_3$ with $f(x_\alpha) \in C_c^\infty(0,1)$. Again, substitution into (2.56) yields

$$\int_{\Omega_1} 2\mu e_{\alpha 3}(v_2)e_{\alpha 3}(\phi)\,dx = 0$$

so that

$$e_{\alpha 3}(v_2) = 0 \text{ in } \Omega_1. \tag{2.64}$$

Finally, we consider a third test function in the form $\phi = f(x_3)e_3$ with $f(x_3) \in C_c^\infty(-1,0)$. Substituting in (2.56), and integrating by parts in the $x_3$ direction, we get that

$$\begin{aligned} 0 &= \int_{\Omega_1'} (\lambda' + 2\mu')(e_{33}(v_0) - \bar{g}(x_\alpha))f'(x_3)\,dx \\ &= [((v_0)_{3,3}(x_\alpha, 0) - \bar{g}(x_\alpha))f(0) - ((v_0)_{3,3}(x_\alpha, -1) - \bar{g}(x_\alpha))f(-1)] \\ &\quad - \int_{\Omega_1'} (\lambda' + 2\mu')(v_0)_{3,33} f(x_3)\,dx. \end{aligned}$$

Since $f(0) = f(-1) = 0$, we obtain

$$\int_{\Omega_1'} (\lambda' + 2\mu')(v_0)_{3,33} f(x_3)\,dx = 0,$$

and therefore

$$(v_0)_{3,33} = 0 \text{ in } \Omega_1'.$$

Using then the continuity of $v_0$ at $x_3 = 0$ (along the interface between film and the cohesive bond), we deduce

$$(v_0)_3 = (1 + x_3)(v_0)_3(x_\alpha, 0^+) \text{ in } \Omega_1'. \tag{2.65}$$

Using (2.58), (2.61) replacing in (2.50) we get:

$$\begin{aligned} A(v,\phi) = &\int_{\Omega_1} \lambda e_{\alpha\alpha}(v_0) e_{\beta\beta}(\phi) + 2\mu e_{\alpha\beta}(v_0) e_{\alpha\beta}(\phi)\, dx \\ &+ \int_{\Omega_1} \lambda (e_{\alpha\alpha}(v_2) e_{33}(\phi) + e_{33}(v_2) e_{\alpha\alpha}(\phi))\, dx \\ &+ \int_{\Omega_1} 4\mu e_{\alpha 3}(v_2) e_{\alpha 3}(\phi)\, dx \\ &+ \int_{\Omega_1} (\lambda + 2\mu) e_{33}(v_4) e_{33}(\phi)\, dx + O(\epsilon^2) \end{aligned} \tag{2.66}$$

using first (2.63) and (2.64) we get:

$$\begin{aligned} A(v,\phi) = &\int_{\Omega_1} \lambda e_{\alpha\alpha}(v_0) e_{\beta\beta}(\phi) + 2\mu e_{\alpha\beta}(v_0) e_{\alpha\beta}(\phi)\, dx \\ &+ \int_{\Omega_1} \lambda e_{33}(v_2) e_{\alpha\alpha}(\phi)\, dx + O(\epsilon^2) \end{aligned} \tag{2.67}$$

finally accounting for (2.59), we get

$$A(v,\phi) = \int_{\Omega_1} \frac{2\mu\lambda}{\lambda + 2\mu} e_{\alpha\alpha}(v_0) e_{\beta\beta}(\phi) + 2\mu e_{\alpha\beta}(v_0) e_{\alpha\beta}(\phi)\, dx + O(\epsilon^2). \tag{2.68}$$

Similarly for (2.51) we get:

$$A'(v,\phi) = \int_{\Omega_1'} (\lambda' + 2\mu')(e_{33}(v_0) - \bar{g}) e_{33}(\phi)\, dx + O(\epsilon^2) \tag{2.69}$$

We can derive the asymptotic energy from (2.68) and (2.69) as:

$$G(u) = \frac{1}{2}\int_{\Omega_1} \frac{2\mu\lambda}{\lambda+2\mu} e_{\alpha\alpha}(v_0)e_{\beta\beta}(v_0) + 2\mu e_{\alpha\beta}(v_0)e_{\alpha\beta}(v_0)\,dx + O(\epsilon^2) \tag{2.70}$$

$$G'(u) = \frac{1}{2}\int_{\Omega_1'} (\lambda'+2\mu')(e_{33}(v_0)-\bar{g})(e_{33}(v_0)-\bar{g})\,dx + O(\epsilon^2). \tag{2.71}$$

Changing variables from $v$ to $u$, integrating in $x_3$, and using (2.62) we get:

$$\begin{aligned} G_\epsilon(u) = &\frac{1}{2}\int_\Gamma \frac{2\mu\lambda}{12(\lambda+2\mu)}(u_0)_{3,\alpha\alpha}(u_0)_{3,\beta\beta} + \frac{\mu}{6}(u_0)_{3,\alpha\beta}(u_0)_{3,\alpha\beta}\,dx \\ &+ \int_\Gamma \frac{2\mu\lambda}{\lambda+2\mu} e_{\alpha\alpha}(U_0)e_{\beta\beta}(U_0) + 2\mu e_{\alpha\beta}(U_0)e_{\alpha\beta}(U_0)\,dx + O(\epsilon^2) \end{aligned} \tag{2.72}$$

where $u_0 = v_0 + g$ is the leading term for in-homogenous scaled displacement field $u = v + g$.

Similarly in $\Omega_1'$ using (2.65) (taking in account that $(v_0)_{3,3} = (u_0)_{3,3} = 0 \,\text{in}\, \Omega_1$), we can write

$$G_\epsilon'(u) = \frac{1}{2}\int_\Gamma (\lambda'+2\mu')|(u_0)_3(x_\alpha) - \bar{g}(x_\alpha)|^2\,dx + O(\epsilon^2), \tag{2.73}$$

where $\Gamma = (\bullet, \frac{1}{2})$ is film's mid surface and $U_0$ is the in-plane displacement in $\Gamma$. In this particular case since out-of-plane ($(u_0)_3$) and in-plane ($U_0$) terms are decoupled and since there is no loading in the in-plane direction (*i.e.*, $g_\alpha = 0$) we get:

$$\begin{aligned} F(u) = &\frac{1}{2}\int_\Gamma \frac{2\mu\lambda}{12(\lambda+2\mu)}(u_0)_{3,\alpha\alpha}(u_0)_{3,\beta\beta} + \frac{\mu}{6}(u_0)_{3,\alpha\beta}(u_0)_{3,\alpha\beta}\,dx \\ &+ \frac{1}{2}\int_\Gamma (\lambda'+2\mu')|(u_0)_3 - \bar{g}|^2\,dx + O(\epsilon^2) \end{aligned} \tag{2.74}$$

□

# CHAPTER 3
# VALIDATION OF FORMULATION IN THE VARIATIONAL APPROACH TO FRACTURE MECHANICS †

## 3.1 Abstract

In this article we report we use numerical algorithm developed based on the variational approach to elastic fracture mechanics. We introduce a new backtracking scheme to control the crack propagation and remedy computational difficulties associated with brutal fracture. We show that using the variational approach based on energy minimization one can conveniently predict crack propagation path for complex loadings and in complex geometries. Comparison of analytical results to a series of well-documented experimental measurements are presented to test the validity of the approach.

## 3.2 Introduction

The modeling of crack geometry (path) has been one of the most challenging and elusive aspects of fracture mechanics and has captured the interest of scientists in different disciplines for many years. The difficulty in this endeavor is two-fold: deriving proper models capable of predicting potentially complex unknown crack paths, and coming up with numerical schemes capable of dealing with the unknown crack geometry without remeshing. The later issue has been tackled with some success by methods based on enriching the approximation space trough cohesive [88, 111] or extended [9, 84] finite elements, or non-local approximations based on phase-fields [64, 81, 80], level sets [3, 17] or eigendeformation [100].

†This chapter has previously appeared as, Mesgarnejad, A., Bourdin, B., Khonsari, M., Validation simulations for the variational approach to fracture., Computer Methods in Applied Mechanics and Engineering. It is used here by permission of Elsevier for details see Appendix B.

Francfort and Marigo's variational approach to fracture [49, 24, 25] aims at addressing both issues simultaneously by providing a rigorous model derived from Griffith's concept of energy restitution between bulk and surface energies, and providing an efficient numerical implementation capable of handling complex unknown crack path. Over the past decade, this approach applied in many areas including elastic fracture [24, 22, 21], thermoelastic fracture [74, 27], thin-film fracture [70, 70, 79], thin-shells [7], electro-mechanical fracture [1, 2], or dynamic fracture [67, 26, 20, 99] to name a few. A major difficulty associated with the variational approach to fracture is the reliance on global energy minimization, which can sometimes result in unrealistic crack paths by making equally admissible "near" and "far" points in configuration space. In this paper, we propose a variant of the backtracking algorithm from [21] that allows a more thorough exploration of "near" states. While most of the literature focuses on verification simulations, or numerical investigations of the properties of such models or algorithms, we focus on the quantitative validation of our method. We use available well-documented experimental data to illustrate the ability of this deep backtracking algorithm, combined with the regularized expression of the variational fracture energy to accurately predict crack paths in realistic situations.

We begin this paper by providing a brief a review of the variational fracture mechanics framework in Section 3.3. In Section 3.4, we review its approximation and minimization processes and introduce the deep backtracking algorithm. In Section 3.5, we compare numerical simulations with experimental results. Finally in Section 3.6, we summarize different aspects of the results obtained in this article.

## 3.3 Methodology

### 3.3.1 The variational approach to elastic fracture

The foundation of the variational approach to fracture mechanics is to associate a potential energy consisting of its stored elastic energy, the work of external forces, and the energy dissipated through fracture to any crack and deformation configuration. For a body

occupying a reference configuration $\Omega \subset \mathbb{R}^n$, $n = 2$ or 3 , subject to a displacement $u$ and containing the set of cracks $\Gamma \subset \Omega$ , we define the potential energy $\mathscr{E}_t(u, \Gamma)$ as:

$$\mathscr{E}_t(u, \Gamma) := \mathscr{P}_t(u, \Gamma) + \mathscr{S}(\Gamma) \tag{3.1}$$

where $\mathscr{P}_t(u, \Gamma)$ is the deformation energy stored in the body and $\mathscr{S}(\Gamma)$ is the energy dissipated through fracture (*i.e.,* the surface energy). The mechanical energy can be written in terms of its local potential $\mathcal{W}(u)$ and the work of the external forces $f_t$ acting on a part $\partial_N\Omega$, of the boundary of the domain

$$\mathscr{P}_t(u, \Gamma) := \frac{1}{2}\int_{\Omega\setminus\Gamma} \mathcal{W}(\boldsymbol{e}(u))\, dx - \int_{\partial_N\Omega} f_t \cdot u\, dx. \tag{3.2}$$

In all that follows, we consider linear elastic materials so that

$$\mathcal{W}(\boldsymbol{e}(u)) := \mathbb{C}\,\boldsymbol{e}(u) : \boldsymbol{e}(u) \tag{3.3}$$

where $\mathbb{C}$ is the fourth order elastic constitutive tensor and $\boldsymbol{e}(u) := (\nabla u + \nabla u^T)/2$ is the linear elastic strain (*i.e.,* the symmetric gradient). For brittle materials, we define the surface energy, $\mathscr{S}(\Gamma)$ as:

$$\mathscr{S}(\Gamma) := G_c\mathcal{H}^{n-1}(\Gamma) \tag{3.4}$$

where $G_c$ is the energy required to create a unit area (unit length) of new cracks, $\mathcal{H}^m$ is the $m$–dimensional Hausdorff measure (*i.e.,* $\mathcal{H}^2(\Gamma)$ is the aggregate area and $\mathcal{H}^1(\Gamma)$ is the aggregate length of cracks $\Gamma$ in three and two dimensions respectively).

### 3.3.2 Non-dimensionalization

To carry out the computations, we introduce a reference displacement $u_0$, a reference length $L_0$, a reference stress $E_0$ and define the non-dimensional displacement $\tilde{u}$, coordinates

$\tilde{x}$, elastic constitutive tensor $\tilde{\mathbb{C}}$, and force $\tilde{f}_t$ as:

$$\begin{aligned}\tilde{u} &:= \frac{u}{u_0}\\ \tilde{x} &:= \frac{x}{L_0}\\ \tilde{\mathbb{C}} &:= \frac{\mathbb{C}}{E_0}\\ \tilde{f}_t &:= \frac{f_t}{E_0},\end{aligned}$$

We then define the $n$-dimensional non-dimensional potential energy

$$\begin{aligned}\tilde{\mathscr{E}}(\tilde{u},\tilde{\Gamma}) &:= \frac{1}{E_0 u_0^2 L_0^{n-2}}\mathscr{E}(u,\Gamma)\\ &= \frac{1}{2}\int_{\tilde{\Omega}\setminus\tilde{\Gamma}} \tilde{\mathbb{C}}\,\tilde{\boldsymbol{e}}(\tilde{u}) : \tilde{\boldsymbol{e}}(\tilde{u})\,d\tilde{x} - \int_{\partial_N\tilde{\Omega}} \frac{L_0}{u_0}\tilde{f}_t\cdot\tilde{u}\,d\tilde{x} + \frac{G_c L}{E_0 u_0^2}\mathcal{H}^{n-1}(\tilde{\Gamma})\end{aligned} \tag{3.5}$$

It is then natural to define a non-dimensional fracture toughness $\tilde{G}$

$$\tilde{G} := \frac{G_c L_0}{E_0 u_0^2} \tag{3.6}$$

so that the non-dimensional total energy (3.5) becomes:

$$\tilde{\mathscr{E}}_t(\tilde{u},\tilde{\Gamma}) = \frac{1}{2}\int_{\tilde{\Omega}\setminus\tilde{\Gamma}} \tilde{\mathbb{C}}\,\tilde{\boldsymbol{e}}(\tilde{u}) : \tilde{\boldsymbol{e}}(\tilde{u})\,d\tilde{x} - \int_{\partial_N\tilde{\Omega}} \tilde{f}_t\cdot\tilde{u}\,d\tilde{x} + \tilde{G}H^{n-1}(\tilde{\Gamma}) \tag{3.7}$$

For ease in notation, from this point on we omit the tilde on all fields, *i.e.,* we write $u$ for $\tilde{u}$ and so on.

### 3.3.3 Quasi-static evolution

In this article we focus on a quasi-static evolution of fracture. For a crack set $\Gamma$, the admissible displacement set consists of functions $\mathcal{K}_t(\Gamma) := \{u \in H^1(\Omega\setminus\Gamma,\mathbb{R}^n)|\ u(x) = \bar{u}_t(x),\ \forall x \in \partial\Omega_D\}$, where $\bar{u}_t(x)$ is a given prescribed boundary displacement on a part $\partial\Omega_D$ of $\partial\Omega$ disjoint from $\partial\Omega_N$. Following [25], the evolution of the displacement field and

associated crack set for a given loading history $f_t$ (and boundary conditions $\bar{u}_t$) is given by the continuous evolution law:

**Definition 3.1. (Quasi-static evolution)** Given a loading sequence $(f_t, \bar{u}_t)$ for $t \in [0, t_{max}]$, a function $t \to (u_t \in \mathcal{K}_t(\Gamma_t), \Gamma_t \subset \bar{\Omega})$ is the solution of the quasi-static evolution if it satisfies:

- **(IR)** Irreversibility of the crack evolution:

$$\Gamma_t \supseteq \Gamma_s, \ \forall\, 0 \leq s \leq t \tag{3.8}$$

- **(GST)** Unilateral global minimality: At any time $t \in [0, t_{max}]$, the state $(u_t, \Gamma_t)$ is such that:

$$\mathscr{E}_t(u_t, \Gamma_t) \leq \mathscr{E}_t(u, \Gamma), \ \forall u \in \mathcal{K}_t(\Gamma_t), \quad \forall\, \Gamma \supseteq \Gamma_t \tag{3.9}$$

- **(EB)** Energy balance: The function $\mathscr{E}(t) := \mathcal{E}_t(u_t, \Gamma_t)$ is absolutely continuous in $t$ and satisfies the condition

$$\frac{d\mathscr{E}}{dt} = \int_{\partial_D \Omega \setminus \Gamma(l(t))} \nabla \mathcal{W}(\boldsymbol{e}(u_t))) \cdot \dot{\bar{u}}_t \, dx - \int_{\Omega_N} f_s \cdot \dot{u}_t \, ds. \tag{3.10}$$

Since evolution in time is only accounted through the irreversibility condition the formulation here is rate-independent; therefore, up to rescaling of time, any monotonically increasing load can be replaced with a linear scaling of a reference load

$$f_t = t f_0. \tag{3.11}$$

where the parameter $t$ is merely a scaling factor. We nevertheless refer to $t$ as "time".

### 3.3.4 Approximation of the energy functional

The implementation of the variational approach to fracture requires the use of sophisticated numerical algorithms. Specifically, the minimization of the displacement field with respect to any kinematically admissible displacement and any set of crack curves introduces a high level of complexity. We follow the approach presented in-depth in [25] and references therein. We introduce a regularization parameter $\epsilon > 0$ homogeneous to a length and a secondary variable $\alpha$ taking its values in $(0, 1)$ to represent the cracks. We define the regularized energy

$$\mathscr{E}_{t,\epsilon}(u, \alpha) := \mathscr{P}_t(u, \alpha) + \mathscr{S}_\epsilon(\alpha), \tag{3.12}$$

where

$$\mathscr{P}_t(u, \alpha) := \frac{1}{2} \int_\Omega (1 - \alpha)^2 \mathbb{C}\boldsymbol{e}(u) : \boldsymbol{e}(u)\, dx + \int_{\Omega_N} f \cdot u\, dx \tag{3.13}$$

and the fracture (surface) energy as:

$$\mathscr{S}_\epsilon(\alpha) := \frac{G_c}{4C_v} \int_\Omega \frac{V(\alpha)}{\epsilon} + \epsilon |\nabla \alpha|^2\, dx, \tag{3.14}$$

where

$$C_v = \int_0^1 \sqrt{V(\alpha)}\, d\alpha \tag{3.15}$$

is a normalization constant (see [28] for instance). The specific choice of the dissipation potential $V(\alpha) = \alpha$ is motivated by the convenience of its numerical implementation and the specific properties of the model at fixed $\epsilon$, namely a stress-softening behavior with an elastic domain [94, 93].

The form of the regularized energy (3.12) is motivated by a now large body of theoretical work establishing it as an approximation, in the sense of $\Gamma$–convergence, of the fracture energy $\mathscr{E}_t$ [4, 5, 35, 36, 48, 53]. Roughly speaking, as $\epsilon \to 0$, the displacement field minimizing (3.12) converges to that of minimizing (3.1), the field $\alpha$ converges to 0 almost everywhere and goes to zero "near the jumps of $u$" (*i.e.,* the cracks).

In our numerical simulations, we consider a time discretization of the quasi-static evolution: We introduce a discrete set of loading parameters $0 = t_0 \leq \cdots \leq t_N = t_{max}$ and for a given choice of the regularization parameter $\epsilon$, we seek minimizers of the regularized energy. At each time step, the irreversibility condition is accounted for through the addition of constraints on the field $\alpha$. Namely, for each $t_i$, we solve the following minimization problem:

$$(u_i, \alpha_i) = \underset{\substack{u_i \in \mathcal{K}_A \\ 0 \leq \alpha_{i-1} \leq \alpha \leq 1}}{\arg\min} \quad \mathscr{E}_{t,\epsilon}(u, \alpha), \tag{3.16}$$

where $\mathcal{K}_A(t_i)$ denotes the set of kinematically admissible displacements and $\epsilon$ is some arbitrarily small parameter.

### 3.4 Numerical implementation

Our minimization strategy for (3.12) is now classical [25]. At each time step, it is achieved by alternating minimizations with respect to $u$ and $\alpha$ until convergence, leveraging the separate convexity of the regularized energy with respect to each field.

In this algorithm, the spatial discretization was done using the Galerkin finite element method. The first step to obtain $u$ is a simple convex problem implemented by solving the associated Euler-Lagrange equation (*i.e.,* an elasticity problem). In the second step to solve for $\alpha$ we use a bounded reduced space Newton minimization scheme for the discrete energy [16]. The variational approach to fracture mechanics requires spatial resolution of discretization to be at most of the order of the characteristic approximation length $\epsilon$. The resulting problems are often very large and necessitate the use of a parallel programming paradigm and the complex numerical tools therein. Our implementation relies on the distributed data structures provided by `libMesh` [66] and for linear algebra on `PETSc` [12, 10].

### 3.4.1 Backtracking schemes

Like many other gradient based minimizations schemes, when dealing with a nonlinear set of equations, the alternate minimization can not be guaranteed to converge to a global minimum of (3.12) but is known to converge to a stationary point of the total energy [31]. The foundation of the backtracking algorithm proposed and discussed in depth in [25] is to derive an additional necessary condition for optimality of a time evolution, and a algorithmic way to ensure that it is satisfied.

Consider a monotonically increasing loading and two loading steps $t_i$ and $t_j$ such that $t_j \leq t_i$. If the pair $(u_i, \alpha_i)$ is admissible for (3.12) at time $t = t_i$, then the pair $(\frac{t_j}{t_i} u_i, \alpha_i)$ is admissible for time $t = t_j$. Therefore, if the pair $(u_j, \alpha_j)$ is the global minimizer at time $t = t_j$, then $\mathscr{E}_{t,\epsilon}(u_j, \alpha_j) \leq \mathscr{E}_{t,\epsilon}(\frac{t_j}{t_i} u_i, \alpha_i)$, so that for any $0 \leq i \leq N$, we have

$$\mathscr{E}_{t,\epsilon}(u_j, \alpha_j) \leq \left(\frac{t_j}{t_i}\right)^2 \mathscr{P}_{t,\epsilon}(u_i, \alpha_i) + \mathscr{S}_\epsilon(\alpha_i), \ \forall\, 0 \leq j \leq i. \tag{3.17}$$

In the Backtracking algorithm, condition (3.17) is checked against all previously computed time steps upon convergence of the alternating minimization algorithm. If a violation is detected *i.e.,* if an admissible pair attaining a lower energy for a past step has been constructed, the time evolution backtracks to that step using the current configuration as an initial guess.

The backtracking search loop (steps 13-17 of Algorithm 3.1) is only performed upon convergence of the alternating minimizations algorithm. The first modification we propose is to perform it after *each* alternate minimization step, in order to better explore the configuration space $(u, \alpha)$.

Of course, checking the backtracking condition for every iteration of the alternate minimization against all the previous time steps may be computationally expensive. Additionally, remark that this loop can be performed for increasing or decreasing values of $k$. This is potentially interesting since different directions can explore different minima of the

**Algorithm 3.1** The backtracking algorithm.

1: Set $\alpha_0 = 0$.
2: Let $\delta_{BT} > 0$, $\delta_{altmin}$ be given tolerance parameters.
3: **for** $n = 0$ to $N$ **do**
4: $\quad \alpha_i^0 \longleftarrow \alpha_{n-1}$
5: $\quad$ **while** $|\alpha^j - \alpha^{j-1}|_{L^\infty} \geq \delta_{altmin}$ **do**
6: $\quad\quad u^{j+1} \longleftarrow \underset{u \in \mathcal{K}_A}{\arg\min}\, E_\epsilon(u, \alpha^j)$
7: $\quad\quad \alpha^{j+1} \longleftarrow \underset{\alpha_i \leq \alpha \leq 1}{\arg\min}\, E_\epsilon(u^{j+1}, \alpha)$
8: $\quad\quad j \longleftarrow j + 1$
9: $\quad u_n \longleftarrow u^j$
10: $\quad \alpha_n \longleftarrow \alpha^j$
11: $\quad \mathscr{P}_n \longleftarrow \mathscr{P}_t(u_n, \alpha_n)$
12: $\quad \mathscr{S}_n \longleftarrow \mathscr{S}_t(u_n, \alpha_n)$
13: $\quad$ **for** $k = 1 \ldots n-1$ **do**
14: $\quad\quad$ **if** $\mathscr{P}_k + \mathscr{S}_k - \left(\frac{t_k}{t_n}\right)^2 \mathscr{P}_n - \mathscr{S}_n \geq \delta_{BT}$ **then**
15: $\quad\quad\quad \alpha^0 \longleftarrow \alpha_n$
16: $\quad\quad\quad n \longleftarrow k$
17: $\quad\quad\quad$ **goto** 5.

configuration space. This leads us to introducing a *deep backtracking* algorithm based on three parameters describing how often and in which order condition (3.17) is checked.

1. The interval $b_i$ controls how often the backtracking search loop is performed;

2. The direction $b_d = \pm 1$ sets which of "older" or "newer" steps are checked first;

3. The scope $b_s$ controls the interval in which the backtracking search loop is performed.

In the next sections, we illustrate the influence of each parameter and how they can be tuned to match well known experimental results.

## 3.5 Numerical experiments

### 3.5.1 The L-shaped plate

The L-shaped experiment depicted in Figure 3.1, reported in [109], offers a simple mixed tension-compression configuration. These experimental data have been previously used for benchmarking and validation of numerical techniques in [77, 106, 62, 17]. The

**Algorithm 3.2** The deep backtracking algorithm.

Set $\alpha_0 = 1$.
Let $\delta_{BT} > 0$, $\delta_{altmin}$ be given tolerance parameters.
**for** $n = 0$ to $N$ **do**
    **if** $n > b_s$ **then**
        $b_s \longleftarrow n$
    $\alpha_i^0 \longleftarrow \alpha_{n-1}$
    **while** $|\alpha^j - \alpha^{j-1}|_{L^\infty} > \delta_{altmin}$ **do**
        $u^{j+1} \longleftarrow \underset{u \in \mathcal{K}_A}{\arg\min}\, E_\epsilon(u, \alpha^j)$
        $\alpha^{j+1} \longleftarrow \underset{\alpha_i \leq \alpha \leq 1}{\arg\min}\, E_\epsilon(u^{j+1}, \alpha)$
        **if** $j \bmod b_i = 0$ **then**
            $\mathscr{P}_n^j \longleftarrow \mathscr{P}_t(u^j, \alpha^j)$
            $\mathscr{S}_n^j \longleftarrow \mathscr{S}_t(u^j, \alpha^j)$
            **if** $b_d = 1$ **then**
                $k_0 = \max((b_s - \text{scope}), 1)$
                $k_1 = n - 1$
            **else**
                $k_0 = n - 1$
                $k_1 = \max((b_s - \text{scope}), 1)$
            **for** $k = k_0$ to $k_1$ **do**
                **if** $\mathscr{P}_k + \mathscr{S}_k - \left(\frac{t_k}{t_n}\right)^2 \mathscr{P}_n^j - \mathscr{S}_n^j \geq \delta$ **then**
                    $\alpha^0 \longleftarrow \alpha^j$
                    $n \longleftarrow k$
                    **goto** 7.
        $j \longleftarrow j + 1$
    $u_n \longleftarrow u^{j+1}$
    $\alpha_n \longleftarrow \alpha^{j+1}$

experiments are done using a concrete L-shape panel 10 cm in width fixed to a mortar foundation at the bottom and loaded by a hydraulic system connected to a mortar jacket on its right side. The material properties taken from the aforementioned references are listed in Table 3.1.

Table 3.1: Material properties for L-shape plate [109].

| E [GPa] | $\nu$ | $G_c$ [Nm$^{-1}$] |
|---|---|---|
| 25.85 | 0.18 | 95 |

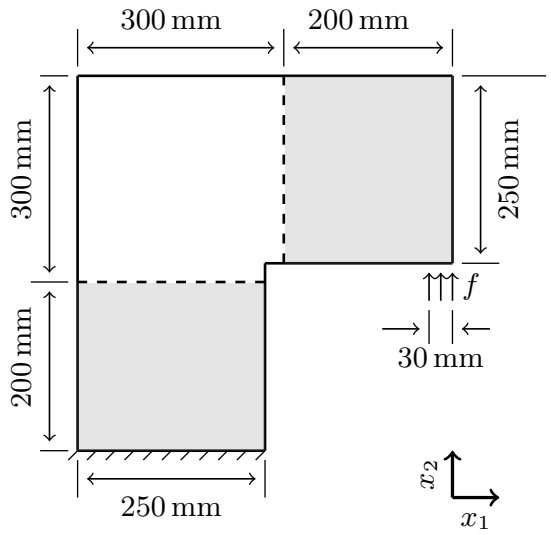


Figure 3.1: L-bar experiment schematics [109], $\alpha \equiv 0$ in gray areas (all sizes are in mm).

For this problem, we performed series of computations using backtracking or deep backtracking, and varying the interval, scope, and direction for two different mesh sizes. The sample geometry and geometry are depicted in Figure 3.1. In order to avoid changes in "effective toughness" induced by the relative magnitude of the mesh size $h$ and regularization parameter $\epsilon$ as discussed in [25], we kept their ratio fixed $h/\epsilon = 5$. In order to speed up computations, we also used a coarser mesh and forced $\alpha = 0$ in the areas represented in gray in the schematics, while setting $\alpha = 0$ along the corner where crack nucleation was expected. In all cases, we observed an elastic phase, followed by the sudden nucleation of a short crack originating from the corner of the domain and subsequently propagation in a stable manner. Figure 3.2 highlights the influence of the backtracking algorithm on the initial crack, and Figure 3.3 compares crack path at a later loading stage with experimental observation from [109]. As expected, there is very little difference in the initial crack length between computations without backtracking or with a standard backtracking, but the standard backtracking leads to lower critical load at nucleation (see Table 3.2). Deep backtracking with a forward direction, an interval $b_i = 1$ and a scope $b_s = \infty$ leads to a shorter crack, and an even lower critical load, which is consistent with the fact that this algorithm is more exploratory than the original one. Neither the nucleation length or load

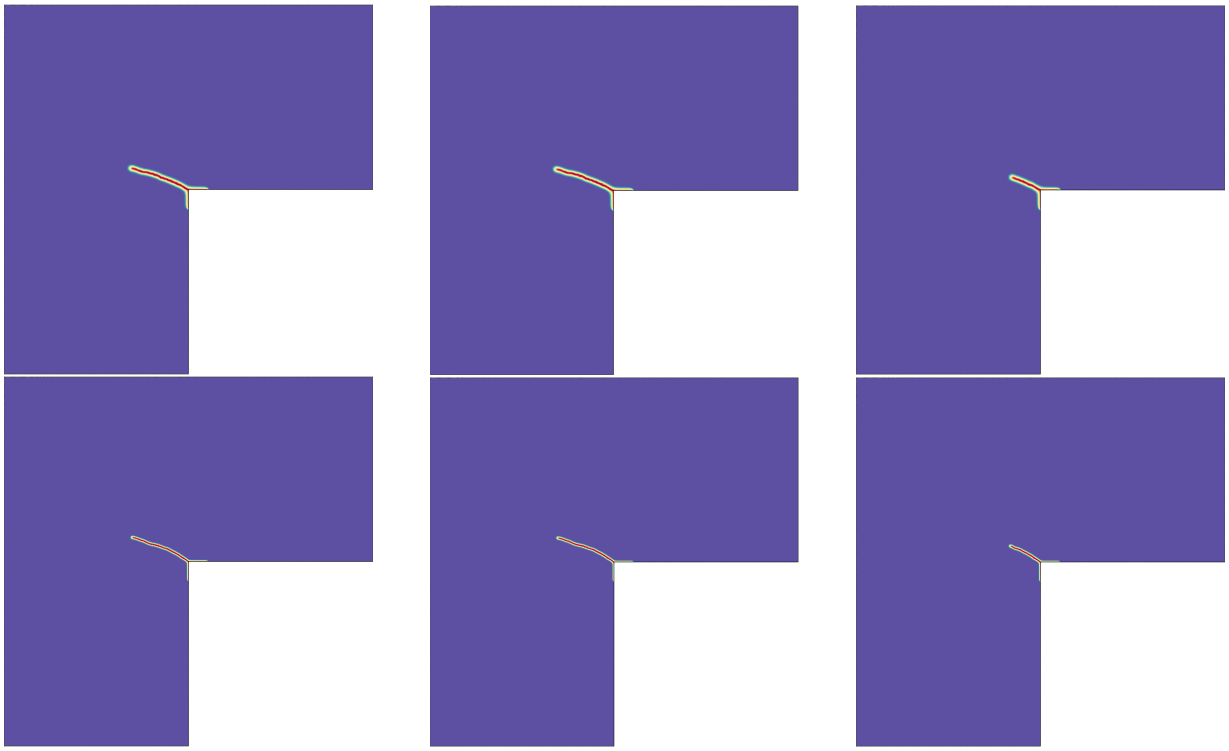

Figure 3.2: Pseudo-color plot of the regularized crack field $\alpha$ after nucleation of a crack for the L-shaped plate without backtracking (left), with the original backtracking (center) or the proposed deep backtracking (right). The material properties are that of Table 3.1. The mesh size and regularization length are $h = 0.625\,\text{mm},\ \epsilon = 3.125\,\text{mm}$ (top row) and $h = 0.3125\,\text{mm},\ \epsilon = 1.5625\,\text{mm}$.

seem to be sensitive to the choice of direction, interval, or scope for this problem. We also did not observe any significant difference in the final crack path when using either variant of the backtracking algorithm (see Figure 3.3). On the other hand, we observed that the critical load and path for each algorithm shows some sensitivity to the regularization parameter (see the variation of initial length and crack angle in Table 3.2). This is again consistent with the finding of [94] who suggest that the link between a material's yield stress and regularization length at the onset of loss of stability of the elastic solution in uniaxial tension experiment can be used to calibrate the regularization parameter. Yet, we did not attempt to do this calibration. In all cases, the crack angle between the initial crack and the horizontal axis in our computations is within the rather large bracket of experimental measurements of $0° - 43°$.

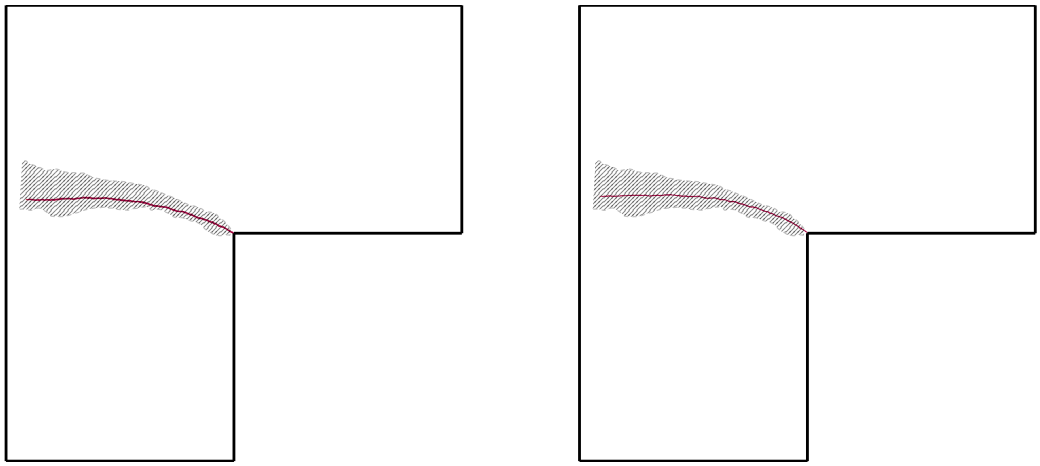

Figure 3.3: Crack path in the L-shaped plate: comparison of the numerical simulations results with with the experimental data (in gray) [109] crack path ($0.9 \leq \alpha \leq 1$ in red) for the characteristic approximation length (left) $\epsilon = 3.125\,\text{mm}$ (right) $\epsilon = 1.5625\,\text{mm}$.

Note finally that in all cases, the force-displacement diagram Figure 3.4 is consistent with experiments with the significant caveat that the stress hardening observed in experiments prior to failure cannot be accounted for in a linear elastic-brittle material.

Table 3.2: L-shaped plate numerical simulation results for different backtracking algorithms.

| $\epsilon$ [mm] | Backtracking algorithm | Critical vertical displacement [mm] | Critical load [kN] | Initial crack length [mm] | Initial crack angle |
|---|---|---|---|---|---|
| 3.125 | None | 0.2496 | 7.3394 | 87.95 | 26.06° |
| 3.125 | Original | 0.2352 | 6.9533 | 87.95 | 26.06° |
| 3.125 | Deep | 0.2304 | 6.8161 | 43.39 | 26.06° |
| 1.5625 | None | 0.2624 | 7.8327 | 96.26 | 33.21° |
| 1.5625 | Original | 0.2448 | 7.3241 | 96.26 | 33.21° |
| 1.5625 | Deep | 0.2416 | 7.2296 | 52.81 | 33.21° |

One of the features of the variational approach to fracture is the effortless generalization to the three dimensions. Figure 3.5 shows a 3-D (isovolume) rendering of smeared fracture field $0.9 \leq \alpha \leq 1$ which was done using approximately 187,000 linear tetrahedral elements with average edge size $h_f = 2.5\,\text{mm}$ in the brittle computational domain (look at Figure 3.1) and regularization length $\epsilon = 5\,\text{mm}$. Again, the crack path falls with the

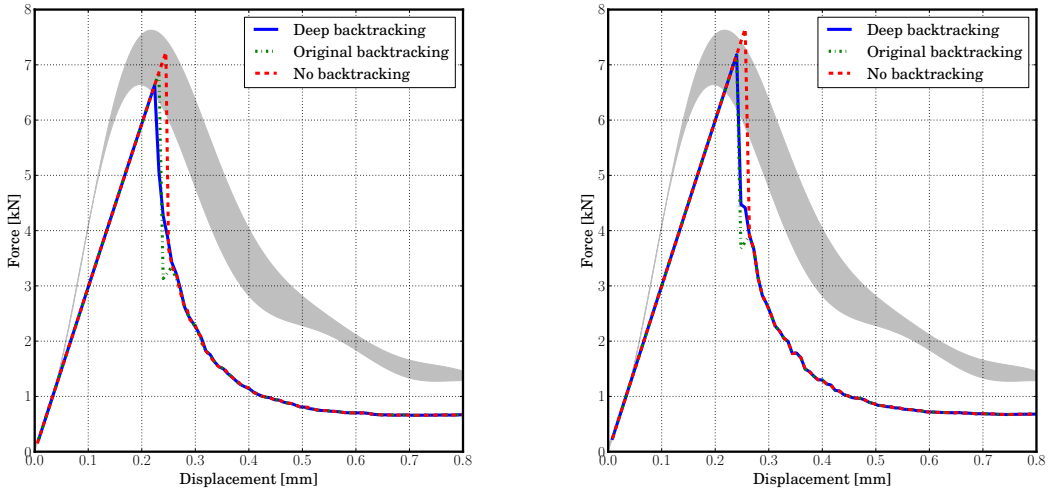


Figure 3.4: Applied force as a function of the vertical displacement at the lower left corner of the plate: comparison of the numerical simulations results with with the experimental data (in gray) [109] crack path ($0.9 \leq \alpha \leq 1$ in red) for the characteristic approximation length (left) $\epsilon = 3.125\,\text{mm}$ (right) $\epsilon = 1.5625\,\text{mm}$.

envelope of experimentally observed paths, demonstrating the ability of our approach to correctly identify crack path on three dimensions.

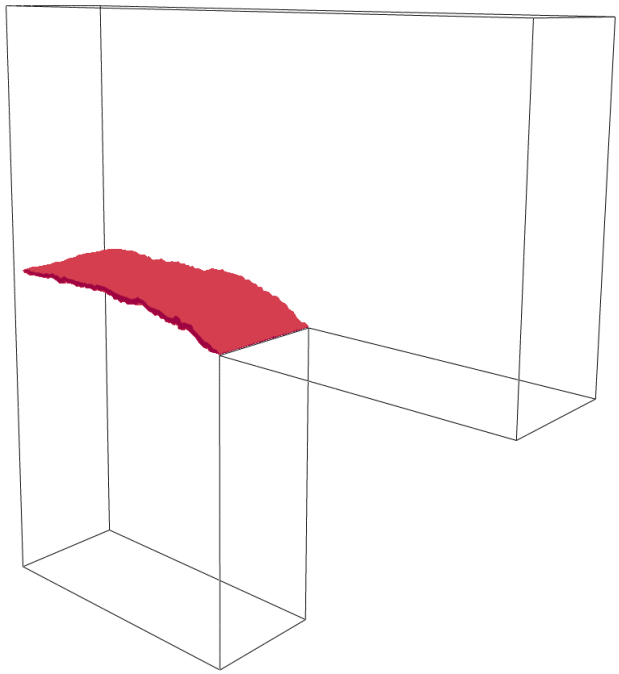

Figure 3.5: Crack path in a three-dimensional L-shaped numerical simulation

### 3.5.2 A three-point bending experiments

In order to highlight the difference between standard and deep backtracking, we turn our attention an asymmetrically notched three-point bending experiment on Plexiglas sheets originally described in [60]. The experiment was designed so that small variations of the sample geometry and loading would lead to large changes in crack path, and is therefore a good test when estimating a method's ability to identify crack path [107, 82, 18, 52]. The sample geometry and its loading are shown in Figure 3.6, the material properties in Table 3.3, and the location and length of the initial crack in two different configurations in specific values of the location of the top, middle and bottom holes (indicated respectively by T,M and B) in Table 3.4. In order to reduce the computational cost and eliminate the

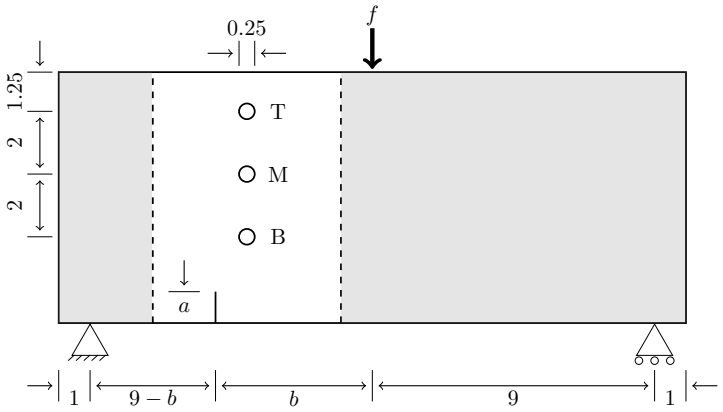


Figure 3.6: Three-point bending experiment schematics, $\alpha \equiv 0$ in gray areas (all the sizes are in inches).

Table 3.3: Material properties for asymmetric three-point bending.

| E (Kpsi) | $\nu$ | $G_c$ (lb in$^{-1}$) |
|---|---|---|
| 450 | 0.35 | 1.73 |

Table 3.4: Material properties for asymmetric three-point bending.

| configuration | **I** | **II** |
|---|---|---|
| $a$ (in) | 1 | 2.5 |
| $b$ (in) | 6 | 6 |

need to deal with potential compressive cracks around the support and force application points, we used a coarse mesh and forced $\alpha = 0$ in the area shown in grey in Figure 3.6. The central part of the domain was meshed with linear triangular finite element with an average edge length of average 0.01 inch, for a total of approximately 1.35 million elements.

Figure 3.7 shows a comparison between the computed crack path for configuration I (see Table 3.4) and experimental results. Without backtracking, we observe that after a long elastic phase, a long crack suddenly forms, spanning from the initial notch to the middle hole, then the upper hole, then continuing through the domain itself (see Figure 3.7-left). The computed crack path only matches experimental data until it reaches the vicinity of the middle hole, and significantly deviates afterwards. As described in [21, 25], in such situation there is no expectation that energy balance (3.17) should be satisfied, and indeed, it is not. Using the original backtracking algorithm leads to an evolution following the same path (recall that the backtracking search loop is only performed after the alternate minimizations algorithm has converged, *i.e.,* once the crack path from Figure 3.7-left has been identified), but a crack growing at a significantly lower loading, so that total energy balance is satisfied. Using the deep backtracking, still leads to sudden crack propagation (see Figure 3.8), but along a path that is closer to that observed in experiments, and does not restart from the middle hole. The crack path is shown for a computation with $b_i = 5$, $b_s = \infty$ and $b_d = +1$ is shown in Figure 3.7-right. We performed multiple experiments varying the value of the three backtracking parameters and obtained similar results, as long as the interval is not set "too high" (indeed, $b_i = \infty$ would correspond to the original backtracking). Additionally, we observed that the deep backtracking leads to a solution energetically favorable compared to the original one (see Figure 3.9). This is expected as the deep backtracking algorithm explores a larger portion of the configuration space. Of course, we do not claim that the computed solution is a global energy minimizer.

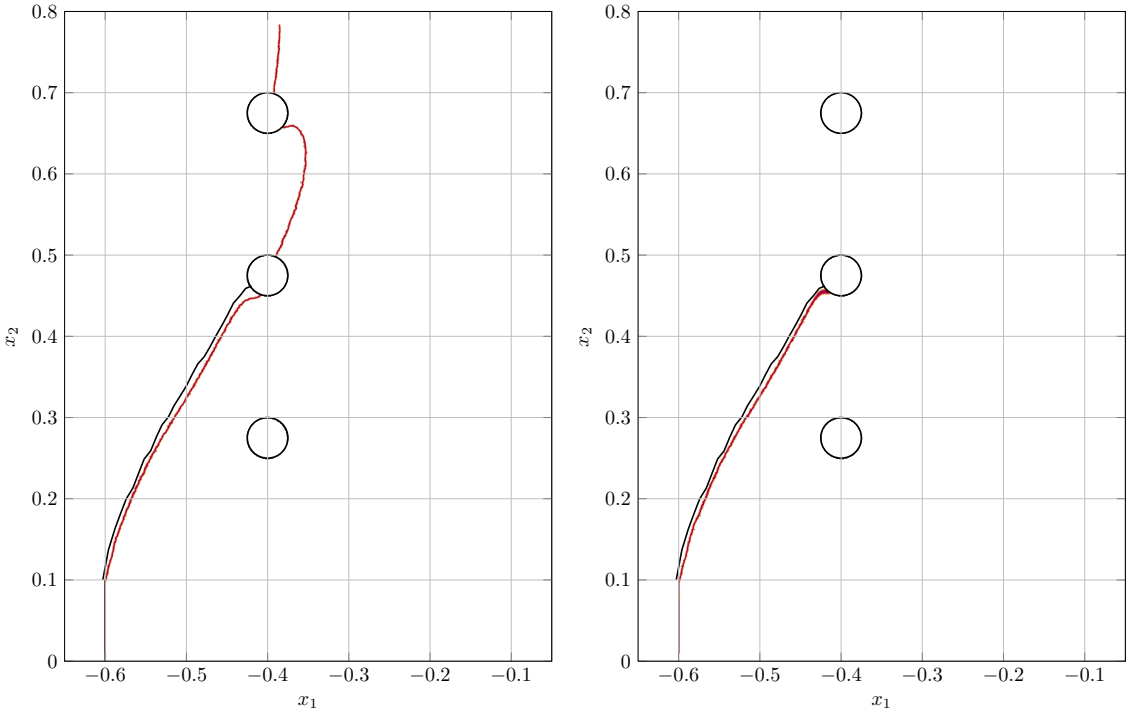


Figure 3.7: Asymmetric three-point bending experiment configuration **I** ($a = 6\,\text{in},\ b = 1\,\text{in}\ \epsilon = 0.02\,\text{in}$): comparison of crack path ($0.9 \leq \alpha \leq 1$ in red) with experimental data [109] (left) original backtracking (right) deep backtracking.

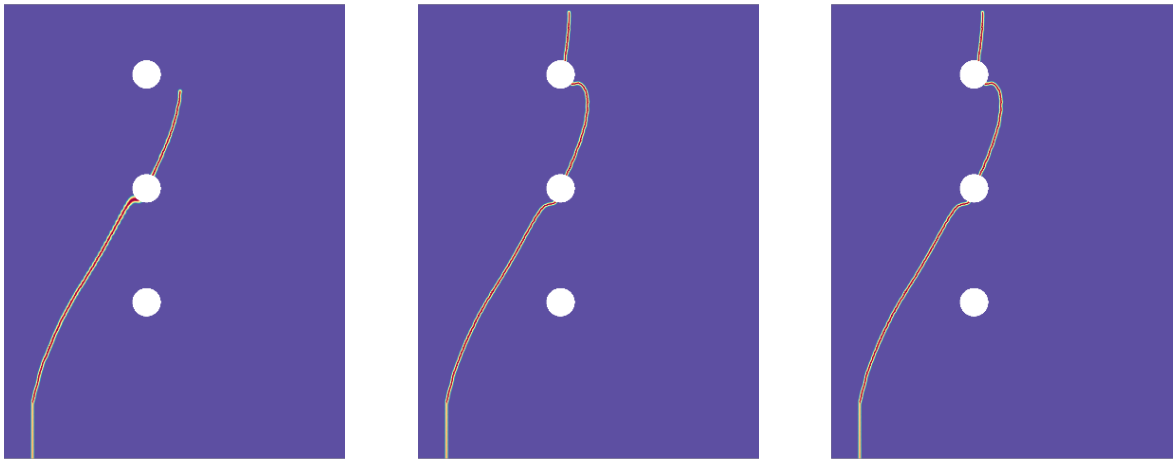

Figure 3.8: Asymmetric three-point bending experiment smeared fracture field $\alpha$ at nucleation for configuration **I** ($a = 6\,\text{in},\ b = 1\,\text{in}$) using (left) deep backtracking (middle) original backtracking (right) no backtracking.

A second set of numerical simulations for configuration **II** (see Figures 3.10-3.11) highlights a similar behavior of the deep compared to standard backtracking. Both the solution without and with standard backtracking lead to a sudden crack propagation through the

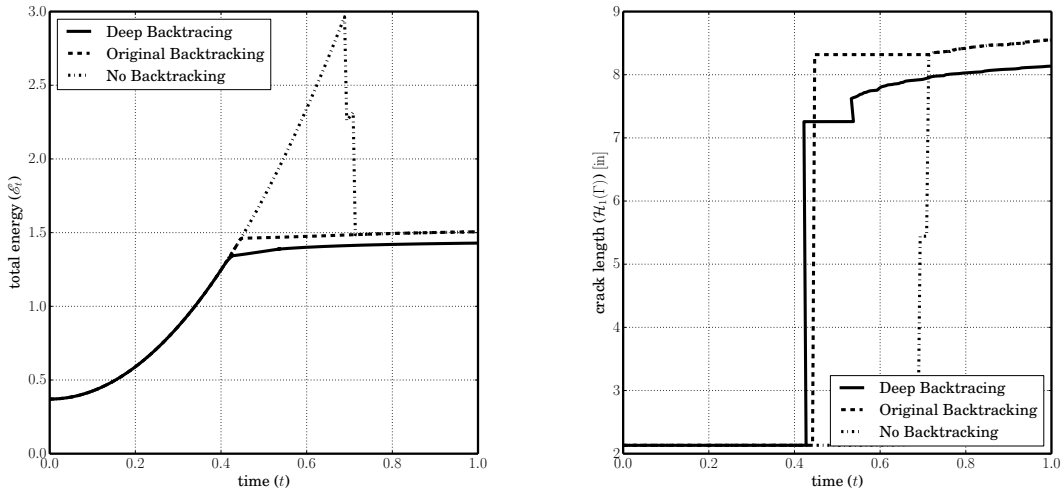


Figure 3.9: Asymmetric three-point bending experiment configuration **II** ($a = 6\,\text{in},\ b = 2.5\,\text{in}$): comparison of total energy (left) and crack length (right) using different backtracking algorithms.

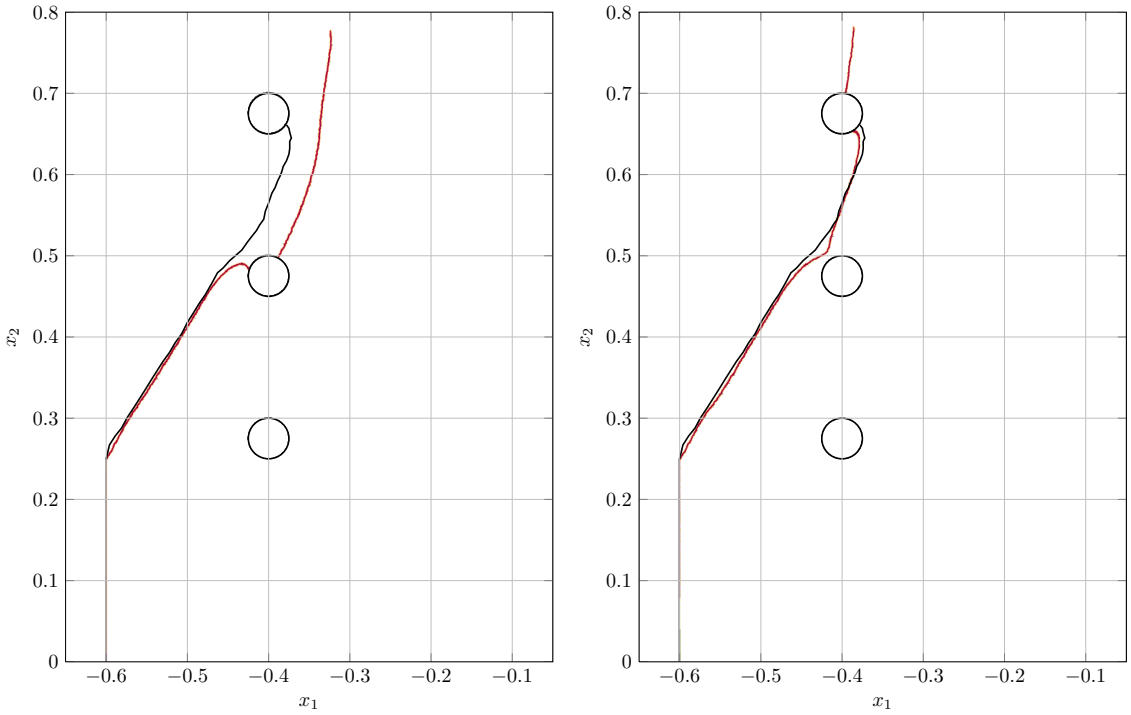


Figure 3.10: Asymmetric three-point bending experiment configuration **II** ($a = 6\,\text{in},\ b = 2.5\,\text{in}\ \epsilon = 0.02\,\text{in}$): comparison of crack path ($0.9 \leq \alpha \leq 1$ in red) with experimental data [109] (left) original backtracking (right) deep backtracking.

middle hole, ending in the bulk of the domain whereas the deep backtracking consistently leads to a crack reaching the top hole, as in the experiments, despite being deflected by

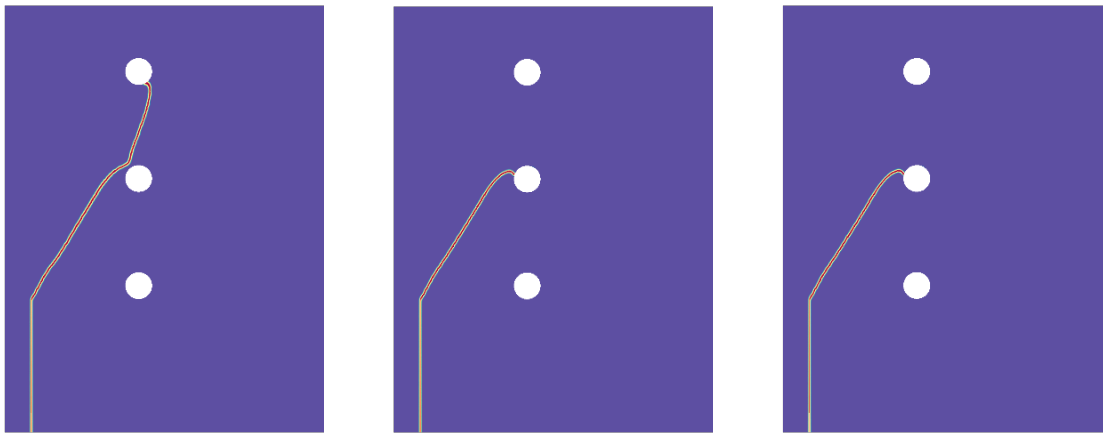

Figure 3.11: Asymmetric three-point bending experiment smeared fracture field $\alpha$ at nucleation for configuration **II** ($a = 6\,\text{in},\ b = 2.5\,\text{in}$) using (left) deep backtracking (middle) original backtracking (right) no backtracking.

the presence of the middle hole (see Figure 3.10). Again, deep backtracking leads to a energetically favorable solution over standard backtracking. We note a significant difference between the numerical and experimental solution as our numerical simulation consistently lead to a crack reactivating out of the top hole, at its onset. Again, no significant difference in the primary crack path (from the notch to the first intersection with one of the holes) was observed when the numerical simulations performed were done using different combination of the auxiliary deep backtracking parameters (*i.e.,* direction, scope, interval).

### 3.5.3 The Nooru-Mohamed tension shear experiments

In the Nooru-Mohamed tension shear experiment, the double-edge-notched specimen is subject to mixed tensile and shear loads [87]. The result of this experiments has been used for validation purposes in number of articles [51, 46, 95, 90]. Figure 3.12 shows the schematic of the test specimen and Table 3.5 summarizes the material properties used in the numerical simulations. Here the loading protocol 4b, as defined in [87] was investigated numerically. This protocol specifies the loading path as follows: (i) apply constant shear load $f_s$ while keeping $f_n \equiv 0$, (ii) apply monotonically increasing $f_n$ while keeping $f_s$ constant. In the experiments, proper care was taken to ensure that the direction of the two loads always remained perpendicular; to achieve the same results in the simulation,

the elastic step of alternate minimization was obtained by superposition of three loadings as depicted in Figure 3.13.

Both backtracking algorithms can be extended to account for this loading by subtracting the work of constant loads from the bulk elastic energy so that the backtracking condition (line 14 in Algorithm 3.1 or line 20 in Algorithm 3.2) becomes

$$\mathscr{P}_k + \mathscr{S}_k + \mathscr{B}_k - \left(\frac{t_k}{t_n}\right)^2 \mathscr{P}_n^j - \mathscr{S}_n^j - \mathscr{B}_n^j \geq \delta, \tag{3.18}$$

where $\mathscr{B}$ is the bulk energy due to constant loads (fiest and second loading stages in Figure 3.13).

The loading protocol highlighted above results in the rotation of principal stresses as the crack propagates which, in turn, results in two curvilinear crack paths. The computations in this section were done using approximately 337,000 linear triangular elements with an average 0.5 mm side length (see Figure 3.6).

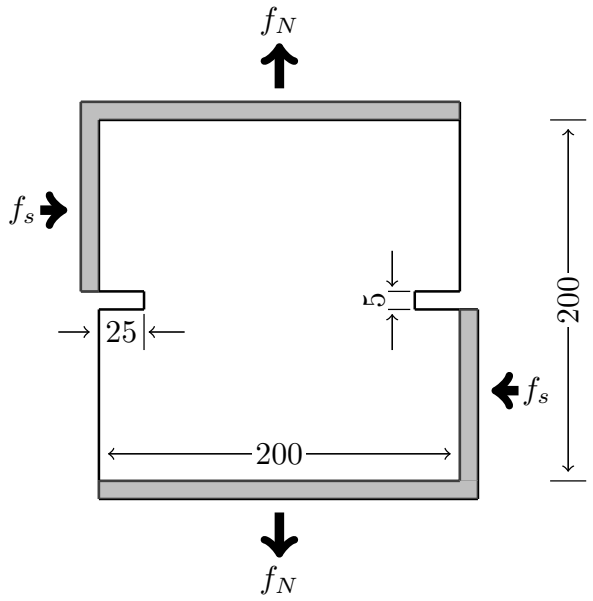


Figure 3.12: Tension shear experiment schematics (all the sizes are in mm, gray areas are rigid).

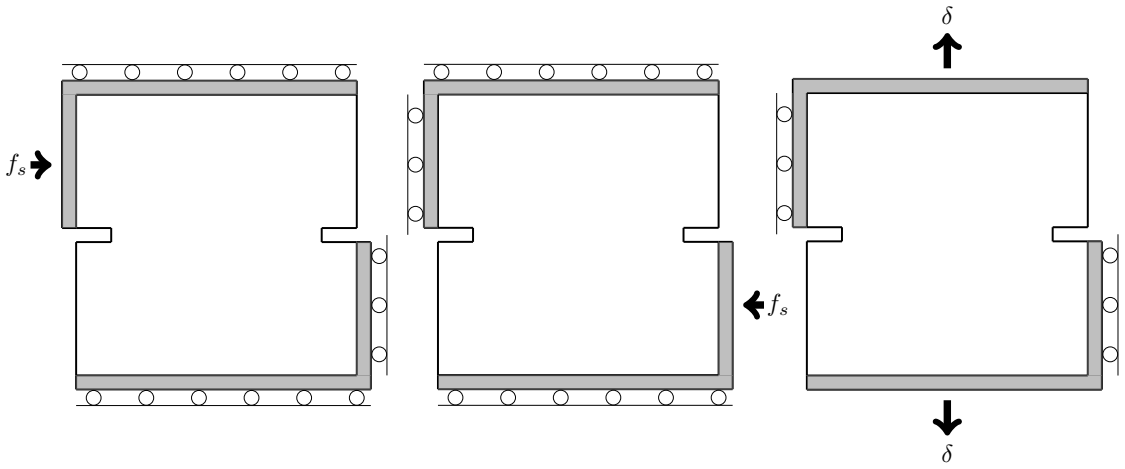


Figure 3.13: Elastic substeps for the tension shear numerical simulations.

Table 3.5: Material properties for tension shear experiment.

| E (GPa) | $\nu$ | $G_c$ ($\mathrm{Nm}^{-1}$) |
|---|---|---|
| 30 | 0.2 | 110 |

In this computation, we observed an elastic phase followed by the nucleation of two cracks of non-zero length, which then propagate progressively. The type of backtracking algorithm did not change the qualitative behavior or the overall path, but again altered the critical load upon which the crack propagated, with as expected an earliest onset for the standard backtracking then deep backtracking.

Figure 3.14 shows a comparison between the numerical results and the experimental data for $f_s = 10\,\mathrm{kN}$ along with simulations based on XFEM and an elasto-plastic model [19]. In the variational approach, crack evolution is governed by a *global* principle (energy minimization) instead of a *local one* (criticality of the elastic energy release rate at each crack tip). Owing to the lack of uniqueness of solution, it may happen that symmetric sets of asymmetric solutions be energy minimizers. Here, we observed that the overall path nearly symmetric and that both cracks are nucleated simultaneously. However, there was a small difference in crack length at nucleation and throughout the evolution (see Figure 3.14-(right)). It is not clear if this behavior illustrates the possible non-uniqueness

often solution of the problem, or is a spurious effect induced by the lack of symmetry of the mesh or numerical error (see also Figure 3.15).

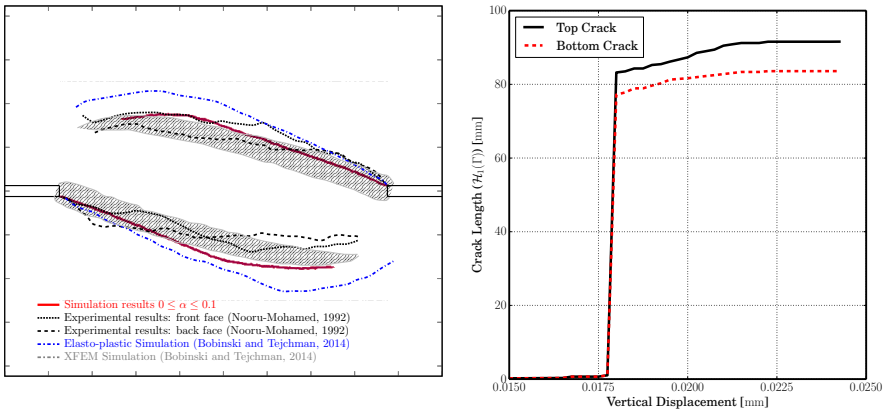


Figure 3.14: Nooru-Mohamed experiment: (left) comparison of simulated crack path ($0.9 \leq \alpha \leq 1$ in red) with experimental data [87] front face (dotted black line), back face (dashed black line), elasto-plastic simulation (gray hashed area) [19], and XFEM simulation (blue dash-dotted line) [19]. (right) Crack length as a function of the vertical displacement top crack in black and bottom crack in red.

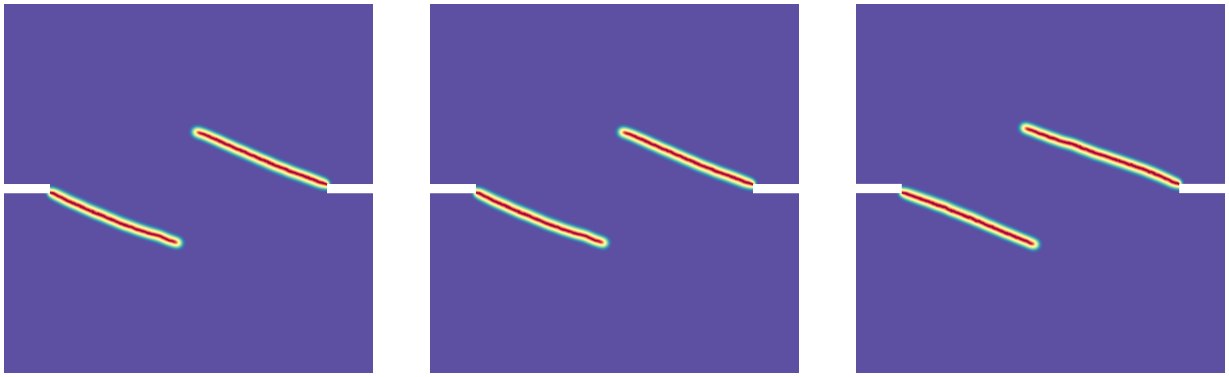

Figure 3.15: Pseudo-color plot of the regularized crack field $\alpha$ after nucleation of a crack for the L-shaped plate without backtracking (left), with the original backtracking (center) or the proposed deep backtracking (right). The material properties are that of Table 3.5. The mesh size and regularization length are $h = 0.5\,\text{mm},\ \epsilon = 2.5\,\text{mm}$.

### 3.5.4 The Brokenshire torsion experiments

We finally focussed our attention on a fully three-dimensional problem initially presented in [30] and previously investigated in a number of articles [51, 55, 14, 63]. The

Brokenshire test consists of a specimen with a 45° oblique notch subject to a torsional load (see Figure 3.16 for a schematic description of the domain geometry). In experiment, the frame (shown in grey in Figure 3.16) is held at three of its end points, while the downward vertical displacement of the fourth one (facing the viewer in the figure) is prescribed. All the computations in this section were done using approximately 1.45 million linear tetrahedral elements with an average edge length of 2.5 mm near the oblique. The material properties used in our computations are consistent with the literature, and indicated in Table 3.6.

Table 3.6: Material properties for Brokenshire torsion experiments.

| E (GPa) | $\nu$ | $G_c$ ($\mathrm{Nm}^{-1}$) |
|---|---|---|
| 35 | 0.2 | 110 |

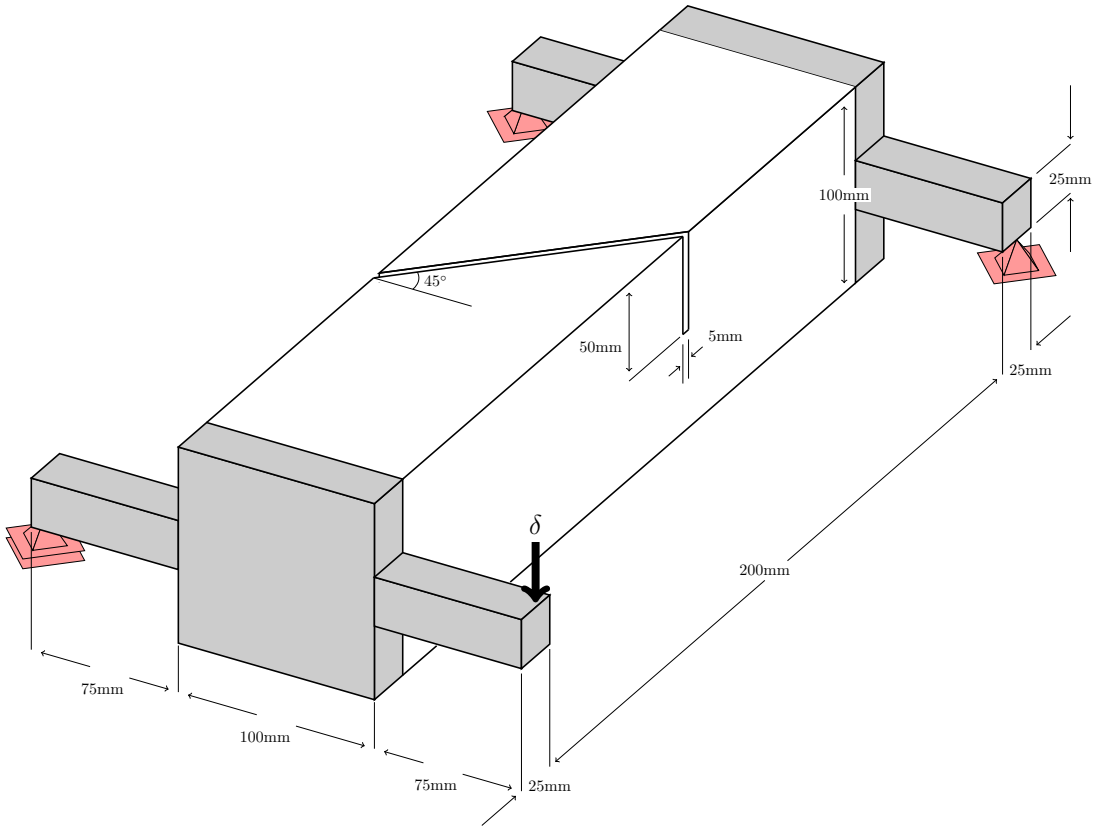


Figure 3.16: Schematics of the torsion experiment with oblique crack.

For such a problem, quantitative comparison with experiments is difficult, but the qualitative behavior that we observed, a three dimensional crack front turning to accommodate for change in the maximum normal stresses' orientation as it propagate (see Figure 3.17) is consistent with experiments. However, as previously noticed in the literature [51, 55, 14, 63], we also observed that the crack path is very sensitive to small changes in geometry and loading, or to changes in the regularization parameter $\epsilon$. Figure 3.18 shows changes in the final fracture geometry (isovolume renderings of the fracture field $0.9 \leq \alpha \leq 1.0$) and the final deformed geometry for three different values of $\epsilon$.

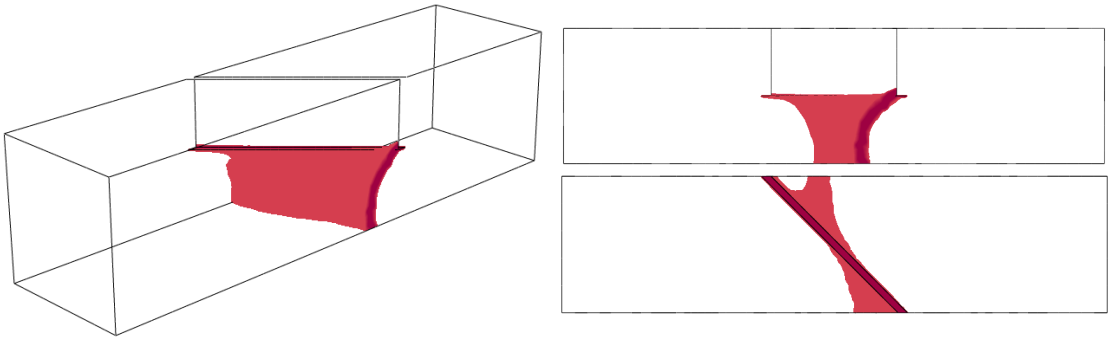

Figure 3.17: Brokenshire torsion simulation ($\epsilon = 12.5\,\text{mm}$): final crack geometry (left) isometric view (right top) front view (right bottom) top view.

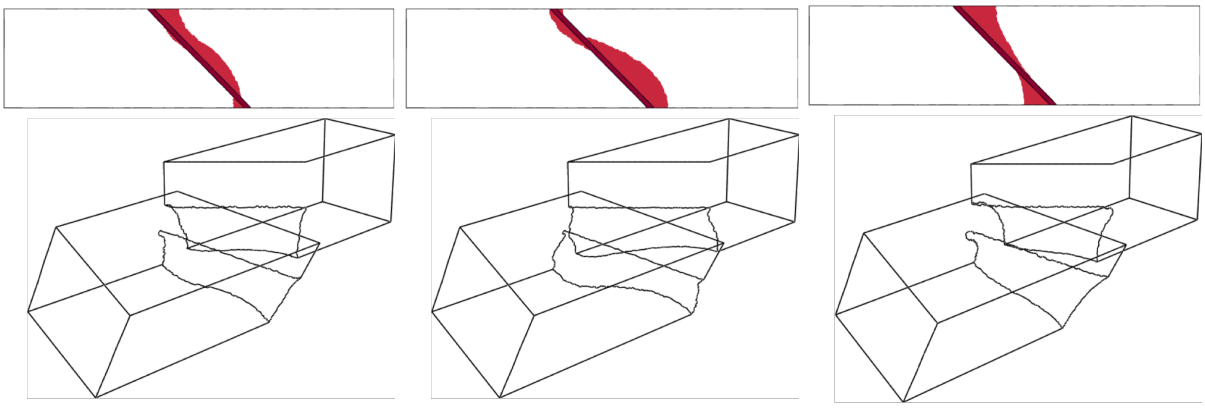

Figure 3.18: Brokenshire torsion simulation: (top) Top view of the final fracture geometry $0.9 \leq \alpha \leq 1.0$, (bottom) Isometric view of the final deformed geometry: (left) $\epsilon = 2.5\,\text{mm}$ (middle) $\epsilon = 5\,\text{mm}$ (right) $\epsilon = 12.5\,\text{mm}$.

## 3.6 Conclusions

In this article, we performed several validation experiment for the the variational approach to fracture [25], implemented through a regularized energy, focussing on situation where complex crack paths arise. We highlighted the adequacy of this approach for quantitative prediction of crack paths, without *a priori* hypotheses. We improved significantly on the backtracking algorithm by devising a variant exploring more states in configuration space.

In four distinct problems, we performed numerical simulations predicting crack paths that are consistent with experiments and the most accepted numerical literature. When nucleation of a crack with non-zero length is observed, the critical loading upon which cracks nucleate is shown to depends significantly on the regularization parameter $\epsilon$ of the regularized energy. This phenomenon should highlight the importance of the extensive study of gradient damage models in the one-dimensional case [93], and how it can be leveraged in numerical simulations, as in [27].

# CHAPTER 4
# COMPUTATIONAL INVESTIGATION OF THE DOUBLE-TORSION EXPERIMENTS

## 4.1 Abstract

In this chapter we apply the variational approach to fracture mechanics to investigate double-torsion experiments, used in the industry for fracture toughness measurement. We compare multiple schemes to handle unilateral contact across the cracks surfaces. We validate our numerical simulations using published sets of experimental data.

## 4.2 Introduction

The double-torsion experiments (Figure 4.1), as first introduced in the 1960s [89, 65], is an experimental method developed to measure the static and dynamic fracture toughness of brittle materials.

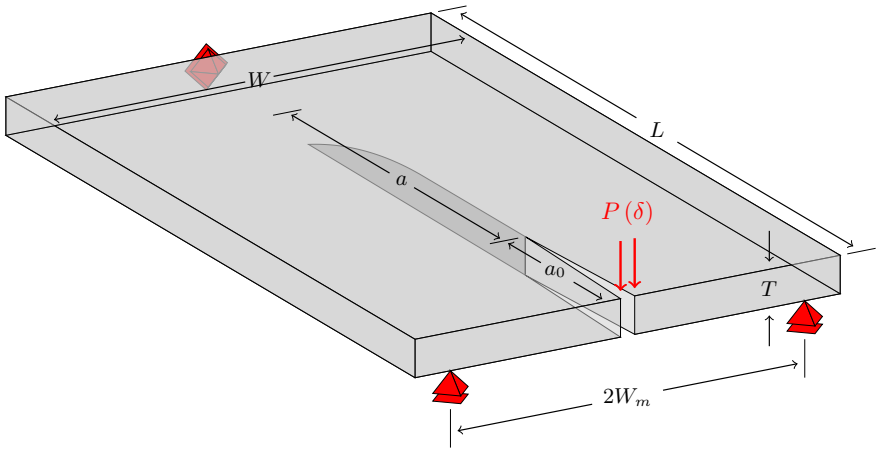


Figure 4.1: Schematics of the double-torsion experiment.

The original formulation and analysis was based on the simplification of the test setup to two cantilever beams under torsion. Using this assumption one can show that the compliance is a linear function of the crack length, which according to classical arguments of linear fracture mechanics results in the energy release rate $G$ from the tip of the advancing crack that does not depend on the length of the crack $a$ and can be written as [108]:

$$C = \frac{6W_m^2(1+\nu)}{WT^3E} \tag{4.1}$$

$$G = \frac{P^2}{2T}\frac{dC}{da} = \frac{3P^2W_m^2(1+\nu)}{WT^4E} \tag{4.2}$$

where $W$ is the width of the specimen, $W_m$ is the distance between the supports, $P$ is the applied force, $T$ is the thickness of the specimen (see Figure 4.1). Fuller [50] obtained a approximate solution for the double-torsion specimen by taking into account the thickness effect, but assuming two independent beams under torsion with a straight (un-curved) crack front and offered the corrected compliance as:

$$C_F = \frac{C}{\psi(T/W)} \tag{4.3}$$

where he obtained the following simplified expression for the specimens with $2T/W \leq 1$ with accuracy better than 0.1 percent:

$$\psi(T/W) = 1 - 0.6302\,(T/W) + 1.2\,(T/W)\,e^{(W\pi/T)} \tag{4.4}$$

Similar analyses were done by Young and Beaumount [112] and Hine et al. [58], in which they expanded the correction factor to be a second order function of the radii of support and loading cylinders, considering the effect of large displacement on the relative position of the supports and as a result the length of the torsion arm.

For short and long cracks (close to the specimen's end), an analysis based on two beams in torsion is no longer valid, and a significant deviation from the constant energy

release rate regime is observed. This non-linear effect was first discussed in [75] and later investigated using finite element analysis [105], and subsequently measured experimentally [101]. An extensive overview of the sample geometry was later compiled in [104] in which the authors recommended sample length of $L = 3W$ and thickness $t = {}^{W}/_{8}$ to ${}^{W}/_{12}$.

More recently, Ciccotti et al. [43, 44, 42] performed finite element analyses for a range of specimen size for double-torsion specimens with and without side grooves. In these analyses a mesh was generated with a curved crack-front where its profile was constructed from the experimental observations as an inclined straight line. Ciccotti et al. introduced a new correction factor that takes into account the non-linearity arising from dependence of energy release rate $G$ on crack length $a$.

The aim of this chapter is to expand the analysis on the correction factor taking into account the geometry of the crack-front. The variational approach to fracture mechanics as introduced in [49] and later developed in [25] is a versatile framework for the simulation of brittle fracture. In this framework the crack path and geometry are obtained as minimizers for a potential energy without use of *ad hoc* assumptions. The variational approach to fracture mechanics has been used over the past decade in many areas including elastic fracture [24, 22, 21, 78], thermoelastic fracture [74, 27], thin-film fracture [72, 71, 79], and electro-mechanical fracture [1, 2] to name a few. This framework lends itself as a unique tool since no assumptions have to be made on the profile of the crack-front, where it is obtained naturally through minimization of the potential energy.

In Section 4.3, we introduce the unilateral contact formulation within the variational approach to fracture mechanics. In Section 4.4, we describe the basis of our implementation and also the necessary formulation for calculation of the energy release rate. In Section 4.5 we first show validation results for our numerical simulations based on previously published experimental data and then expand the analysis for different geometries showing the variation of correction factors as the fracture propagates. Finally, in Section 4.6, we summarize the findings of this chapter and offer possible extensions.

## 4.3 Methodology

### 4.3.1 The variational approach to fracture mechanics

The variational approach to fracture mechanics [49, 25] is a framework to model the fracture phenomena in brittle materials. The variational approach to fracture mechanics is based on the minimization of the "potential energy" of the system. For an elastic body occupying the domain $\Omega \subset \mathbb{R}^3$ and for a displacement field $u$ and crack set $\Gamma \subset \Omega$, we define potential energy $\mathscr{E}_t(u, \Gamma)$ as:

$$\mathscr{E}_t(u, \Gamma) := \frac{1}{2} \int_{\Omega \setminus \Gamma} \mathcal{W}(\boldsymbol{e}(u))\, dx - \int_{\partial_N \Omega} f_t \cdot u\, dx + G_c \mathcal{H}^2(\Gamma) \tag{4.5}$$

where $\mathcal{W}(\boldsymbol{e}(u))$ is the bulk elastic potential. For a linear elastic material $\mathcal{W}(\boldsymbol{e}(u)) := \mathbb{C}\, \boldsymbol{e}(u) : \boldsymbol{e}(u)$, where $\mathbb{C}$ is the fourth order elasticity constitutive tensor (*i.e.,* Hooke's law) and $\boldsymbol{e}(u) = {}^1\!/_2(\nabla u + \nabla^T u)$ is the linearized strain tensor (*i.e.,* symmetric gradient). $G_c$ is the material's critical fracture toughness and $\mathcal{H}^2(\Gamma)$ is the two-dimensional Hausdorff measure of set $\Gamma$ (*i.e.,* aggregate area of fracture set $\Gamma$).

### 4.3.2 Non-dimensionalization

To carry out the computations, we introduce a reference displacement $u_0$, a reference length $L_0$, a reference stress $E_0$ and define the non-dimensional displacement $\tilde{u}$, coordinates $\tilde{x}$, elastic constitutive tensor $\tilde{\mathbb{C}}$ as:

$$\tilde{u} := \frac{u}{u_0}$$
$$\tilde{x} := \frac{x}{L_0}$$
$$\tilde{\mathbb{C}} := \frac{\mathbb{C}}{E_0}$$

We now define the non-dimensional potential energy following (4.5) as:

$$\tilde{\mathscr{E}}(\tilde{u}, \tilde{\Gamma}) = \frac{1}{2} \int_{\tilde{\Omega} \setminus \tilde{\Gamma}} \tilde{\mathbb{C}}\, \tilde{\boldsymbol{e}}(\tilde{u}) : \tilde{\boldsymbol{e}}(\tilde{u})\, dx - \int_{\partial_N \tilde{\Omega}} \tilde{f} \cdot \tilde{u}\, d\tilde{x} + \tilde{G} \mathcal{H}^2(\tilde{\Gamma}) \tag{4.6}$$

where $\tilde{\mathbb{C}} = \mathbb{C}/E_0$. Where, we define the non-dimensional force $\tilde{f}$ and the non-dimensional fracture toughness $\tilde{G}$ as:

$$\tilde{f} := \frac{fL_0}{E_0 u_0} \tag{4.7}$$

$$\tilde{G} := \frac{G_c L_0}{E_0 u_0^2} \tag{4.8}$$

For ease of notation, from this point on we omit the tilde on all fields, *i.e.,* we write $u$ for $\tilde{u}$ and so on.

### 4.3.3 Approximation of the energy functional

We follow previous works by Bourdin et al. [25] and introduce a regularization parameter $\epsilon > 0$ homogeneous to a length (that we call the characteristic approximation length) and a secondary variable $\alpha$ taking its values in $(0, 1)$ to represent the cracks. We define the regularized energy as:

$$\mathscr{E}_{t,\epsilon}(u, \alpha) := \frac{1}{2} \int_\Omega \mathcal{W}(\boldsymbol{e}(u), \alpha)\, dx - \mathscr{F}_t(u) + \frac{3G_c}{8} \int_\Omega \frac{\alpha}{\epsilon} + \epsilon |\nabla \alpha|^2\, dx, \tag{4.9}$$

where $\mathcal{W}(\boldsymbol{e}(u), \alpha)$ is the approximate elastic energy potential. The specific choice of this potential is further discussed in the following Section 4.3.4.

As previously discussed in 3.3.4, roughly speaking, as $\epsilon \to 0$, the displacement field minimizing (4.9) converges to that of minimizing (4.5), the field $\alpha$ converges to 0 almost everywhere and goes to zero "near the jumps of $u$" (*i.e.,* the cracks). Considering the irreversibility for a given $\epsilon$, we seek minimizers of (4.9).

### 4.3.4 Enforcing unilateral contact

The simplest form of the elastic potential can be written as:

$$\mathcal{W}(\boldsymbol{e}(u), \alpha) = ((1 - \alpha)^2 + \eta_\epsilon)\, \mathbb{C}\boldsymbol{e}(u) : \boldsymbol{e}(u) \tag{4.10}$$

where it used successfully in the previous Chapter 3 to model fracture in brittle materials. However, one can easily see that the approximate potential of form (4.10) does not prohibit fracture under pure compression. Since the specific geometry and loading configuration of the double-torsion test introduces a compressive region on the top half portion of the specimen, one has to forbid interpenetration of cracks under compression. Amor et al. [8] addressed this problem by introducing an approximate elastic potential based on hydrostatic-deviatoric orthogonal decomposition of the bulk elastic potential $\mathcal{W}$ :

$$\mathcal{W}(\boldsymbol{e}(u),\alpha) = ((1-\alpha)^2+\eta_\epsilon)\left(\kappa\,\mathrm{tr}^+\left(\boldsymbol{e}(u)\right)^2 + 2\mu\boldsymbol{e}^D(u):\boldsymbol{e}^D(u)\right) + \kappa\,\mathrm{tr}^-\left(\boldsymbol{e}(u)\right)^2 \quad (4.11)$$

where $\mathrm{tr}^+(\boldsymbol{e}(u)) = max(\mathrm{tr}(\boldsymbol{e}(u)),0)$ and $\mathrm{tr}^-(\boldsymbol{e}(u)) = max(-\mathrm{tr}(\boldsymbol{e}(u)),0)$.

As we will discuss later this model does not account for asymmetric behavior of the material under tension versus compression and thus permits the creation of spurious compressive cracks due to shear. To remedy this we introduce a modified version of approximate bulk elastic potential as:

$$\mathcal{W}(\boldsymbol{e}(u),\alpha) = \mathrm{H}\left(\mathrm{tr}^+(\boldsymbol{e}(u))\right)((1-\alpha)^2+\eta_\epsilon)\mathcal{W}(\boldsymbol{e}(u)) + (1-\mathrm{H}\left(\mathrm{tr}^+(\boldsymbol{e}(u))\right))\mathcal{W}(\boldsymbol{e}(u)) \quad (4.12)$$

where

$$\mathrm{H}(x) = \begin{cases} 1 \text{ if } x > 0 \\ 0 \text{ otherwise} \end{cases} \quad (4.13)$$

is the Heaviside function. To facilitate referring to these models, we will refer the model presented in (4.10) as the original bulk energy potential model, the model presented in (4.11) as hydrostatic-deviatoric decomposition model, and the model presented in (4.12) as the positive hydrostatic-deviatoric decomposition model. Later in Section 4.5 we will further investigate the behavior of these models.

## 4.4 Numerical implementation

Our minimization strategy for (4.9) is now classical [25, 78]. Minimization is achieved at each time step, using the separate convexity of the regularized energy (4.9) with respect to each field, by alternate minimization with respect to $u$ and $\alpha$ until the results converges. In this algorithm, the spatial discretization is done using the Galerkin finite element method.

The variational approach to fracture mechanics requires the spatial resolution of discretization to be several times bigger than the characteristic approximation length $\epsilon$. The resulting problems are often very large and necessitate the use of a parallel programming paradigm and the complex numerical tools therein. Our implementation relies on the distributed data structures provided by `libMesh` [66] and for linear algebra on `PETSc` [12, 10].

## 4.5 Results and discussion

In this section, we first discuss the steps taken for validating our numerical simulations and then expand our investigation to other cases. For validation purposes we used the data provided by Madjoubi et al. [73] from their experiments on soda-lime glass. Tables 4.1summarizes the material properties as well as the geometric dimensions of the experimental setup.

Table 4.1: Material properties and geometry in Madjoubi et al. [73].

| E [GPa] | $\nu$ | $G_c$ [Nm$^{-1}$] | $L$ [m] | $W$ [m] | $T$ [m] | $W_m$ [m] | $L_s$ [m] |
|---|---|---|---|---|---|---|---|
| 72 | 0.22 | 6.8 | 0.08 | .04 | 0.003 | 0.017 | 0.007 |

The first step to validate our numerical simulation versus the experimental data is to identify the most accurate set of boundary conditions for a given experimental setup. In the original conception, the double-torsion experiment was modeled as two beams under pure torsion. Therefore, in the numerical investigations done first in [105] and later in [42], the boundary conditions were applied as loading in z-direction on the 4 nodes at $(0, \pm 0, t)$ and $(0, \pm W_m, 0)$ and the rigid body motion was eliminated by fixing all displacements in a

node at $(L, 0, t/2)$ (see Figure 4.1) or as imposed pure torsion in the center of two ligaments in [15].

Figure 4.2 show the comparison between elastic-only numerical simulation containing straight explicit cracks using Madjoubi et al. [73] experimental data. In both cases, the numerical simulations with $\mathbb{P}^1$ linear tetrahedral elements result in stiffer structures compared to the experiments. This discrepancy is not surprising, and the large stiffness (smaller compliance) of $\mathbb{P}^1$ linear tetrahedral elements in bending is known [114] and can be attributed to weaker convergence of stresses in these elements [29]. Therefore, it is not surprising that when the numerical simulations are redone with $\mathbb{P}^2$–Lagrange tetrahedral elements, the numerical error is reduced. One puzzling aspect of the simulations depicted in 4.2 is that even though the straight crack has a larger fracture surface compared to the experimentally observed curved fracture, there is good match between the numerical simulations of explicit cracks with $\mathbb{P}^2$ elements. As discussed later, in the case of experimental data from Madjoubi et al. [73], the disparity could be due to experimental measurement errors or uncertainties in material parameters

### 4.5.1 Creation and treatment of spurious compressive fracture

As discussed previously in Section 4.3.4, although the unilateral contact model limits the creation of cracks under compression, it does not completely prohibit them. In Amor et al.'s model (4.11) the deviatoric part of the bulk energy is still available for the formation of cracks in compression. In the case of the double-torsion experiments, this can lead to the creation of unphysical compressive fracture in the top portion of mid-line ($y = 0$) (see Figure 4.3 for example).

Figure 4.4 shows a comparison between the dimensionless experimentally measured compliance and the numerical simulations using the hydrostatic-deviatoric decomposition (see (4.11)) using two different characteristic approximation lengths $\epsilon = 3h, 4h$ where $h =$

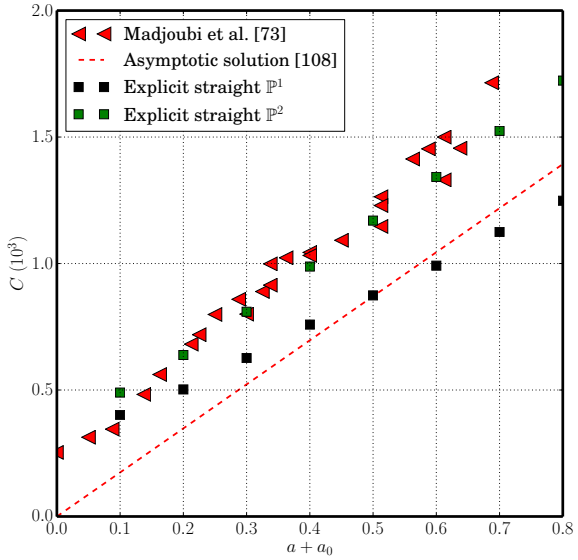


Figure 4.2: Dimensionless compliance of double-torsion experiments versus the dimensionless crack length: (red triangles) experimental data [73], (black squares) explicit straight cracks using $\mathbb{P}^1$ linear tetrahedral elements, (green squares) explicit straight cracks using $\mathbb{P}^2$ parabolic tetrahedral elements.

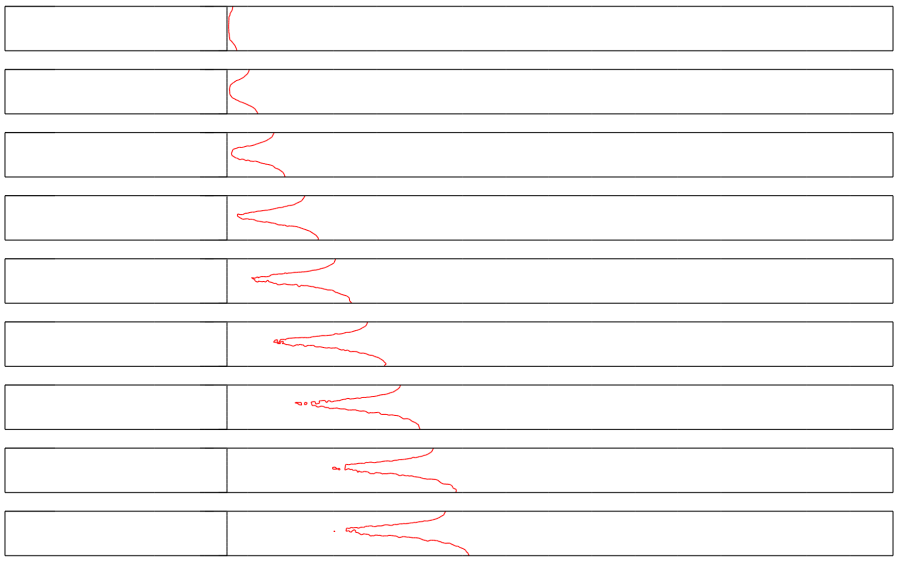

Figure 4.3: Numerical simulation of the double-torsion fracture using original unilateral contact formulation (4.11) moving crack front (*i.e.,* the contour line of $\alpha = 0.9$ on plane $y = 0$) at (from top) $\delta = 2, 3, 4, 5, 6, 7, 8, 9, 10$

$3.75 \times 10^{-3}$ is the approximate mesh size in the vicinity of the crack front. Since these numerical simulations use the $\mathbb{P}^1$ linear tetrahedral elements, it is not unexpected that they underestimate the compliance of double-torsion experiments.

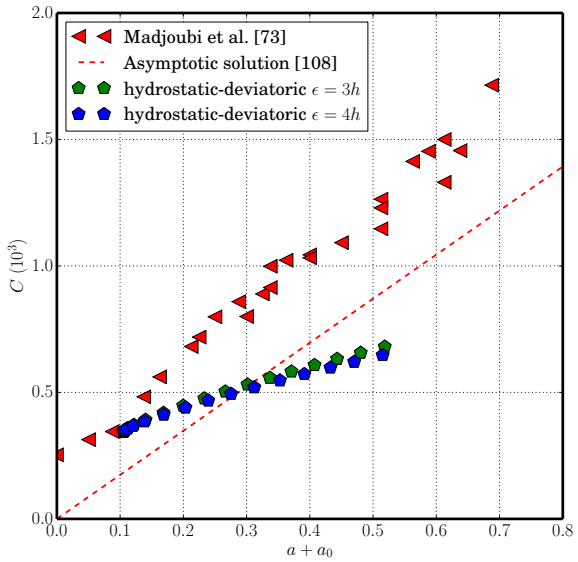


Figure 4.4: Dimensionless compliance of double-torsion experiments versus the dimensionless crack length: (red triangles) experimental data [73], (blue pentagons) numerical simulations using hydrostatic-deviatoric decomposition with characterstic length scale $\epsilon = 4h$, (green pentagons) numerical simulations using hydrostatic-deviatoric decomposition with characterstic length scale $\epsilon = 3h$.

In this section, we discuss two methods to remedy the creation of compressive cracks with the goal of improving the numerical results using hydrostatic-deviatoric decomposition. We will compare the compliance in each case to the experimental data from [73] and demonstrate convergence in each case.

#### 4.5.1.1 Use of Buffer Layers

The most simple solution to alleviate this spurious effect is to add a non-damageable buffer layer. Although this is very effective in remedying the compressive cracks it introduces an added compliance to the sample. To rectify this effect, we set the elastic modulus of this buffer layer to a much smaller value compared to the material properties. This,

however, introduces a new set of shear crack at the bottom of this buffer layer and can affect the geometry of the crack front. However, numerical simulations suggest that the thickness of this spurious compressive crack zone as well as the added compliance, diminish as $\epsilon \to 0$ and therefore, when using a "fine enough" mesh, will have minimal impact on calculations. Figure 4.5 show the propagation of the crack front (the contour line of $\alpha = 0.9$ on the plane $y = 0$) at different loading parameters with a relative elastic modulus of the buffer layer set to ${}^{E}/_{E_b} = 10^4$ for the geometry and material properties defined in Table 4.1.

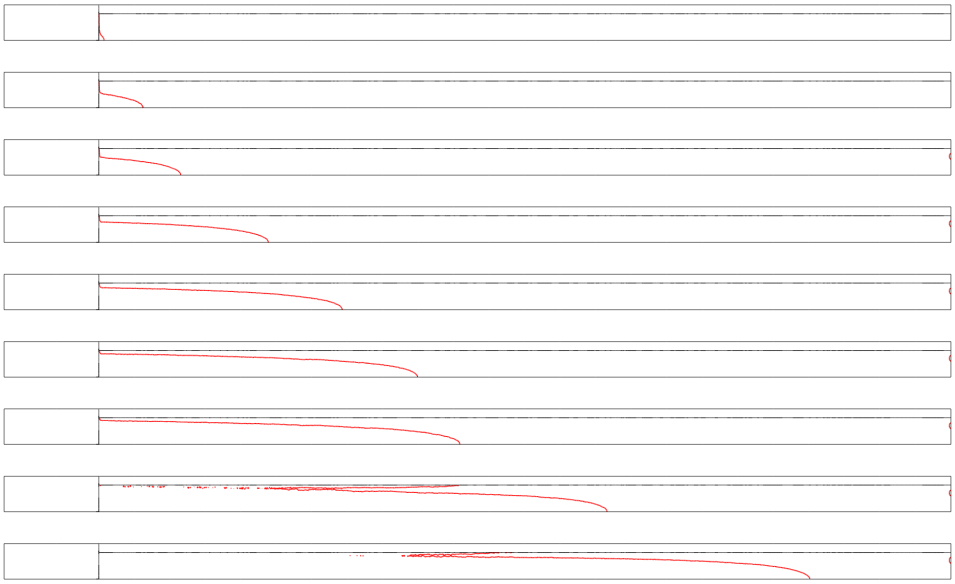

Figure 4.5: Numerical simulation of the double-torsion fracture using buffer layer with ${}^{E}/_{E_b} = 10^4$: moving crack front (*i.e.,* the contour line of $\alpha = 0.9$ on plane $y = 0$) at (from top) $\delta = 2.4$, 3.2, 4, 4.8, 5.6, 6.4, 7.2, 8

Figure 4.6 shows the comparison between the dimensionless experimentally measured compliance and the numerical simulations using buffer layers with relative thicknesses of ${}^{T}/_{3}$ and ${}^{T}/_{4}$ and with two different relative compliances of the buffer layer ${}^{E}/_{E_b} = 10^3$ and $10^4$. As the Figure 4.6 shows, the error between the experimental measurement reduces as the thickness of the buffer layer is reduced. Also, one can see that the effect of the relative compliance of the buffer layer diminishes as the layer becomes thinner.

Since the numerical calculations in Figure 4.6 were done using $\mathbb{P}^1$ linear tetrahedral

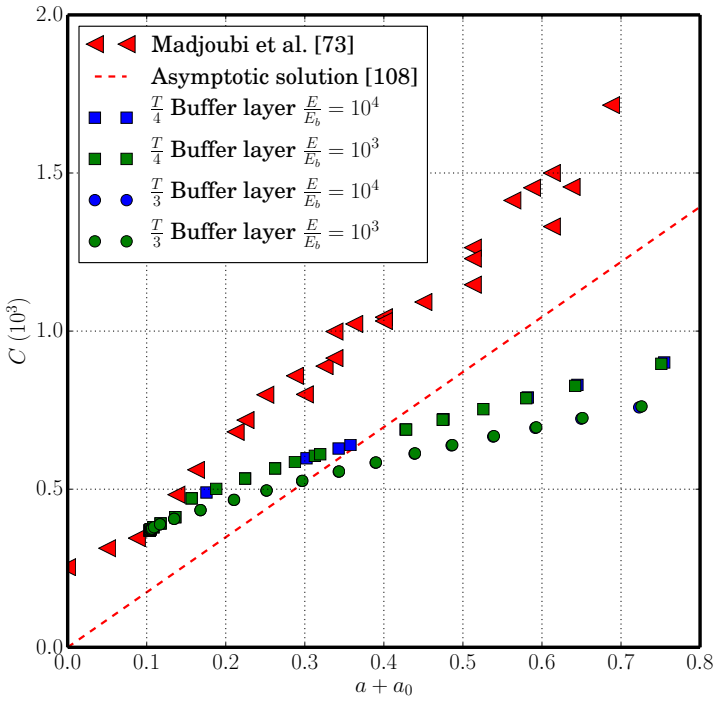


Figure 4.6: Dimensionless compliance of double-torsion experiments versus the dimensionless crack length: (red triangles) experimental data [73], (green circles) numerical simulation with $T/3$ buffer layer scheme $E/E_b = 10^3$, (blue circles) numerical simulation with $T/3$ buffer layer scheme $E/E_b = 10^4$, (green squares) numerical simulation with $T/4$ buffer layer scheme $E/E_b = 10^3$, (blue squares) numerical simulation with $T/4$ buffer layer scheme $E/E_b = 10^4$.

elements, it is not unexpected that we observe a lower compliance compared to the experiments. Figure 4.7 shows a comparison between dimensionless experimentally measured compliance and a numerical simulation done using $\mathbb{P}^2$ parabolic tetrahedral elements. As expected, the accuracy of the computations is tremendously improved.

#### 4.5.1.2 Positive Spherical-Deviatoric Decomposition

Another option to eliminate the compressive fracture layers to use the positive hydrostatic-deviatoric decomposition as introduced in (4.12). This formulation eliminates the access to deviatoric energy when cracks are under compression, and thus remedies the creation of compressive cracks. Figure 4.8 depicts the propagation of the crack front (the contour line

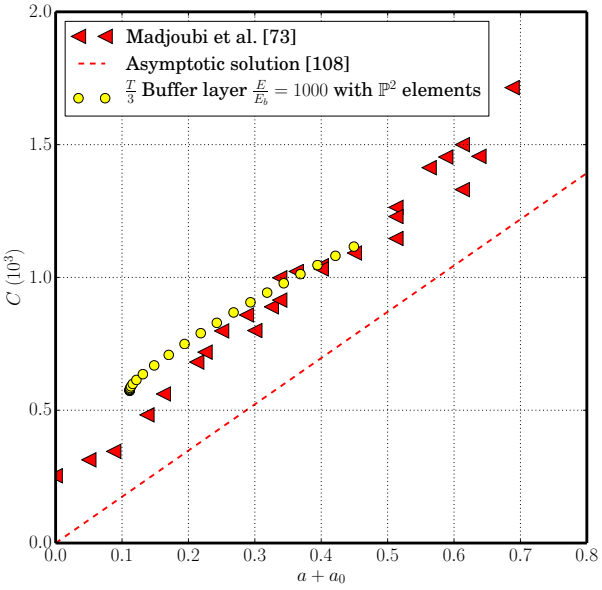


Figure 4.7: Dimensionless compliance of double-torsion experiments versus the dimensionless crack length: (red triangles) experimental data [73], (yellow circles) numerical simulation with $T/3$ buffer layer scheme $E/E_b = 10^3$ using $\mathbb{P}^2$ parabolic tetrahedral elements.

of $\alpha = 0.9$ on plane $y = 0$) at different loading parameters for the geometry and material properties defined in Table 4.1.

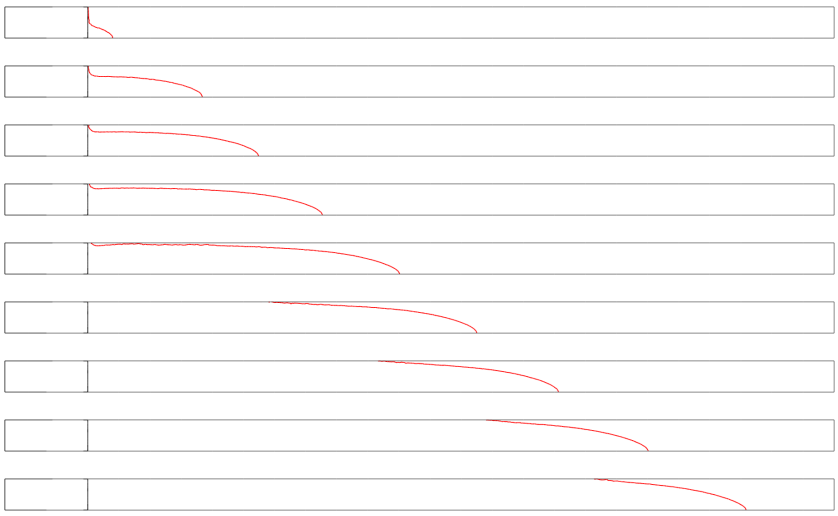

Figure 4.8: Numerical simulation of the double-torsion fracture using positive hydrostatic-deviatoric scheme: moving crack front (*i.e.,* the contour line of $\alpha = 0.9$ on plane $y = 0$) at (from top) $\delta = 4,\ 6,\ 8,\ 10,\ 12,\ 14,\ 16,\ 18,\ 20$

Figure 4.9 shows the comparison between the dimensionless experimentally measured compliance and the numerical simulations using the positive hydrostatic-deviatoric model (4.12). Once more, the numerical simulations result in a lower compliance compared to the experimental data. As shown in before (see Figure 4.2 for example) the error could be attributed to the use of $\mathbb{P}^1$ linear tetrahedral elements.

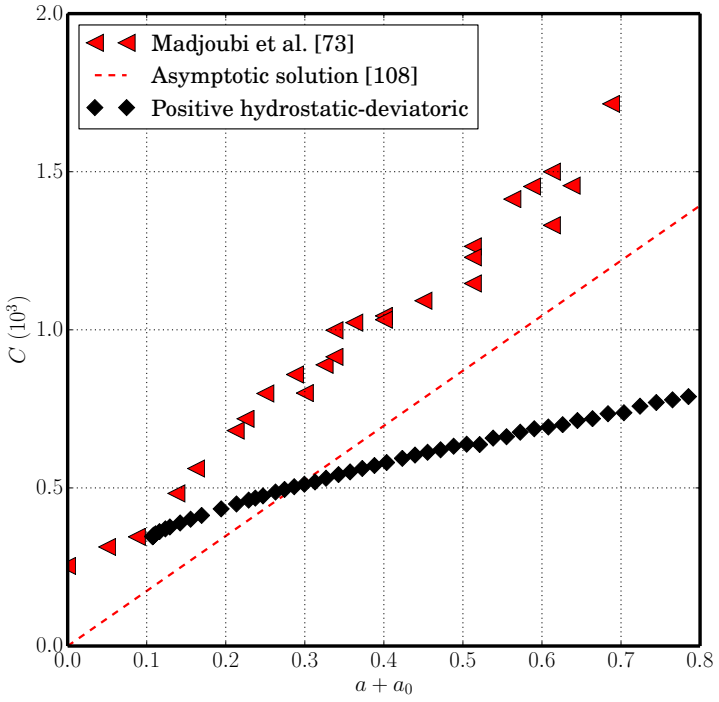


Figure 4.9: Dimensionless compliance of double-torsion experiments versus the dimensionless crack length: (red triangles) experimental data [73], (black diamonds) numerical simulation using positive hydrostatic-deviatoric decomposition.

### 4.5.2 Comparison between numerical simulations using buffer layer versus positive hydrostatic-deviatoric

Now that two different methods of remedying compressive cracks (*i.e.,* compliant buffer layer, and positive hydrostatic-deviatoric decomposition) are introduced, they can be compared against eachother. Figure 4.10 compares the dimensionless experimentally measured compliance for the set of experiments [73] (as summarized in Table 4.1) with the numerical

simulation results using compliant buffer layers and positive hydrostatic-deviatoric formulation. Predictions of both methods using $\mathbb{P}^1$ linear tetrahedra elemements underestimate the compliance of the double-torsion specimen, but are very close. These results verifiy that both these methods converge regardless of the mesh size. The accuracy of the simulations increases dramatically using higher order $\mathbb{P}^2$ parabolic tetrahedral elements and converges to the observed experimental data.

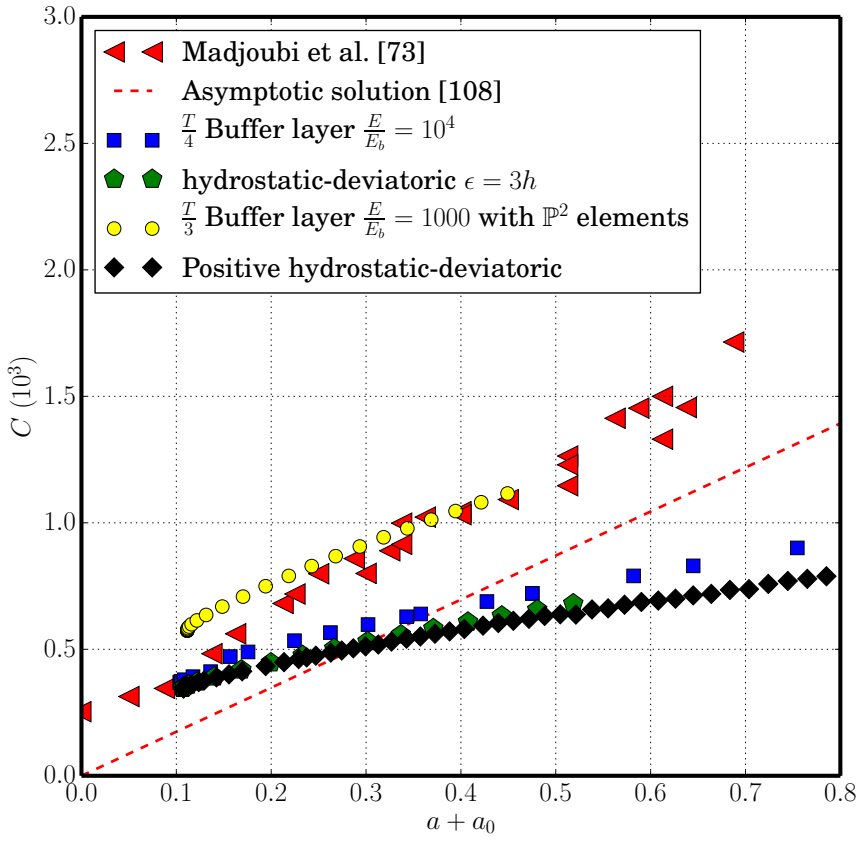


Figure 4.10: Dimensionless compliance of double-torsion experiments versus the dimensionless crack length: (red triangles) experimental data [73], (green pentagons) numerical simulations using hydrostatic-deviatoric decomposition with characterstic length scale $\epsilon = 3h$, (blue squares) numerical simulation with $T/4$ buffer layer scheme $E/E_b = 10^4$, (yellow circles) numerical simulation with $T/3$ buffer layer scheme $E/E_b = 10^3$ using $\mathbb{P}^2$ parabolic tetrahedral elements, (black diamonds) numerical simulation using positive hydrostatic-deviatoric decomposition.

### 4.5.3 Comparison of the numerical simulations against correction factor results from the literature

Figure 4.11 illustrates the comparison between the experimental data from [73], the theoretical calculation based on the Fuller's correction [50] (see (4.3)), the theoretical calculations with correction factors from Ciccotti et al. [42], the numerical calculation with explicit straight cracks, and the results of our numerical simulations based on unilateral contact formulation (see Section 4.3.3) with a buffer layer and higher order elements. All models, excluding our numerical simulations underestimate the compliance. It is possible that the use of linear tetrahedral elements in the case of Ciccotti et al. [42], undermines the accuracy of the simulations.

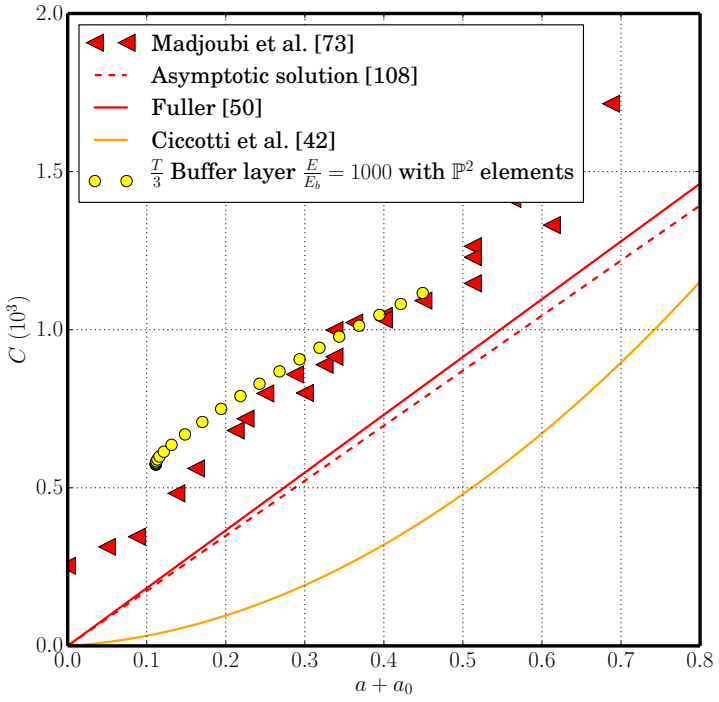


Figure 4.11: Compliance vs. crack length: comparison of: (red triangles) experimental data , (red line) theoretical formulation, (orange line) Ciccotti et al. correction [42], , (yellow circles) numerical simulation with $T/3$ buffer layer scheme $E/E_b = 10^3$ using $\mathbb{P}^2$ parabolic tetrahedral elements, (black diamonds) numerical simulation using positive hydrostatic-deviatoric decomposition.

### 4.5.4 Verification of numerical simulation using energy release rate

The energy release rate $G$ is the parameter of interest in the double-torsion experiments. Since our numerical scheme is built upon the Griffith fracture assumption, the quasi-static stable crack growth results in an energy release rate equal to the fracture toughness (*i.e.,* the critical energy release rate). In the next section, we present a method to calculate energy release rate using the bulk and surface energy.

#### 4.5.4.1 Calculation of Energy Release Rate $G$

Energy release rate can be defined as:

$$G := -\frac{\partial \mathscr{B}}{\partial A}|_{t=cst} \tag{4.14}$$

where $A = \mathcal{H}^2(\Gamma)$ is the aggregate surface of cracks [†].

Since in the quasi-static evolution, as described in Section 4.3, the loading (*i.e.,* the imposed vertical displacement on notch see Figure 4.1) is applied monotonically one can write:

$$\frac{\partial \mathscr{B}}{\partial A} = \frac{\partial \mathscr{B}}{\partial A}|_{t=cst} + \frac{\partial \mathscr{B}}{\partial t}|_{A=cst}\frac{\partial t}{\partial A} \tag{4.15}$$

However, since the loading is monotonic one can easily show that $\mathscr{B}|_{A=cst} = kt^2$, therefore:

$$\frac{\partial \mathscr{B}}{\partial t}|_{A=cst} = 2\frac{\mathscr{B}}{t} \tag{4.16}$$

Combining (4.14-4.16) one can write:

$$G = \frac{\partial \mathscr{B}}{\partial A} - 2\frac{\mathscr{B}}{t}\frac{\partial t}{\partial A} \tag{4.17}$$

where in the following calculations, the crack length was calculated as the length of the initial notch $a_0$ plus the area of the fracture $\mathcal{H}^2(\Gamma)$ divided by the thickness $T$:

[†]Here we assume that the bulk energy possesses the necessary smoothness with respect to the crack area

$$a = \frac{\mathcal{H}^2(\Gamma)}{T} + a_0 \tag{4.18}$$

In the following calculations, the non-dimensional fracture toughness was set to $G = 1$. Here, the distance of the support from the center line was set as $W_m = 0.45W$, and the Poisson ratio of $\nu = 0.22$ was used. Figure 4.12 shows the variation of the energy release rate (calculated using the method described previously in 4.5.4.1) versus the dimensionless crack length.

In Figure 4.12, one may notice that since the in the initial phase of the loading the fracture front is stationary, use of finite differences results in $G \to \infty$. However, for an advancing fracture, the energy release rate $G = 1$ with less than 5 percent error. For very long cracks $a \geq 0.8L$ the propagation becomes unstable once more resulting in brutal fracture.

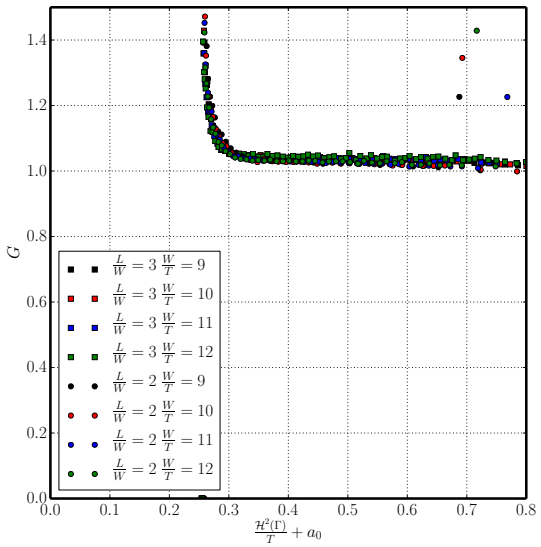


Figure 4.12: Compliance of double-torsion specimen vs. crack length: comparison of theoretical and numerical values for different thicknesses.

### 4.5.5 Calculation of correction factor for given geometry

As a proof of concept, using the calculated value of the energy release rate from the numerical simulations and the classical formulation for the double-torsion experiments (4.2) one can calculate the corresponding correction factors $\psi(W/L, T/W, a)$. Figure 4.13 illustrates the change of correction factor versus crack length for different sample thickness to length and width to length ratios for the same series of numerical simulations as above. One can see that (within the thickness to width ratios used here) for a given width to length ratio the calculated correction factor curves collapse on each other. Also, for the wider sample $L/W = 2$, one can see that there is a deviation from continues trend at about $a = 0.7$, which is created due to the creation of a fracture zone at the position of end boundary conditions.

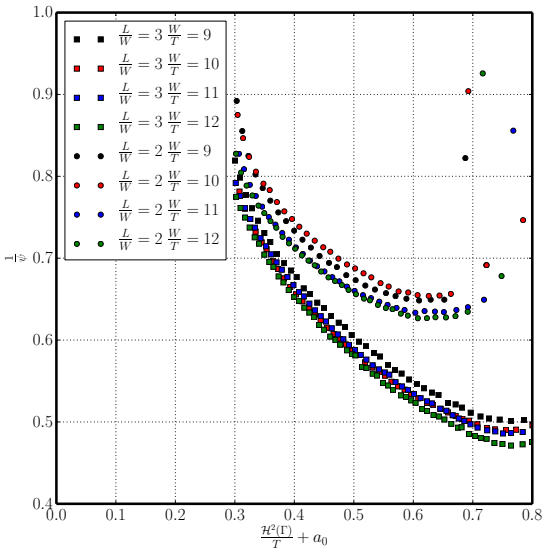


Figure 4.13: Inverse of the correction factor for double-torsion specimen vs. crack length: comparison of theoretical and numerical values for different thicknesses.

## 4.6 Conclusions and recommended future work

In this chapter, we studied the fracture in double-torsion specimens using the variational approach to fracture mechanics. Double-torsion experiments, as first introduced in the 1960s is a method of studying the static and dynamic fracture properties of brittle ma-

terials. However, as previously pointed out by other researchers, the simplifications done in the original derivation of classical formulation neglects some crucial effects that can affect the accuracy of the experimental results. Lack of a standard specimen geometry and a standard fixture results in scenarios where the classical formulation performs poorly and without an in-depth analysis of the fracture mechanics can lead to erroneous results.

We showed that the variational approach to fracture mechanics can be used effectively to perform numerical simulations for a given geometry. Using the unilateral contact formulation, we showed that the curved crack front can be modeled effectively. Spurious compressive cracks on the top section of the mid-plane were addressed using two methods (i) by introducing a non-brittle buffer zone, (ii) using our proposed positive hydrostatic-deviatoric model. We studied the convergence behavior of simulations with buffer layers and showed convergence as the thickness of the buffer layer decreases.

The biggest challenge was the inaccuracy of linear tetrahedral elements under bending. We showed that using higher order $\mathbb{P}^2$ elements, the accuracy of calculation of compliance improves significantly. The next logical step is to perform simulations using these higher order elements in conjunction with our two proposed formulations.

We also showed that by using this approach correction factors can be calculated for a few sample geometries and it was shown that the correction factor varies with crack length. This means that in most situation the compliance is not a linear function of the crack length. We concluded that in order to perform valid analysis on fracture properties using the double-torsion test simple correction factors are inadequate.For the best results, the experiments most be performed in conjunction with a complete set of numerical analyses addressing the non-linear effects rising from specimen geometry, boundary conditions, and the moving curved fracture front.

# CHAPTER 5
# CONCLUDING REMARKS AND RECOMMENDED FUTURE WORK

## 5.1 Conclusions

In this dissertation, we studied the phenomena of fracture in solids using the variational approach to fracture mechanics. The variational approach to fracture mechanics formulates the problem of the initiation and propagation of fracture in a solid medium as an energy minimization principle. We started with an overview of the basic concepts of the variational approach to fracture mechanics in Chapter 1.

In Chapter 2, we applied the variational framework to the fracture of thin films. As a result of the inherent multi-dimensional nature of thin-film topology (*i.e.,* thickness vs. other dimensions), we first performed an asymptotic study and reduced the dimension of the problem from three to two dimensions in Section 2.8. Using the new two-dimensional elastic setting (*i.e.,* plate on an elastic foundation), we formulated the problem of fracture in the thin films in Section 2.3. We showed that by using this two-dimensional setting and variational approach to fracture mechanics, one can model a wide range of phenomena (*e.g.* creation of ring and radial cracks, creation of parallel network of cracks, etc.) previously thought to be separate can be explained as facets of the introduced two-dimensional model with respect to different geometrical scales (*i.e.,* film thickness divided by the domain length).

In Chapter 3, we treated the problem of fracture in two and three-dimensional homogeneous isotropic solids. We performed a validation study for the variational approach to fracture mechanics using a number of well-documented studies in the literature. In this chapter we proposed a new *deep backtracking algorithm* (Section 3.4) that offers a rem-

edy for brutal fracture propagation that impedes the ability of the variational approach to fracture mechanics to correctly recover intricate fracture paths.

In Chapter 4, we investigated the fracture in double-torsion experiments. The double-torsion experiment, as proposed in the 1960s, is a method for study of static and dynamic fracture behavior of brittle solids. The original formulation is based on many simplifying assumptions that limit the usefulness of this method. Different correction factors considering an array of issues have been proposed by other investigators over the past 60 years; however, they fall short since the experimental setup (*i.e.,* geometry of specimen and fixture) is not standard. The variational approach to fracture mechanics and the unilateral contact formulation within that provide a versatile tool for studying this important experimental technique. After introducing the formulation, we first validate our numerical simulation based on a set of previously published results, and then extend our analysis to a few carefully chosen geometries and fixture configurations.

## 5.2 Recommended future work

In the past decade, the variational approach to fracture mechanics was introduced as a strong contender in the field of brittle fracture. The variational approach to fracture mechanics owes its potential to strong physical and mathematical backbones. However, the complexity of the fundamental aspects of the formulation has been a barrier for the wider engineering community to embrace this technique. It is the author's hope that this dissertation and the articles emerging from its development serve as a bridge between the founding applied mathematics community and the engineering audience. The author of this dissertation offers the following as proposed theoretical paths forward:

- Over the past few years, more and more connections between the variational approach to fracture mechanics and gradient damage and phase field models of fracture have been established putting all these methods in a larger framework of smeared fracture

simulation. An important contribution to the field can come from a unifying and thermodynamically consistent framework for all these methods.

- As shown in Chapter 4, one of the major hurdles in need of careful investigation is enforcement of unilateral contact within the fractured medium. Such a model is of utmost importance if the variational approach to fracture is to be used as a standard tool in the real-world engineering problems.

- Variational framework of fracture mechanics also holds a boundless potential to be extended to problems involving a tertiary class of phenomena, whether in the form of plastic (in-elastic) behavior or modeling of corrosive fracture. Mass transport equations can be incorporated easily within this framework, and a variable fracture toughness as a function of corrosive factors diffusion can be easily implemented.

- As shown in Chapter 3, (Section 3.5.2) small changes in the initial geometry can lead to vastly different fracture paths. Motivated by this observation, another set of extensions to the variational approach to fracture can be made in conjunction with stochastic methods. Engineering advances in the field are reliant on the ability of predictive methods to include the inherent randomness in the material properties as well as other sources of uncertainty in the input data. In the author's opinion polynomial chaos methods offer a sound basis for such an extension.

It is the author's hope that this treatise on the different aspects of the variational approach to fracture mechanics can be used as a stepping stone for these proposed investigations and more importantly, as is the nature of science, the unanticipated upcoming works.

# References


[1] A. Abdollahi and I. Arias. Phase-field modeling of the coupled microstructure and fracture evolution in ferroelectric single crystals. *Acta Materialia*, 59(12):4733–4746, 7 2011.

[2] A. Abdollahi and I. Arias. Phase-field modeling of crack propagation in piezoelectric and ferroelectric materials with different electromechanical crack conditions. *Journal of the Mechanics and Physics of Solids*, 60(12):2100–2126, 12 2012.

[3] G. Allaire, F. Jouve, and N. Van Goethem. Damage and fracture evolution in brittle materials by shape optimization methods. *Journal of Computational Physics*, 230(12):5010–5044, 2011.

[4] L. Ambrosio. Existence theory for a new class of variational problems. *Archive for Rational Mechanics and Analysis*, 111(4):291–322, 1990.

[5] L. Ambrosio and V. M. Tortorelli. On the approximation of free discontinuity problems. *Bollettino dell'Unione Matematica Italiana*, 6:105–123, 1992.

[6] L. Ambrosio and V.M. Tortorelli. Approximation of functionals depending on jumps by elliptic functionals via $\gamma$-convergence. *Communications on Pure and Applied Mathematics*, 43(8):999–1036, 1990.

[7] F. Amiri, D. Millán, Y. Shen, T. Rabczuk, and M. Arroyo. Phase-field modeling of fracture in linear thin shells. *Theoretical and Applied Fracture Mechanics*, 69(0):102 – 109, 2014.

[8] H. Amor, J.-J. Marigo, and C. Maurini. Regularized formulation of the variational brittle fracture with unilateral contact: Numerical experiments. *Journal of the Mechanics and Physics of Solids*, 57(8):1209–1229, 2009.

[9] P. Areias and T. Belytschko. Analysis of three-dimensional crack initiation and propagation using the extended finite element method. *International Journal for Numerical Methods in Engineering*, 63(5):760–788, 2005.

[10] S. Balay, J. Brown, K. Buschelman, V. Eijkhout, W.D. Gropp, D. Kaushik, M.G. Knepley, L.C. McInnes, B.F. Smith, and H. Zhang. PETSc users manual. Technical Report ANL-95/11 - Revision 3.3, Argonne National Laboratory, 2012.

[11] S. Balay, J. Brown, K. Buschelman, V. Eijkhout, W.D. Gropp, D. Kaushik, M.G. Knepley, L.C. McInnes, B.F. Smith, and H. Zhang. PETSc Web page, 2012. http://www.mcs.anl.gov/petsc.

[12] S. Balay, W.D. Gropp, L.C. McInnes, and Smith B.F. Efficient management of parallelism in object oriented numerical software libraries. In E. Arge, A. M. Bruaset,

and H. P. Langtangen, editors, *Modern Software Tools in Scientific Computing*, pages 163–202. Birkhäuser Press, 1997.

[13] G. I. Barenblatt. The mathematical theory of equilibrium cracks in brittle fracture. *Advances in applied mechanics*, 7(55-129):104, 1962.

[14] M. Baydoun and T. P. Fries. Crack propagation criteria in three dimensions using the xfem and an explicit–implicit crack description. *International Journal of Fracture*, 178(1-2):51–70, 2012.

[15] T. H. Becker, T. J. Marrow, and R. B. Tait. An evaluation of the double torsion technique. *Experimental Mechanics*, 51(9):1511–1526, 2011.

[16] S. J. Benson and T. S. Munson. Flexible complementarity solvers for large-scale applications. *Optimization Methods and Software*, 21(1):155–168, 2006.

[17] P.E. Bernard, N. Moës, and N. Chevaugeon. Damage growth modeling using the thick level set (tls) approach: Efficient discretization for quasi-static loadings. *Computer Methods in Applied Mechanics and Engineering*, 233:11–27, 2012.

[18] T. N. Bittencourt, P. A. Wawrzynek, A. R. Ingraffea, and J. L. Sousa. Quasi-automatic simulation of crack propagation for 2d lefm problems. *Engineering Fracture Mechanics*, 55(2):321–334, 1996.

[19] J. Bobiński and J. Tejchman. A constitutive model for concrete based on continuum theory with non-local softening coupled with extended finite element method. *Computational Modelling of Concrete Structures*, page 117, 2014.

[20] M. J. Borden, C. V. Verhoosel, M. A. Scott, T. J.R. Hughes, and C. M. Landis. A phase-field description of dynamic brittle fracture. *Comput. Methods Appl. Mech. Engrg.*, 217–220(0):77 – 95, 2012.

[21] B. Bourdin. Numerical implementation of the variational formulation for quasi-static brittle fracture. *Interfaces and Free Boundaries*, 9(3):411–430, 2007.

[22] B. Bourdin. The variational formulation of brittle fracture: numerical implementation and extensions. In *IUTAM Symposium on Discretization Methods for Evolving Discontinuities*, pages 381–393. Springer, 2007.

[23] B. Bourdin and A. Chambolle. Implementation of an adaptive finite-element approximation of the Mumford-Shah functional. *Numerische Mathematik*, 85(4):609–646, 2000.

[24] B. Bourdin, G. A. Francfort, and J.-J. Marigo. Numerical experiments in revisited brittle fracture. *Journal of the Mechanics and Physics of Solids*, 48(4):797–826, 2000.

[25] B. Bourdin, G. A. Francfort, and J.-J. Marigo. The variational approach to fracture. *Journal of Elasticity*, 91(1):5–148, 2008.

[26] B. Bourdin, C.J. Larsen, and C.L. Richardson. A time-discrete model for dynamic fracture based on crack regularization. *International journal of fracture*, 168(2):133–143, 2011.

[27] B. Bourdin, J.-J. Marigo, C. Maurini, and P. Sicsic. Morphogenesis and propagation of complex cracks induced by thermal shocks. *Phys. Rev. Lett.*, 112:014301, Jan 2014.

[28] A. Braides. *Approximation of free-discontinuity problems*. Lecture notes in mathematics. Springer-Verlag, 1998.

[29] S. C. Brenner and R. Scott. *The mathematical theory of finite element methods*, volume 15. Springer, 2008.

[30] D. R. Brokenshire. *A study of torsion fracture tests*. PhD thesis, Cardiff University, 1996.

[31] S. Burke, C. Ortner, and E. Süli. An adaptive finite element approximation of a variational model of brittle fracture. *SIAM J. Numer. Anal.*, 48(3):980–1012, 2010.

[32] H. Chai and B. R. Lawn. Fracture mode transitions in brittle coatings on compliant substrates as a function of thickness. *Journal of materials research*, 19(6):1752–1761, 2004.

[33] A. Chambolle. Image segmentation by variational methods: Mumford and Shah functional and the discrete approximations. *SIAM Journal on Applied Mathematics*, 55(3):827–863, 1995.

[34] A. Chambolle. A density result in two-dimensional linearized elasticity, and applications. *Archive for Rational Mechanics and Analysis*, 167(3):211–233, 2003.

[35] A. Chambolle. An approximation result for special functions with bounded variations. *Journal de Mathématiques Pures et Appliquées*, 83:929–954, 2004.

[36] A. Chambolle. Addendum to "an approximation result for special functions with bounded deformation" [j. math. pures appl. (9) 83 (7) (2004) 929–954]: the n-dimensional case. *Journal de Mathématiques Pures et Appliquées*, 84:137–145, 2005.

[37] A. Chambolle, G. A. Francfort, and J.-J. Marigo. When and how do cracks propagate? *Journal of the Mechanics and Physics of Solids*, 57(9):1614–1622, 2009.

[38] A. Chambolle, A. Giacomini, and M. Ponsiglione. Crack initiation in brittle materials. *Archive for Rational Mechanics and Analysis*, 188(2):309–349, 2008.

[39] M. Charlotte and G. A. Francfort. Revisiting brittle fracture as an energy minimization problem: comparison of Griffith and Barenblatt surface energy models. In *Proceedings of the Symposium on "Continuous Damage and Fracture*, pages 7–12, 2000.

[40] J. Chen. Indentation-based methods to assess fracture toughness for thin coatings. *Journal of Physics D: Applied Physics*, 45(20):203001, 2012.

[41] P. G. Ciarlet. *Mathematical elasticity: Theory of plates*, volume 27 of *Studies in mathematics and its applications*. Elsevier, 1997.

[42] M. Ciccotti. Realistic finite-element model for the double-torsion loading configuration. *Journal of the American Ceramic Society*, 83(11):2737–2744, 2000.

[43] M. Ciccotti, G. Gonzato, and F. Mulargia. The double torsion loading configuration for fracture propagation: an improved methodology for the load-relaxation at constant displacement. *International Journal of Rock Mechanics and Mining Sciences*, 37(7):1103–1113, 10 2000.

[44] M. Ciccotti, N. Negri, G. Gonzato, and F. Mulargia. Practical application of an improved methodology for the double torsion load relaxation method. *International Journal of Rock Mechanics and Mining Sciences*, 38(4):569–576, 6 2001.

[45] G. Dal Maso and R. Toader. A model for the quasi-static growth of brittle fractures: Existence and approximation results. *Archive for Rational Mechanics and Analysis*, 162(2):101–135, 2002.

[46] R. De Borst. Some recent developments in computational modelling of concrete fracture. *International journal of fracture*, 86(1-2):5–36, 1997.

[47] D. S. Dugdale. Yielding of steel sheets containing slits. *Journal of the Mechanics and Physics of Solids*, 8(2):100–104, 5 1960.

[48] M. Focardi. On the variational approximation of free-discontinuity problems in the vectorial case. *Mathematical Models & Methods in Applied Sciences*, 11(663–684), 2001.

[49] G. A. Francfort and J.-J. Marigo. Revisiting brittle fracture as an energy minimization problem. *Journal of the Mechanics and Physics of Solids*, 46(8):1319–1342, 1998.

[50] E. R. Fuller. *Fracture mechanics applied to brittle materials*, volume 678 of *Fracture mechanics applied to brittle materials, ASTM STP*, chapter An Evaluation of Double Torsion Testing–Analysis, pages 3–18. ASTM International, 1979.

[51] T. C. Gasser and G. A. Holzapfel. 3d crack propagation in unreinforced concrete.: A two-step algorithm for tracking 3d crack paths. *Computer Methods in Applied Mechanics and Engineering*, 195(37):5198–5219, 2006.

[52] S. Geniaut and E. Galenne. A simple method for crack growth in mixed mode with x-fem. *International Journal of Solids and Structures*, 2012.

[53] A. Giacomini. Ambrosio-Tortorelli approximation of quasi-static evolution of brittle fractures. *Calculus of Variations and Partial Differential Equations*, 22(2):129–172, 2005.

[54] A. A. Griffith. The phenomena of rupture and flow in solids. *Philosophical transactions of the royal society of london. Series A, containing papers of a mathematical or physical character*, 221:163–198, 1921.

[55] E. Gürses and C. Miehe. A computational framework of three-dimensional configurational-force-driven brittle crack propagation. *Computer Methods in Applied Mechanics and Engineering*, 198(15):1413–1428, 2009.

[56] V. Hakim and A. Karma. Laws of crack motion and phase-field models of fracture. *Journal of the Mechanics and Physics of Solids*, 57(2):342–368, 2009.

[57] H. Henry and H. Levine. Dynamic instabilities of fracture under biaxial strain using a phase field model. *Physical Review Letters*, 93(10):105–504, 2004.

[58] P. J. Hine, R. A. Duckett, and I. M. Ward. A double-torsion study of the fracture of polyethersulphone. *Journal of Materials Science*, 19(11):3796–3805, 1984.

[59] J. W. Hutchinson and Z. Suo. Mixed mode cracking in layered materials. *Advances in Applied mechanics*, 29:63–191, 1992.

[60] A. R. Ingraffea and M. Grigoriu. Probabilistic fracture mechanics: a validation of predictive capability. Technical report, DTIC Document, 1990.

[61] G. R. Irwin. *Fracture*, volume 6 of *Hanbuch der Physik, herausgegeben: Elastizät und Plastizität*. Springer, Berlin, 1958.

[62] P. Jäger, P. Steinmann, and E. Kuhl. Modeling three-dimensional crack propagation—a comparison of crack path tracking strategies. *International Journal for Numerical Methods in Engineering*, 76(9):1328–1352, 2008.

[63] L. Kaczmarczyk, M. M. Nezhad, and C. Pearce. Three-dimensional brittle fracture: configurational-force-driven crack propagation. *International Journal for Numerical Methods in Engineering*, 97(7):531–550, 2014.

[64] A. Karma and A. E. Lobkovsky. Unsteady crack motion and branching in a phase-field model of brittle fracture. *Physical Review Letters*, 92(24):245–510, 2004.

[65] J. A. Kies and A. B. J. Clarck. Fracture propagation rates and times to fail following proof stress in bulk glass. In P. L. Pratt, editor, *Fracture 1969 : proceedings of the Second International conference on fracture*, page 483. Chapman & Hall, London, 1969.

[66] B. S. Kirk, Peterson J. W., Stogner R. H., and Carey G. F. `libMesh`: A C++ Library for Parallel Adaptive Mesh Refinement/Coarsening Simulations. *Engineering with Computers*, 22(3–4):237–254, 2006.

[67] C. J. Larsen, C. Ortner, and E. Süli. Existence of solutions to a regularized model of dynamic fracture. *Math. Models Methods Appl. Sci.*, 20(7):1021–1048, 2010.

[68] B. R. Lawn. Indentation of ceramics with spheres: a century after hertz. *Journal of the American Ceramic Society*, 81(8):1977–1994, 1998.

[69] B. R. Lawn, Y. Deng, P. Miranda, A. Pajares, H. Chai, and D.K. Kim. Overview: Damage in brittle layer structures from concentrated loads. *Journal of Material Research*, 17(12):3019–3036, 2002.

[70] A. A. Léon Baldelli. *On Fracture of Thin Films: a Variational Approach*. PhD thesis, l'Université Pierre et Marie Curie, 2013.

[71] A. A. Léon Baldelli, J.-F. Babadjian, B. Bourdin, D. Henao, and C. Maurini. A variational model for fracture and debonding of thin films under in-plane loadings. *Journal of the Mechanics and Physics of Solids*, In press, 2014.

[72] A. A. Léon Baldelli, B. Bourdin, J.-J. Marigo, and C. Maurini. Fracture and debonding of a thin film on a stiff substrate: analytical and numerical solutions of a 1d variational model. *Continuum Mechanics and Thermodynamics*, 25(2-4):243–268, 2013.

[73] M. A. Madjoubi, M. Hamidouche, N. Bouaouadja, J. Chevalier, and G. Fantozzi. Experimental evaluation of the double torsion analysis on soda-lime glass. *Journal of Materials Science*, 42(18):7872–7881, 2007.

[74] C. Maurini, B. Bourdin, G. Gauthier, and V. Lazarus. Crack patterns obtained by unidirectional drying of a colloidal suspension in a capillary tube: experiments and numerical simulations using a two-dimensional variational approach. *International Journal of Fracture*, 184(1-2):75–91, 2013.

[75] K. R. Mckinney and H. I. Smith. Method of studying subcritical cracking of opaque materials. In *American Ceramic Society Bulletin*, volume 50, page 784, 1971.

[76] S. Dj. Mesarovic and N. A. Fleck. Spherical indentation of elastic–plastic solids. *Proceedings of the Royal Society of London. Series A: Mathematical, Physical and Engineering Sciences*, 455(1987):2707–2728, 1999.

[77] G. Meschke and P. Dumstorff. Energy-based modeling of cohesive and cohesionless cracks via X-FEM. *Computer Methods in Applied Mechanics and Engineering*, 196(21–24):2338–2357, 4 2007.

[78] A. Mesgarnejad, B. Bourdin, and M. M. Khonsari. Validation simulations for the variational approach to fracture mechanics. *Computer Methods in Applied Mechanics and Engineering*, 2014.

[79] A. Mesgarnejad, B. Bourdin, and M.M. Khonsari. A variational approach to the fracture of brittle thin films subject to out-of-plane loading. *Journal of mechanics and physics of solids*, 61(11):2360–2379, November 2013.

[80] C. Miehe, M. Hofacker, and F. Welschinger. A phase field model for rate-independent crack propagation: Robust algorithmic implementation based on operator splits. *Computer Methods in Applied Mechanics and Engineering*, 199(45-48):2765 – 2778, 2010.

[81] C. Miehe, F. Welschinger, and M. Hofacker. Thermodynamically consistent phase-field models of fracture: Variational principles and multi-field FE implementations. *International Journal for Numerical Methods in Engineering*, 83(10):1273–1311, 2010.

[82] C. Miehe, F. Welschinger, and M. Hofacker. Thermodynamically consistent phase-field models of fracture: Variational principles and multi-field FE implementations. *International Journal for Numerical Methods in Engineering*, 83(10):1273–1311, 2010.

[83] L. L. Mishnaevsky and D. Gross Jr. Micromechanisms and Mechanics of Damage and Fracture in Thin Film/Substrate Systems. *International Applied Mechanics*, 40(2):140–155, 2004.

[84] N. Moës, J. Dolbow, and T. Belytschko. A finite element method for crack growth without remeshing. *International Journal for Numerical Methods in Engineering*, 46:131–150, 1999.

[85] K. R. Morasch and D. F. Bahr. An energy method to analyze through thickness thin film fracture during indentation. *Thin Solid Films*, 515(6):3298–3304, 2007.

[86] T. Munson, J. Sarich, S. Wild, S. Benson, and L.C. McInnes. Tao 2.0 users manual. Technical Report ANL/MCS-TM-322, Mathematics and Computer Science Division, Argonne National Laboratory, 2012. http://www.mcs.anl.gov/tao.

[87] M. B. Nooru-Mohamed. *Mixed-mode fracture of concrete: an experimental approach.* PhD thesis, Delft University of Technology, 1992.

[88] M. Ortiz and A. Pandolfi. Finite-deformation irreversible cohesive elements for three-dimensional crack-propagation analysis. *International Journal for Numerical Methods in Engineering*, 44:1267–1282, 1999.

[89] J. O. Outwater and D. J. Gerry. On the fracture energy, rehealing velocity and refracture energy of cast epoxy resin. *The Journal of Adhesion*, 1(4):290–298, 2014/09/06 1969.

[90] B. Patzák and M. Jirásek. Adaptive resolution of localized damage in quasi-brittle materials. *Journal of engineering mechanics*, 130(6):720–732, 2004.

[91] K. Pham and J.-J. Marigo. Damage localization and rupture with gradient damage models. *Fracture and Structural Integrity*, 19, 2012.

[92] K. Pham and J.-J. Marigo. From the onset of damage to rupture: construction of responses with damage localization for a general class of gradient damage models. *Continuum Mechanics and Thermodynamics*, pages 1–25, 2013.

[93] K. Pham, J.-J. Marigo, and C. Maurini. The issues of the uniqueness and the stability of the homogeneous response in uniaxial tests with gradient damage models. *Journal of the Mechanics and Physics of Solids*, 59(6):1163 – 1190, 2011.

[94] K. Pham, J.-J. Marigo, and C. Maurini. The issues of the uniqueness and the stability of the homogeneous response in uniaxial tests with gradient damage models. *Journal of the Mechanics and Physics of Solids*, 59(6):1163–1190, 2011.

[95] P. Pivonka, J. Ožbolt, R. Lackner, and H.A. Mang. Comparative studies of 3d-constitutive models for concrete: application to mixed-mode fracture. *International Journal for Numerical Methods in Engineering*, 60(2):549–570, 2004.

[96] Y.-W. Rhee, H.-W. Kim, Y. Deng, and B. R. Lawn. Contact-induced damage in ceramic coatings on compliant substrates: fracture mechanics and design. *Journal of the American Ceramic Society*, 84(5):1066–1072, 2001.

[97] J. R. Rice. A path independent integral and the approximate analysis of strain concentration by notches and cracks. *Journal of applied mechanics*, 35(2):379–386, 1968.

[98] J. R. Rice. Mathematical analysis in the mechanics of fracture. *Fracture: an advanced treatise*, 2:191–311, 1968.

[99] A. Schlüter, A.ter, A. Willenbücher, C. Kuhn, and R. MLler. Phase field approximation of dynamic brittle fracture. *Computational Mechanics*, pages 1–21, 2014.

[100] B. Schmidt, F. Fraternali, and M. Ortiz. Eigenfracture: An eigendeformation approach to variational fracture. *Multiscale Modeling & Simulation*, 7(3):1237–1266, 2009.

[101] D. K. Shetty and A. V. Virkar. Determination of the useful range of crack lengths in double torsion specimens. *Journal of the American Ceramic Society*, 61(1-2):93–94, 1978.

[102] K. A. Sierros, A. J. Kessman, R. Nair, N. X. Randall, and D. R. Cairns. Spherical indentation and scratch durability studies of transparent conducting layers on polymer substrates. *Thin Solid Films*, 520(1):424–429, 2011.

[103] R. Szilard. *Theories and applications of plate analysis: classical, numerical, and engineering methods*. Wiley, 2004.

[104] R. B. Tait, P. R. Fry, and G. G. Garrett. Review and evaluation of the double-torsion technique for fracture toughness and fatigue testing of brittle materials. *Experimental Mechanics*, 27(1):14–22, 1987.

[105] G. G. Trantina. Stress analysis of the double-torsion specimen. *Journal of the American Ceramic Society*, 60(7-8):338–341, 1977.

[106] J.F. Unger, S. Eckardt, and C. Könke. Modelling of cohesive crack growth in concrete structures with the extended finite element method. *Computer Methods in Applied Mechanics and Engineering*, 196(41–44):4087–4100, 9 2007.

[107] G. Ventura, JX. Xu, and T. Belytschko. A vector level set method and new discontinuity approximations for crack growth by efg. *International Journal for Numerical Methods in Engineering*, 54(6):923–944, 2002.

[108] D. P. Williams and A. G. Evans. A simple method for crack growth. *Journal of Testing and Evaluation*, 1:264–270, 1973.

[109] B.J. Winkler. *Traglastuntersuchungen von unbewehrten und bewehrten Betonstrukturen auf der Grundlage eines objektiven Werkstoffgesetzes für Beton.* Innsbruck University Press, 2001.

[110] Z. C. Xia and J. W. Hutchinson. Crack patterns in thin films. *Journal of the Mechanics and Physics of Solids*, 48(6-7):1107–1131, 2000.

[111] X. P. Xu and A. Needleman. Numerical simulations of fast crack-growth in brittle solids. *International Journal of Solids and Structures*, 42(9):1397–1434, 1994.

[112] R. J. Young and P. W. R. Beaumont. Failure of brittle polymers by slow crack growth. *Journal of Materials Science*, 12(4):684–692, 1977.

[113] K. Zeng, F. Zhu, J. Hu, L. Shen, K. Zhang, and H. Gong. Investigation of mechanical properties of transparent conducting oxide thin films. *Thin solid films*, 443(1):60–65, 2003.

[114] O. C. Zienkiewicz and R. L. Taylor. *The Finite Element Method: Solid Mechanics*, volume 2. Butterworth-heinemann, 2000.

# Appendix A
# VFMFE

In this chapter we briefly introduce the formulation used in the Variational Fracture Mechanics Finite Element code (from this point on referred to by its acronym VFMFE). VFMFE is fully parallel *Galerkin finite element* code capable of performing quasi-static fracture mechanics analysis based on variational approach to fracture mechanics.

## A.1 Finite element formulation

As explained previously in Section 1.4 the Amborosio-Tortorelli approximation of the variational fracture mechanics is convex in both displacement $u$ and smeared fracture field $\alpha$. We can write the formulation of the Galerkin finite element for the variational approach to fracture mechanics be deriving the Gâteaux derivative of of the energy (1.6) in $u$ and $\alpha$ directions.

### A.1.1 Displacement Problem

We can write the Gâteaux derivative of the energy (1.6) with respect to $u$ in $v$ direction as:

$$\frac{\partial \mathscr{E}_\eta}{\partial u}(v,\alpha) = \int_\Omega \alpha^2 \frac{\partial \mathcal{W}}{\partial u}(v)\, dx - \int_\Omega f_b \cdot v\, dx - \int_{\partial_N \Omega} f_s \cdot v\, dx \tag{A.1}$$

the first order optimality condition then will read as:

$$\frac{\partial \mathscr{E}_\eta}{\partial u}(v,\alpha) = 0 \ , \forall v \in \mathcal{K}_A \tag{A.2}$$

where $\mathcal{K}_A$ is the admissible displacement field (*i.e.,* it satisfies homogeneous dirichlet boundary conditions).

In VFMFE two main sets of local bulk potentials $\mathcal{W}$ are implemented

- Out-of-plane thin-film as defined in (2.11).
- Two and three dimensional elasticity as defined in (3.7).

for these two main sets we can write the derivative of the bulk energy local potential $\frac{\partial \mathcal{W}}{\partial u}(v)$ as

$$\frac{\partial \mathcal{W}}{\partial u} = \mathcal{C}e(u) : e(v) \tag{A.3}$$

for elasticity and

$$\frac{\partial \mathcal{W}_b}{\partial u} = \mathcal{C}\mathrm{D}^2(u) : \mathrm{D}^2(v) \tag{A.4}$$

$$\frac{\partial \mathcal{W}_c}{\partial u} = (u - u_0)(v) \tag{A.5}$$

for out-of-plane thin-film setting[†].

*Remark* A.1. Astute reader will notice that the equation (A.1) for $\alpha = 1$ is the expression of the elastic (or thin-film) problem without fracture.

### A.1.2 Fracture Problem

Similarly, we can write the Gâteaux derivative of the energy (1.6) with respect to $\alpha$ in $\xi$ direction as:

$$\frac{\partial \mathscr{E}_\eta}{\partial \alpha}(u, \xi) = \int_\Omega \alpha \xi \mathcal{W}(u)\, dx + \int_\Omega G_c(x, \alpha) \left( \frac{m\alpha^m - 1\xi}{\eta} + 2\eta \nabla\alpha \cdot \nabla\xi \right) dx \tag{A.6}$$

the first order optimality condition follows:

$$\frac{\partial \mathscr{E}_\eta}{\partial \alpha}(u, \xi) = 0 \ , \forall \xi \in \mathcal{A} \tag{A.7}$$

where $\mathcal{A}$ is the admissible fracture field (*i.e.,* it satisfies the irreversibility condition).

[†]the bulk potential for the thin-film formulation breaks down in two parts as was shown with detail in 2.8.

### A.1.3 Galerkin Finite Element Statement of Displacement and Fracture Problems

To obtain the Galerkin finite element formulation for the displacement problem one has to introduce a mapping between nodal values $(\hat{u}, \hat{\alpha})$ and the spatial values of the displacement $(u(x), \alpha(x))$ in an element and

$$u(x) = \sum_{i=1}^{N_u} P_i^u \hat{u}_i \tag{A.8}$$

$$\alpha(x) = \sum_{j=1}^{N_\alpha} P_j^\alpha \hat{\alpha}_j \tag{A.9}$$

where $P_i^u$, $i = 1..N_u$ are the basis functions for the displacement problem and $P_i^\alpha$, $i = 1..N_\alpha$ are the basis functions for the fracture problem $\hat{u}_i$ and $\hat{\alpha}_i$ are respectively the nodal value of displacement and fracture at the i$^{\text{th}}$ degree of freedom.

The first order optimality for displacement and fracture problems then can be written as

$$K_{ij}^u \hat{u}_i = f_j^u \tag{A.10}$$

$$K_{ij}^\alpha \hat{\alpha}_i = f_j^\alpha \tag{A.11}$$

where the stiffness matrix and force vector for displacement $K^u$,$f^u$ and for the smeared fracture $K^\alpha$, $f^\alpha$ can be derived as follows:

- for elasticity (3.7):

$$K_{ij}^u = \sum_{e \in \mathcal{T}} \sum_{j=1}^{N_u} \left( \int_e \Big( \sum_{k=1}^{N_\alpha} P_k^\alpha \hat{\alpha}_k \Big)^2 \mathcal{C} e(P_i^u) : e(P_j^u)\, dx \right) \tag{A.12}$$

$$f_j^u = \sum_{e \in \mathcal{T}} \sum_{j=1}^{N_u} \left( \int_e f_b \cdot P_j^u\, dx + \int_{\partial e \cap \partial_N \Omega} f_s \cdot P_j^u\, dx \right) \tag{A.13}$$

- for out-of-plane formulation on thin-film (2.11):

$$K_{ij}^{u} = \sum_{e\in\mathcal{T}}\sum_{j=1}^{N_u}\Big(\int_e \Big(\sum_{k=1}^{N_\alpha} P_k^\alpha \hat{\alpha}_k\Big)^2 \mathcal{C}\mathrm{D}^2(P_i^u) : \mathrm{D}^2(P_j^u)\,dx + K\int_e P_j^u P_i^u\,dx\Big) \tag{A.14}$$

$$f_j^u = \sum_{e\in\mathcal{T}}\sum_{j=1}^{N_u}\Big(\int_e P_j^u u_0(x)\,dx\Big) \tag{A.15}$$

- Fracture problem with AT2

$$K_{ij}^{\alpha} = \sum_{e\in\mathcal{T}}\sum_{j=1}^{N_u}\Big(\int_e 2P_i^\alpha P_j^\alpha\,\mathcal{W}\Big(\sum_{k=1}^{N_u} P_k^u \hat{u}_k\Big)\,dx - \int_e \frac{G_c(x)}{4C_\eta}\Big(\frac{P_j^\alpha P_i^\alpha}{\eta} + \eta\nabla(P_i^\alpha)\cdot\nabla(P_j^\alpha)\Big)\,dx\Big) \tag{A.16a}$$

$$f_j^{\alpha} = \sum_{e\in\mathcal{T}}\sum_{j=1}^{N_u}\Big(\int_e \frac{G_c(x)}{4C_\eta\eta} P_j^\alpha\,dx\Big) \tag{A.16b}$$

- Fracture problem with AT1

$$K_{ij}^{\alpha} = \sum_{e\in\mathcal{T}}\sum_{j=1}^{N_u}\Big(\int_e 2P_i^\alpha P_j^\alpha\,\mathcal{W}\Big(\sum_{k=1}^{N_u} P_k^u \hat{u}_k\Big)\,dx - \int_e \frac{G_c(x)}{4C_\eta}\Big(\eta\nabla(P_i^\alpha)\cdot\nabla(P_j^\alpha)\Big)\,dx\Big) \tag{A.17a}$$

$$f_j^{\alpha} = \sum_{e\in\mathcal{T}}\sum_{j=1}^{N_u}\Big(\int_e \frac{G_c(x)}{4C_\eta\eta} P_j^\alpha\,dx\Big) \tag{A.17b}$$

*Remark* A.2. We should point out that $P^u$:

- in case of out-of-plane thin-film formulation is a one-dimensional at least $C^1$ continious basis.

- in case of $n$-dimensional elasticity is a $n$-dimensional basis.

# Appendix B
# LETTERS OF PERMISSION TO USE PUBLISHED MATERIALS

**Title:** A variational approach to the fracture of brittle thin films subject to out-of-plane loading
**Author:** A. Mesgarnejad,B. Bourdin,M.M. Khonsari
**Publication:** Journal of the Mechanics and Physics of Solids
**Publisher:** Elsevier
**Date:** November 2013



Logged in as:
Ata Mesgarnejad
LOGOUT

**Order Completed**

Thank you very much for your order.

This is a License Agreement between Ata Mesgarnejad ("You") and Elsevier ("Elsevier"). The license consists of your order details, the terms and conditions provided by Elsevier, and the payment terms and conditions.

Get the printable license.

| | |
|---|---|
| License Number | 3484970246661 |
| License date | Oct 09, 2014 |
| Licensed content publisher | Elsevier |
| Licensed content publication | Journal of the Mechanics and Physics of Solids |
| Licensed content title | A variational approach to the fracture of brittle thin films subject to out-of-plane loading |
| Licensed content author | A. Mesgarnejad,B. Bourdin,M.M. Khonsari |
| Licensed content date | November 2013 |
| Licensed content volume number | 61 |
| Licensed content issue number | 11 |
| Number of pages | 20 |
| Type of Use | reuse in a thesis/dissertation |
| Portion | full article |
| Format | both print and electronic |
| Are you the author of this Elsevier article? | Yes |
| Will you be translating? | No |
| Title of your thesis/dissertation | Applications of the variational approach to fracture mechanics |
| Expected completion date | Dec 2014 |
| Estimated size (number of pages) | 120 |
| Elsevier VAT number | GB 494 6272 12 |
| Permissions price | 0.00 USD |
| VAT/Local Sales Tax | 0.00 USD / 0.00 GBP |
| Total | 0.00 USD |

Copyright Clearance Center RightsLink®

Account Info | Help

**Title:** Validation simulations for the variational approach to fracture
**Author:** A. Mesgarnejad,B. Bourdin,M.M. Khonsari
**Publication:** Computer Methods in Applied Mechanics and Engineering
**Publisher:** Elsevier
**Date:** Dec 31, 1969
Copyright © 1969, Elsevier

Logged in as:
Ata Mesgarnejad
Account #:
3000843855
LOGOUT

**Order Completed**

Thank you very much for your order.

This is a License Agreement between Ata Mesgarnejad ("You") and Elsevier ("Elsevier") The license consists of your order details, the terms and conditions provided by Elsevier, and the payment terms and conditions.

| | |
|---|---|
| License number | Reference confirmation email for license number |
| License date | Nov 19, 2014 |
| Licensed content publisher | Elsevier |
| Licensed content publication | Computer Methods in Applied Mechanics and Engineering |
| Licensed content title | Validation simulations for the variational approach to fracture |
| Licensed content author | A. Mesgarnejad,B. Bourdin,M.M. Khonsari |
| Licensed content date | Available online 17 November 2014 |
| Licensed content volume number | n/a |
| Licensed content issue number | n/a |
| Number of pages | 1 |
| Type of Use | reuse in a thesis/dissertation |
| Portion | full article |
| Format | both print and electronic |
| Are you the author of this Elsevier article? | Yes |
| Will you be translating? | No |
| Title of your thesis/dissertation | Applications of the variational approach to fracture mechanics |
| Expected completion date | Dec 2014 |
| Elsevier VAT number | GB 494 6272 12 |
| Billing Type | Invoice |
| Billing address | 2203 Patrick F. Taylor Hall |
| | Louisiana State University |
| | BATON ROUGE, LA 70803 |
| | United States |
| Permissions price | 0.00 USD |
| VAT/Local Sales Tax | 0.00 USD / 0.00 GBP |
| Total | 0.00 USD |

# VITA

Ata Mesgarnejad was born in 1982 in Tehran, Iran. He graduate from Alborz High School in 1998. He proceeded to get his B.Sc. and M.Sc. in mechanical engineering from the Islamic Azad University, central Tehran branch in 2005 and from Amirkabir University of Technology in 2007. He is currently a candidate for the Masters degree in Applied Mathematics at Louisiana State University which will be awarded December 2014. He is also a candidate for Doctor of Philosophy degree in Mechanical Engineering at Louisiana State University which will also be awarded in December 2014.